

อิทธิพลของโซเดียมในกระบวนการประดิษฐ์เซลล์สุริยะชนิดฟิล์มบางคอปเปอร์อินเดียมแกลเลียม
ไดซีไลน์ประสิทธิภาพสูง



นายราชศักดิ์ ศักดานุภาพ

ศูนย์วิทยทรัพยากร จุฬาลงกรณ์มหาวิทยาลัย

วิทยานิพนธ์นี้เป็นส่วนหนึ่งของการศึกษาตามหลักสูตรปริญญาวิทยาศาสตรดุษฎีบัณฑิต

สาขาวิชาฟิสิกส์ ภาควิชาฟิสิกส์

คณะวิทยาศาสตร์ จุฬาลงกรณ์มหาวิทยาลัย

ปีการศึกษา 2553

ลิขสิทธิ์ของจุฬาลงกรณ์มหาวิทยาลัย

INFLUENCE OF SODIUM IN FABRICATION PROCESS OF HIGH EFFICIENCY
Cu(In,Ga)Se₂ THIN FILM SOLAR CELLS



Mr. Rachsak Sakdanuphab

ศูนย์วิทยทรัพยากร
จุฬาลงกรณ์มหาวิทยาลัย

A Dissertation Submitted in Partial Fulfillment of the Requirements
for the Degree of Doctor of Philosophy Program in Physics

Department of Physics

Faculty of Science

Chulalongkorn University

Academic year 2010

Copyright of Chulalongkorn University

Thesis Title INFLUENCE OF SODIUM IN FABRICATION PROCESS
OF HIGH EFFICIENCY Cu(In,Ga)Se₂ THIN FILM
SOLAR CELLS

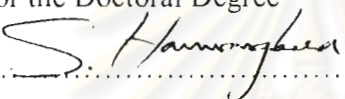
By Mr. Rachsak Sakdanuphab

Field of Study Physics


Thesis Advisor Assistant Professor Sojiphong Chatraphorn, Ph.D.

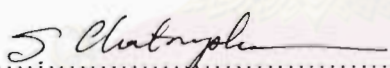
Thesis Co-Advisor Chanwit Chityuttakan, Ph.D.

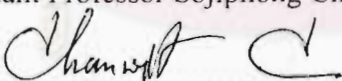
Accepted by the Faculty of Science, Chulalongkorn University in Partial Fulfillment
of the Requirements for the Doctoral Degree


 Dean of the Faculty of Science
(Professor Supot Hannongbua, Dr.rer.nat.)

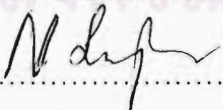
THESIS COMMITTEE

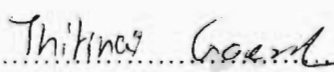
 Chairman
(Assistant Professor Rattachat Mongkolnavin, Ph.D.)

 Thesis Advisor
(Assistant Professor Sojiphong Chatraphorn, Ph.D.)

 Thesis Co-Advisor
(Chanwit Chityuttakan, Ph.D.)

 Examiner
(Assistant Professor Thiti Bovornratanaraks, Ph.D.)

 Examiner
(Narumon Suwonjandee, Ph.D.)

 External Examiner
(Associate Professor Thitinai Gaewdang, Ph.D.)

ราชศักดิ์ คักดานุภาพ : อิทธิพลของโซเดียมในกระบวนการประดิษฐ์เซลล์สุริยะชนิดฟิล์มบางคอปเปอร์อินเดียมแกลเลียมไดซลีไนต์ประสิทธิภาพสูง. (INFLUENCE OF SODIUM IN FABRICATION PROCESS OF HIGH EFFICIENCY Cu(In,Ga)Se_2 THIN FILM SOLAR CELLS) อ.ที่ปรึกษาวิทยานิพนธ์หลัก : ผศ.ดร.โคจิพงศ์ ฉัตรภรณ์, อ.ที่ปรึกษาวิทยานิพนธ์ร่วม: อ.ดร.ชาญวิทย์ จิตยุทธการ, 91 หน้า.

อิทธิพลของ Na ที่มีต่อเซลล์สุริยะชนิดฟิล์มบางคอปเปอร์อินเดียมแกลเลียมไดซลีไนต์ถูกศึกษาโดยใช้ NaF ปรี่เคอเซอร์ ในกระบวนการปลูกฟิล์มแบบสามชั้นตอน สเปกตรัมการเลี้ยวเบนรังสีเอกซ์แสดงการเพิ่มขึ้นของระนาบ (112) ที่ขึ้นกับความหนาของ NaF ปรี่เคอเซอร์ ซึ่งนำไปสู่การเกิดลักษณะของเกรนที่แหลมโดยดูได้จากพื้นผิวของฟิล์ม เซลล์สุริยะที่เตรียมโดยใช้ NaF ปรี่เคอเซอร์ มีการเพิ่มขึ้นของค่า open-circuit voltage, ค่า fill factor และค่าการแปลงประสิทธิภาพอย่างมีนัยสำคัญ ซึ่งปริมาณโซเดียมภายในฟิล์มที่เหมาะสมที่สุดสำหรับงานวิจัยนี้มีค่าประมาณ 0.25 at.% และได้ค่าประสิทธิภาพสูงสุดที่ 16 % ในงานวิจัยนี้ได้มีการนำเสนอแบบจำลองอย่างง่ายของการปลูกฟิล์ม ภายใต้อิทธิพลของโซเดียมในกระบวนการแบบสามชั้นตอนเพื่ออธิบายกลไกการปลูกฟิล์มและกลไกการเพิ่มของพหุภายในฟิล์ม ในระหว่างชั้นตอนที่หนึ่ง Na จะคงอยู่ที่ด้านล่างและส่งผลต่อการเปลี่ยนแปลงระนาบของฟิล์ม $\gamma\text{-(In,Ga)}_2\text{Se}_3$ โดยจะทำให้เกิดการเพิ่มขึ้นของระนาบ (105) จากนั้นในชั้นตอนที่สอง Na จะมีการรวมตัวเกิดเป็นสารประกอบ เช่น Na(In,Ga)Se_2 และ Na_2Se_2 ผสมอยู่ในฟิล์ม CIGS และ Cu_{2-x}Se สารประกอบเหล่านี้จะไปลดการเกิดของระนาบ (220)(204) และทำให้ฟิล์มมีความขรุขระกับการเริ่มเกิดลักษณะของเกรนที่แหลมขึ้น ในชั้นตอนสุดท้ายสารประกอบของ Na จะมีการแยกตัวทำให้เกิดอะตอม Na อิสระ ซึ่งจะแพร่ไปที่บริเวณผิวฟิล์มโดยทิ้งที่ว่างของอะตอม Na เอาไว้บริเวณตามขอบเกรน การเพิ่มขึ้นของพหุมีความสัมพันธ์กับการเกิดสารประกอบของ Na และความบกพร่องชนิดที่ว่าง Na ภายในฟิล์ม ซึ่งสามารถสังเกตได้จากการเพิ่มขึ้นของค่า open-circuit voltage

ภาควิชา ฟิสิกส์

สาขาวิชา ฟิสิกส์

ปีการศึกษา 2553

ลายมือชื่อนิสิต ราชศักดิ์ คักดานุภาพ

ลายมือชื่อ อ.ที่ปรึกษาวิทยานิพนธ์หลัก

ลายมือชื่อ อ.ที่ปรึกษาวิทยานิพนธ์ร่วม อ.ดร.ชาญวิทย์ จิตยุทธการ

4973839223 : MAJOR PHYSICS

KEYWORDS : THIN FILM SOLAR CELL / Cu(In,Ga)Se₂ / MBD / NaF / SODIUM PRECURSOR

RACHSAK SAKDANUPHAB : INFLUENCE OF SODIUM IN FABRICATION PROCESS OF HIGH EFFICIENCY Cu(In,Ga)Se₂ THIN FILM SOLAR CELLS. THESIS ADVISOR : ASST. PROF. SOJIPHONG CHATRAPORN, Ph.D., THESIS CO-ADVISOR : CHANWIT CHITYUTTAKAN, Ph.D. 91 pp.

Influence of Na on Cu(In,Ga)Se₂ thin film solar cells were studied by using a NaF precursor in the three-stage deposition process. The X-ray diffraction spectra showed the increasing of (112) preferred-orientation with the thickness of NaF precursor leading to the increase of sharp grains seen on surface morphology. The CIGS thin film solar cells using NaF precursor showed a significant increase of **the open-circuit voltage**, the fill factor and the conversion efficiency. The optimum Na concentration in the CIGS film was approximately 0.25 at.% to achieve the best cell efficiency of 16 % in this work. A simplified Na-assist growth model in the three-stage process was introduced to explain growth mechanism and doping mechanism. It was proposed that Na located at the bottom, during the first stage, affected the preferred orientation of γ -(In,Ga)₂Se₃ film by enhancing (105) orientation. Then, Na formed Na-related compounds, e.g. Na(In,Ga)Se₂ and Na₂Se₂ in the mixture of CIGS and Cu_{2-x}Se compounds in the film during the second stage. They reduced (220)(204) orientations of CIGS film and enhanced roughness with slightly sharper grain. Finally, the Na compounds decomposed and contributed to free Na atoms which were then driven to the surface thus leaving the vacancies around the grain boundaries. The increase of doping was related to the formation of Na compounds and the Na vacancy defects in CIGS thin film which could be observed from the increase of the open-circuit voltage.

Department : Physics

Student's Signature *R. Sakdanuphab*

Field of Study : Physics

Advisor's Signature *S. Chatraporn*

Academic Year : 2010

Co-Advisor's Signature *C. Chityuttakan*

Acknowledgments

I would like to express my gratitude to my thesis advisors, Assistant Professor Dr. Sojiphong Chatraphorn and my thesis co-advisors, Dr. Chanwit Chityuttakan for their suggestion and advice throughout the course of this dissertation. I am also grateful to Assistant Professor Dr. Rattachat Mongkolnavin, Assistant Professor Dr. Thiti Bovornratanaraks, Dr. Narumon Suwonjandee and Associate Professor Dr. Thitinai Gaewdang for serving as the committee. All of whom have made valuable comments and have been helpful in the production of this dissertation.

I would like to thank Semiconductor Physics Research Laboratory (SPRL) for supporting the facilities and members of SPRL; Dr. Panita Chinvetkitvanich, Mr. Bancha Athibenjukul and Dr. Kriangkrai Wantong as well as master degree students who teach and collaborate with during the study.

I would like to acknowledge the financial supports from Development and Promotion of Science and Technology talents project (DPST), the National Research Council of Thailand (NRCT), the 90th Anniversary of Chulalongkorn University Fund (Ratchadaphisek-somphot Endowment Fund) and Thailand Center of Excellence in Physics (ThEP Center).

I would like to thank the Department of Geology, Faculty of Science, Chulalongkorn University for allowing me to use their XRD. Also the access to SEM at the Department of Physics, King Mongkut's University of Technology Thonburi, KMUTT and AES at Thai Microelectronics Center, TMEC are truly appreciated.

Finally, a deep gratitude is acknowledged to my parents for encouragement throughout the entire study.

Contents

	Page
Abstract (Thai)	iv
Abstract (English)	v
Acknowledgement	vi
Contents	vii
List of Tables	x
List of Figures	xi
Chapter I Introduction	1
1.1 Overview.....	1
1.2 Literature review of models of Na effects.....	4
1.3 Scope of this Dissertation.....	6
Chapter II Theoretical Background	8
2.1 Principle of solar cell	8
2.1.1 The electrical property of a solar cell.....	10
2.2 Physical Vapor Deposition (PVD).....	12
2.2.1 The physics and chemistry of evaporation.....	12
2.2.2 Evaporation of multi-element material.....	14
2.3 Cu(In,Ga)Se ₂ material.....	15
2.3.1. Optical Property of Cu(In,Ga)Se ₂ material.....	15
2.3.2. The variation of band gap in CIGS material.....	17
2.3.3. Structural properties of Cu(In,Ga)Se ₂	18
2.4 Formation of CuInSe ₂ , CuGaSe ₂ and Cu(In,Ga)Se ₂ compounds... ..	20
2.4.1 Phase diagram of Cu-In-Se system.....	20
2.4.2 Phase diagram of Cu-Ga-Se system.....	21
2.4.3 Phase diagram of Cu-In-Ga-Se system.....	22
2.5 Defect in Cu(In,Ga)Se ₂ compound	22
Chapter III Experimental procedure	24
3.1 Fabrication processes of CIGS thin film.....	24
3.1.1 Single stage process.....	24
3.1.2 Two stage process.....	24

3.1.3 Three stage process.....	26
3.1.4 Band gap grading.....	28
3.2 <i>in situ</i> monitoring and end point detection.....	30
3.3 Device structure and solar cell processing.....	32
3.3.1 Substrate preparation.....	32
3.3.2 Mo back contact.....	33
3.3.3 CdS buffer layer.....	35
3.3.4 ZnO bilayer window.....	36
3.3.5 Ni-Al grid.....	37
3.3.6 Molecular beam deposition technique and MBE system	38
3.3.7 Calculation of the CIGS deposition process.....	40
3.4 Characterizations.....	42
3.4.1 Scanning electron microscope (SEM).....	42
3.4.2 X-ray diffraction (XRD)	43
3.4.3 Chemical characterization of surface and film.....	44
3.4.4 Optical transmission and Optical reflection.....	46
3.4.5 I-V measurement	48
Chapter IV Results and Discussions.....	49
4.1 Effects of internal sodium diffusion and external sodium fluoride precursor in Cu(In,Ga)Se ₂ thin film solar cells.....	49
4.1.1 Surface morphology and cross section.....	50
4.1.2 Structural Property.....	54
4.1.3 Auger Electron Spectroscopy (AES) Depth Profiling.....	56
4.1.4 Device Performance.....	58
4.1.5 The relation between atomic concentration of Na and the doping levels in CIGS thin film.....	60
4.2 Evolution of Cu(In,Ga)Se ₂ thin film using Na precursor in 3-stage growth process.....	63
4.2.1 Crystal structure.....	64
4.2.2 Surface morphology.....	68
4.2.3 Cross-section images.....	70

	Page
4.2.4 AES depth profiles.....	71
Chapter V Growth and doping mechanisms.....	74
Chapter VI Conclusions	77
References	79
Appendices	85
Appendix A List of Abbreviations	86
Appendix B List of Conferences	88
Appendix C List of Publications	90
Vitae.....	91



ศูนย์วิทยทรัพยากร
จุฬาลงกรณ์มหาวิทยาลัย

List of Tables

	Page
1.1 Chemical composition of soda lime glass (SLG) Ref. U.S. Department of Energy, National Center for Photovoltaics, NREL.....	3
2.1 The chemical reaction during the evaporation phenomena in compound where M = metal, X = nonmetal.....	15
2.2 Theoretical variation of the lattice parameters a and c in chalcopyrite alloys calculated from Vegard's law for $\text{Cu}(\text{In}_{1-x}\text{Ga}_x)\text{Se}_2$	19
2.3 Formation energies of intrinsic defects in CuInSe_2	23
2.4 Majority defect pair in CuInSe_2 under the condition an excess of In_2Se_3 with an excess or deficiency of selenium (ΔS).....	23
3.1 Density and molecular mass of the material used in CIGS fabrication.....	41
4.1 Crystal parameters of the CIGS film grown on difference Na contents calculated from the XRD spectra.....	56
4.2 Device performances of the CIGS thin film solar cells using various Na content substrates.....	59
4.3 Density per molecular mass ratio of Cu, In, Ga, Se and NaF.....	60
4.4 Number of each evaporated atoms per unit area in the CIGS film at $y = 0.9$	61
4.5 The ratio of $[\text{Na}]/[\text{Cu}]$ and at. % Na with the solar cell parameter such as open-circuit voltage and solar cell efficiency.....	61

List of Figures

	Page
1.1 Evolution of the different solar cell performances [NREL].....	2
2.1 A Simple diagrams of the generated electron-hole pair at the p-n junction	9
2.2 Energy band diagram of a homojunction i.e. c-Si or multi-Si solar cells...	9
2.3 Energy band diagram of heterojunction CIGS based thin film solar cells..	10
2.4 Equivalent circuit diagram of solar cell and I-V characteristic of solar cell	12
2.5 Relation between vapor pressure and the temperature of several materials	14
2.6 Standard solar spectrum of space and terrestrial (American Society for Testing and Materials (ASTM)).....	16
2.7 Absorption spectrum of CuInSe ₂ compared with that of other photovoltaic.....	16
2.8 Ideal solar cell efficiency as a function of band gap energy at AM 1.5.....	18
2.9 The chalcopyrite structure of Cu(In,Ga)Se ₂ where red atoms are Cu, gray atom are In or Ga and black atom are Se.....	19
2.10 Phase diagram along the Cu ₂ Se and In ₂ Se ₃ for the formation of CuInSe ₂ compound.....	20
2.11 Phase diagram of Cu ₂ Se and Ga ₂ Se ₃ for a formation of CGS compound..	21
2.12 Isothermal quasi-ternary Cu ₂ Se–In ₂ Se ₃ –Ga ₂ Se ₃ phase diagram where Ch is the α -phase, P1 is the β -phase, P2 is the γ -phase or layered structure and Zb is the δ -phase.....	22
3.1 Deposition rate of any elements and the evolution of [Cu]/([In]+[Ga]) ratio (y) and [Ga]/([In]+[Ga]) ratio (x) in two-stage growth process of CIGS thin films.....	25
3.2 (a) Deposition rate of any elements and the substrate temperature. (b) Evolution of Cu-content (y) and Ga-content (x) in three-stage growth process of CIGS thin films.....	27
3.3 Schematic diagram of band gap grading profile (a) non-grading, (b) normal-grading and (c) double grading.....	29
3.4 Two-stage growth process for the CIGS film (dash line) and normal Ga-graded CIGS film (solid line) (a) and double grading (b).....	29

3.5	<i>in situ</i> monitoring consisting of pyrometer and heating output power during the CIGS growth.....	30
3.6	<i>in situ</i> monitoring signal i.e. heating output power and pyrometer from 3-stage growth process (a) pyrometer signal and (b) heating output power Signal.....	31
3.7	Schematic diagram of a structural Cu(In,Ga)Se ₂ solar cell.....	32
3.8	Surface morphology of Mo film on SLG using the single-layer process from Atomic Force Microscopy.....	34
3.9	Thermal evaporation system of Ni-Al grid.....	38
3.10	Molecular beam epitaxial system (EIKO model EW-100) containing growth chamber, evaporation sources, temperature controller and real-time monitoring.....	39
3.11	Deposition rates of elemental sources; NaF, Cu, In, Ga and Se in MBE system calibrated by QCM.....	40
3.12	Schematic of the scanning electron microscope.....	42
3.13	(a) Electron and photon signals emanating from tear-shaped interaction volume during electron-beam impingement on specimen surface. (b) Energy spectrum of electrons emitted from specimen surface. (c) Effect of surface topography on electron emission.....	43
3.14	X-ray diffraction in crystal lattice satisfied the Bragg's condition.....	44
3.15	Schematic diagrams of AES in depth profile mode consisting Ar ⁺ -gun, electron gun and electron detector.....	45
3.16	Electron configurations of an atom and the Auger electron process.....	46
3.17	Optical transmittance and optical reflectance of CIGS thin film grown by 3-stage process.....	47
3.18	Absorption coefficient of the CIGS film calculated from %T, %R and thickness of the CIGS film.....	48
4.1	CIGS thin films fabricated on different substrate and addition of NaF precursor.....	50
4.2	Surface morphologies of the CIGS films grown on (a) Mo/Al ₂ O ₃ /SLG (b) NaF(100Å)/Mo/Al ₂ O ₃ /SLG and (c) Mo/SLG substrates.....	51

4.3	Cross-sectional images of the CIGS films grown on (a) Mo/Al ₂ O ₃ /SLG, (b) Mo/SLG and (c) NaF(100Å)/Mo/Al ₂ O ₃ /SLG (d)NaF(200Å)/Mo/SLG..	53
4.4	BEI Cross-sectional images of the CIGS films grown on (a) Mo/Al ₂ O ₃ /SLG and (b) NaF(100Å)/Mo/Al ₂ O ₃ /SLG.....	54
4.5	Cross-sectional images of the CIGS films grown on Mo/Al ₂ O ₃ /SLG from FSEM in secondary electron and BEI modes (circle indicates Cu _{2-x} Se)....	54
4.6	XRD spectra of the CIGS films grown on (a) Mo/Al ₂ O ₃ /SLG, (b) Mo/SLG, (c) NaF(100Å)/Mo/Al ₂ O ₃ /SLG and (d) NaF(200Å)/Mo/SLG...	55
4.7	Comparative XRD spectra of the CIGS films grown on difference Na contents.....	56
4.8	AES depth profiling for the CIGS film grown on (a) NaF (100Å)/Mo/Al ₂ O ₃ /SLG and (b) Mo/SLG.....	57
4.9	The depth profile of Na distribution and [Ga]/([In]+[Ga]) ratio in CIGS film grown on (100Å)/Mo/Al ₂ O ₃ /SLG substrate.....	58
4.10	Solar cell parameters such as J _{sc} , FF, V _{oc} and η of CIGS cells grown with various at. % Na.....	62
4.11	Three-stage growth profile and the interested points in the growth process.....	63
4.12	XRD spectra of the films at the end of each stage; at first stage: (a) with NaF, (b) without NaF; at the transition temperature: (c) with NaF, (d) without NaF; at the end of second stage: (e) with NaF, (f) without NaF; and at EPD:(g) with NaF, (h) without NaF.....	66
4.13	Gaussian fitting XRD spectra of the films at the end of the 2 nd stage consisting of (112) and (220)(204) CIGS orientations as well as (111) and (022) Cu _{2-x} Se orientations.....	67
4.14	Gaussian fitting XRD spectra of the CIGS films at EPD consisting of (112) and (220)(204) orientation.....	67
4.15	Surface morphology of the films at the end of each stage; at first stage: (a) with NaF, (b) without NaF; at the transition temperature: (c) with NaF, (d) without NaF; and at the end of second stage: (e) with NaF, (f) without NaF; and at EPD: (g) with NaF, (h) without NaF.....	69

4.16 SEM cross-section images of the films at the end of the second stage: (e) with NaF, (f) without NaF; and at EPD: (g) with NaF, (h) without NaF.....	70
4.17 AES depth profiles of Na atoms in the films with NaF precursor; (a) end of first stage, (c) at transition temperature, (e) end of second stage, and (g) at EPD.....	72
4.18 [Ga]/([In]+[Ga]) ratio in CIGS film with (g) and without (h) NaF precursor.....	72
4.19 Variation of [Ga]/([In]+[Ga]) ratio in depth profiles of the films at interrupted points.....	73
5.1 Schematic diagram of the CIGS growth model in 3-stage growth process with Na precursor.....	75

CHAPTER I

INTRODUCTION

1.1 Overview

Solar energy is one of alternative sources of energy. It reduces the CO₂ emission and other greenhouse gases that are the cause of climate change and global warming problems [1]. Solar cell is a semiconductor device that can directly convert the photon energy into the electrical energy by using a photovoltaic (PV) effect. In 1839, the photovoltaic effect was discovered by Becquerel and then a solar cell was produced at Bell Laboratory in 1950 by using single crystal silicon [2]. The silicon wafer was diffused to form a p-n junction with group III and group VI elements, respectively. The primary solar cells were mostly used to generate the electricity in space applications (e.g. spacecraft, space station and satellite). Silicon solar cell is the 1st generation PV. The achievement of the silicon solar cell leads to the PV market. Today, the single crystalline and polycrystalline silicon solar cells share about 80 percent of PV market [3]. Scientists have found new photovoltaic materials and methods which have a potential to reduce the manufacturing cost and gain the device efficiency. Over the past three decades, the technology of solar cell has been developed in order to achieve higher electrical conversion efficiency. Thin film solar cells were emerged in 1970. Solar cells based on thin film technology have attracted commercials because of their high efficiency, low material usage and high yield processes. The thin film solar cells such as amorphous (hydrogenated) silicon (a-Si:H), CdTe and Cu(In,Ga)Se₂ are the 2nd generation of PV technology. The thin-film PV market shows a spectacular annual growth rate of 126% in 2007 [4]. The 3rd generation of PV started in 1991. A photo electrochemical reaction based solar cells i.e. dye-sensitized cells was firstly invented by Michael Grätzel and Brian O'Regan at the École Polytechnique Fédérale de Lausanne [5]. It is presently very interesting because of the easier processes (non vacuum) and the dramatically lower cost. However, these cells still have short term stability and unreliability in outdoor operation.

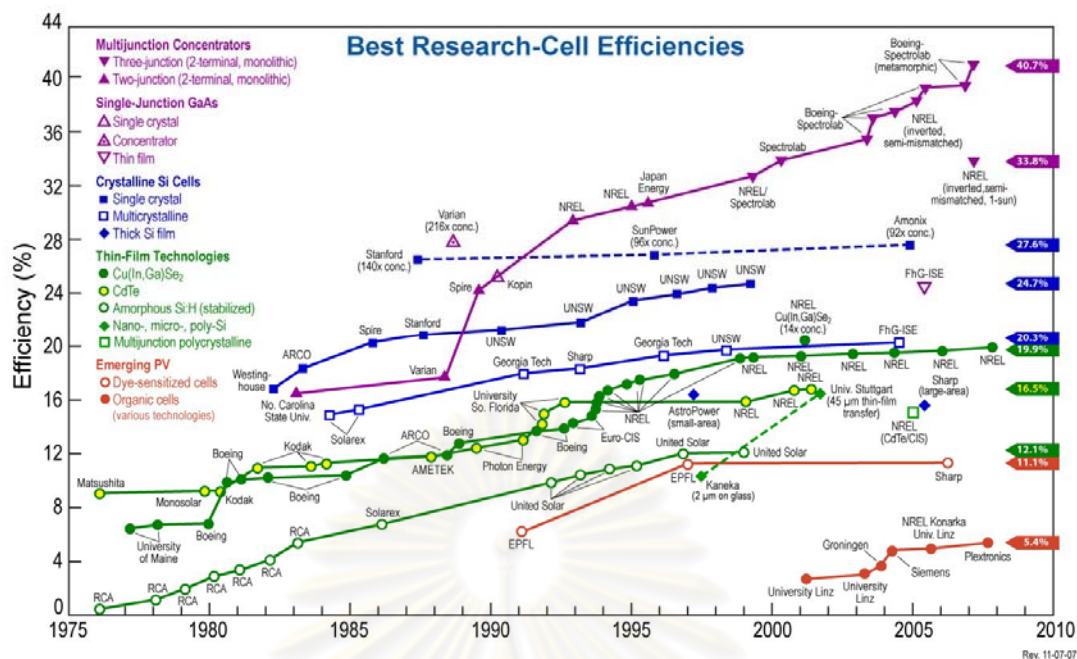


Figure 1.1 Evolution of the different solar cell performances [Ref: U.S. Department of Energy, National Center for Photovoltaics, NREL].

In order to achieve the highest efficiency, the multijunction solar cells or namely tandem cells are fabricated for absorbing photons almost the whole solar spectrum. III-VI compounds e.g. GaAs, and GaInP₂ have been studied for multijunction solar cells using metalorganic vapour phase epitaxy growth. The evolution of the performances of different solar cells is shown in Fig. 1.1.

One of the most interesting thin film solar cells is Cu(In,Ga)Se₂ or CIGS based solar cells. CIGS solar cells are the 2nd generation of solar cells which have the highest efficiency solar energy conversion. The world record of CIGS solar cells efficiency in the lab scale is almost 20 percent demonstrated by NREL [6]. Today, they are used in many applications such as solar power plants, power supply in aerospace and portable purposes. The portable devices now use flexible solar cells as electrical generators for reducing their weight and size. CIGS solar cells are gaining more attraction from the energy investors and the government. The CIGS solar cell industries are widely established in many countries such as USA (Day Star Technologies), Germany (WürthSolar), Japan (Honda), etc. [3].

Cu(In,Ga)Se₂ is a ternary compound semiconductor of the I-III-VI group. It has been demonstrated for the sufficiently long term stability and high absorption coefficient so it is used as the photon absorber in high efficiency thin film solar cell [7,

8]. The structure of the CIGS solar cell consists of Ni-Al grid/ZnO/CdS/CIGS/Mo layers. The heterojunction of CIGS solar cells is constructed by the difference of semiconducting materials with unequal energy gaps. The p-n junction is formed between ZnO/CdS as the n-type semiconductors and Cu(In,Ga)Se₂ as the p-type semiconductor. Mo and Ni-Al grid are back and front electrical contact, respectively. CIGS is a direct band gap material whose bandgap energy can be adjusted from 1.04-1.68 eV by varying the ratio of group III elements. This property is very interesting for band gap engineering. The p-type CIGS is generally doped by native defects such as vacancies, interstitial and antisite defects which contribute as the acceptors to increase the conductivity. The native defects occur during the growth process and depend on the impurity and composition of the CIGS films at the end of the process. The non-equilibrium process, e.g. a three-stage process has been developed to enhance native defects for obtaining higher doping levels in the CIGS films. In general, the standard CIGS thin film solar cells using a soda-lime glass (SLG) as a substrate are unintentionally doped with an impurity in the substrate whose compositions are illustrated in Table 1.1. The important compounds of alkaline elements in the SLG such as sodium (Na) and potassium (K) are induced as the native defects to enhance the device efficiency. However, the amount of Na that diffuses from the SLG substrate through the Mo film into the CIGS film during the growth cannot be easily controlled and identified. It depends on the SLG properties, substrate temperature during the growth process and the properties of Mo film which allow the Na diffusion.

Table 1.1 Chemical composition of soda lime glass (SLG) [Ref: U.S. Department of Energy, National Center for Photovoltaics, NREL].

Material	Composition (%)
SiO ₂	72.8
Na ₂ O	12.7
CaO	8.1
MgO	3.8
Al ₂ O ₃	1.4
K ₂ O	0.8
Other (Fe)	0.4

The optimum concentration of Na in the CIGS film is only 0.1 atomic percent to achieve high efficiency cells [9]. In addition, the small amount of internal Na diffusion from the SLG substrate enhances several positive effects to the CIGS films and the performance of the solar cells when forming the p-n junction. The role of Na mainly affects the conductivity of absorber layer or doping levels of the CIGS film which corresponds to the native defects [10]. Many researchers have shown the improvement of morphology, orientation, and grain size by sodium enhancement in the CIGS thin films [11, 12]. The cell performance consisting of the open-circuit voltage and the fill factor substantially increase [13]. However, the limitation of Na diffusion from the SLG is presently not fully understood in details. Thus Na from an external source is then needed for controlling the quantity of Na. Moreover, this is a basic requirement for fabricating the CIGS solar cells on flexible substrates such as metallic foils or polymer sheets [14]. According to the previous works, the effects of Na on the CIGS solar cell have been observed in many laboratories e.g. A. N. Tiwari's group in Switzerland and L. Stolt's group in Sweden, etc. The varieties of the model have been proposed to explain the Na effects in the CIGS material and the solar cell based on their experimental results. However, these models are still inconsistent. For a general agreement, Na affects the electronic property by enhancing the carrier concentration and the film conductivity, and thus improves the solar cell efficiency. In contrast, there is a conflict of Na effects in the structural property. The presence of Na during the growth process affects the increase of grain size and texture observed by Granath *et al.* but Rudmann *et al.* found the decrease of grain size when incorporated with Na [12, 15]. The structural effects seem to be a main problem that depends on the conditions of the growth process. In order to understand the problems, I focus on the growth mechanism with Na incorporation during the growth process and compare the experimental results with the previous works by others. A growth model will be introduced to explain the growth mechanism and doping mechanism under Na incorporation.

1.2 Literature review of models of Na effects

There are several models of Na effects in the CIGS films which can be classified into three categories based on the experimental observations. The first model suggests the substitution of Na in the CIGS structure. The substitution of Na onto In or Ga sites

($Na_{(In,Ga)}$) helps increasing the hole carriers because $Na_{(In,Ga)}$ acts as an acceptor. In addition of the substitution of Na into Cu site (Na_{Cu}) helps reducing In or Ga atoms on Cu sites ($(In,Ga)_{Cu}$) which acts as a donor by forming a neutral defect [10,16]. Therefore, the substitution of Na in the CIGS structure causes the change of electronic property in the CIGS by enhancing the p-type doping and thus reducing the n-type doping. In the second model, Na behaves as a surfactant during the growth of the CIGS. It destabilizes ($2V_{Cu}+In_{Cu}$) neutral defect complexes in the near-surface region, and thus reduces the amount of In_{Cu} compensating donors as well as enhances the crystal quality of the CIGS [17, 18]. In addition, the advantages of the surfactant are the suppression of β -phase CIGS formation and expand the range of α -phase CIGS formation as described by Granata and Sites [19], Herberholz and co-workers [9]. D. Rudmann *et al.* proposed that Na especially passivates at the grain boundaries and surfaces because of the very low solubility in the CIGS single crystal [20]. Then, they claimed the Na effects in the CIGS caused by Na acting only at the grain boundaries. Rockett *et al.* suggested that Na improves the cell performance primarily via grain boundaries by changing in the electronic properties. Na increases atomic mobility during the growth of the CIGS at the grain boundaries, and thus will increasing the grain size due to the decrease of energy at the surfaces [21]. The third model is not the direct effect of Na on the CIGS. It assumes that Na on the surface catalyzes O_2 dissociation which supplies oxygen in the CIGS. Kronik *et al.* proposed that the increased hole density is due to the occupation of Se vacancies (V_{Se}) with oxygen atom. The V_{Se} acts as a donor but the substitution of O atom into V_{Se} acts as a neutral defect. Therefore, O atoms help reducing the n-type doping and introducing an acceptor [22].

According to the theoretical calculation, the first principle calculation of Na effects on the electrical and structural properties of $CuInSe_2$ was introduced by S. H. Wei, S. B. Zhang, and Alex Zunger [23]. They divided the Na effects into three main types on $CuInSe_2$ by determining the quantity of Na in the $CuInSe_2$ crystal and the possibility of catalyzing oxygen dissociation. They calculated the formation energies and the transition energy levels involving point defects e.g. Na_{Cu} , Na_{In} , V_{Se} , and O_{Se} in $CuInSe_2$. The Na models were clarified with their calculation results. They proposed that: (1) There is a formation of phase separation of the $NaInSe_2$ and the alloy $Na_xCu_{1-x}InSe_2$ which are the precipitation of a secondary phase on the surfaces or the grain

boundaries at large Na concentration. Na atom will replace Cu site and forms a more stable NaInSe₂ compound that have a larger band gap and lead to the higher open-circuit voltage. The NaInSe₂ compound increases the (112) morphological texture. (2) When small quantities of Na are introduced to the CuInSe₂, Na will form Na-on-Cu defect (Na_{Cu}) and Na-on-In antisite Na_{In} defect. Na-on-Cu site does not create levels in the band gap, while Na on In site creates acceptor levels that are shallower than Cu_{In} . Therefore, Na_{In} can effectively reduce the In_{Cu} donors and thus significantly enhance the effective hole density. In addition, the quenching of In_{Cu} as well as V_{Cu} by Na enhancement reduces the stability of the ($2V_{Cu}+In_{Cu}$) and thus suppresses the formation of the ordered defect compounds. (3) They found the possibility of oxygen atom substituting in Se vacancies (V_{Se}) when determining the heat reaction of oxygen substitution in Se vacancy. Na induces oxygen point defects on the surface of Cu(In,Ga)Se₂ known as a catalyze dissociation of O₂ into atomic oxygen.

1.3 Scope of this dissertation

This dissertation is concentrated on the growth of CIGS thin films with Na incorporation by using molecular beam deposition technique. The two main Na sources are from the internal Na diffusion from the SLG substrate and the NaF evaporating source. They are studied and compared with each other. Al₂O₃ layer is used as a Na diffusion barrier in this study. The properties of the CIGS films grown on the Mo/Al₂O₃/SLG substrate such as crystal orientation, surface morphology and chemical composition are investigated and compared with the standard CIGS grown on Mo/SLG substrate. Then, the use of Sodium-Fluoride (NaF) as a Na precursor, the improvement of the device performances by adding an ultra-thin layer of NaF on Mo/SLG substrate and Mo/Al₂O₃/SLG substrate are investigated. This can be used as the information of using NaF as a Na source for the preparation of the CIGS thin film solar cells on flexible or Na-free substrates.

This dissertation is composed of four parts. In the first part (Chapter II), an overview of the principle of solar cell, physics of physical vapor deposition and the CIGS material properties are described. The experimental details of the CIGS thin film growth by the Molecular Beam Epitaxy (MBE) system, *in situ* monitoring and fabrication of the solar cell as well as the physics of characterization techniques are explained in the second part (Chapter III). Then the experimental results and

discussions of Na effects on the structural, surface morphological properties, chemical composition of the CIGS films as well as the device performance are discussed in the third part (Chapter IV). In the fourth part (Chapter V), the growth model based on the experimental results are described including the doping mechanism of Na incorporation in the CIGS films. Finally Chapter VI is the conclusions of this dissertation.



ศูนย์วิทยทรัพยากร
จุฬาลงกรณ์มหาวิทยาลัย

CHAPTER II

THEORETICAL BACKGROUND

2.1 Principle of solar cell

Solar cell is a semiconducting device consisting of a p-n junction which can convert photon energy into the electron-hole pair and feed to an electrical circuit as seen in Fig. 2.1. The basic principle of a solar cell is based on the photovoltaic effect that can be described by a band diagram for example, a p-n homojunction (Si-solar cell) under illumination as shown in Fig. 2.2. In principle, photons with energy equal to or greater than the band gap energy are absorbed in a semiconducting material and then electron-hole pairs are created. On the other hand, photons with energy less than the band gap will pass through the material and do not convert into the electrical energy. However, a less of photon can be absorbed by trap states inside the band gap. Most of the electron-hole pairs generated by photon are transported across the junction by an internal electric field at the junction. The electric field is created from the diffusion process of electron and hole at space charge region and thus establishes a built-in potential. Electrons and holes separated by the electric field give rise to electrical voltage and current in the external circuit, however the partial electron-hole pairs which cannot go to the external load, can recombine and cause the loss of electrical current.

For the CIGS thin film solar cell, it is multi-layers of semiconducting materials combined to form a p-n junction (heterojunction solar cell). The structure of the CIGS solar cell consists of the p-type semiconductor (CIGS) and the n-type semiconductor (CdS and ZnO). The band diagram of the CIGS heterojunction solar cell as shown in Fig. 2.3 is more complicated than that of the Si-homojunction. The different semiconducting materials with unequal band gaps are combined to form a junction at the equal Fermi level. The CIGS material has an energy gap in the range of 1.04 eV - 1.68 eV and typically the gap of 1.2-1.3 eV are used to obtain the high efficiency solar cells. The energy gap of the CdS and the ZnO n-type semiconductors are about 2.4 eV and 3.3 eV, respectively. A little spike is created at the junction between the CIGS and the CdS. The spike is expected to reduce the interface recombination and increase the built-in potential. Note that, when the wider band gap

CIGS (high Ga concentration) is needed, the CdS layer becomes inappropriate due to the absence of the spike. ZnS buffer layer ($E_g \approx 3.8$ eV) is usually used instead of the CdS layer.

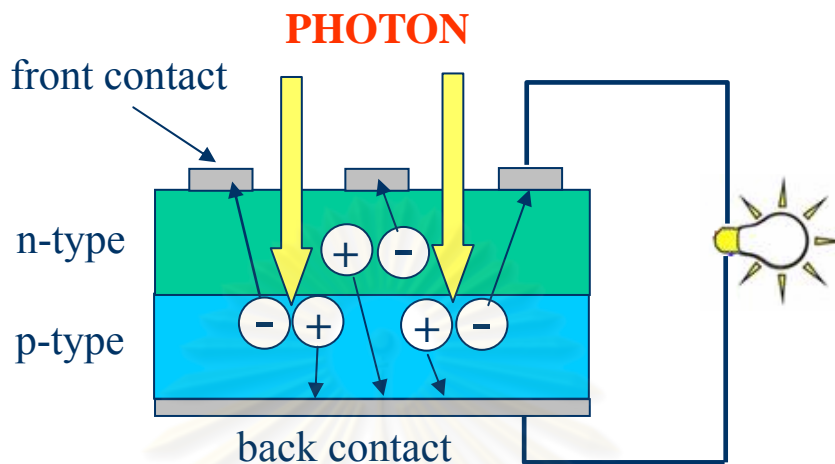


Figure 2.1 A simple diagram of the generated electron-hole pair at the p-n junction.

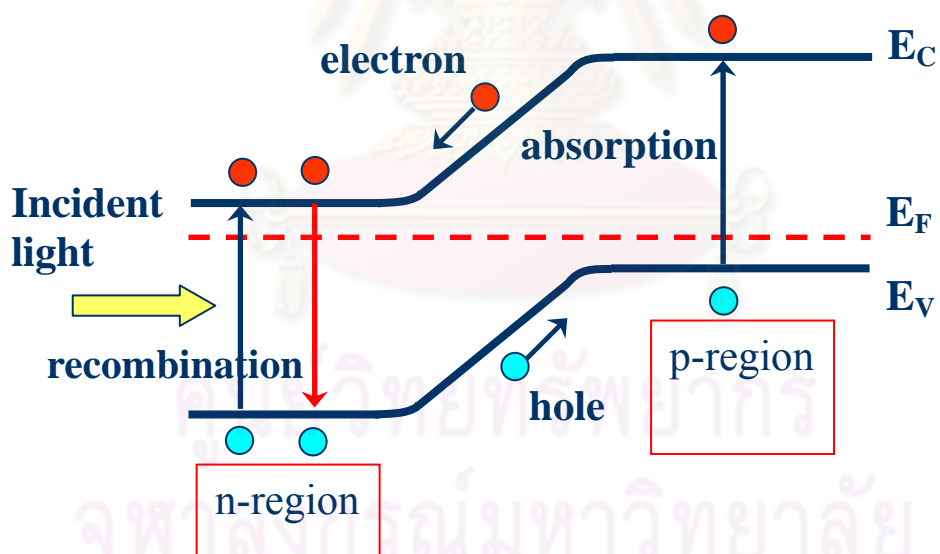


Figure 2.2 Energy band diagram of a homojunction, e.g. c-Si or multi-Si based solar cells.

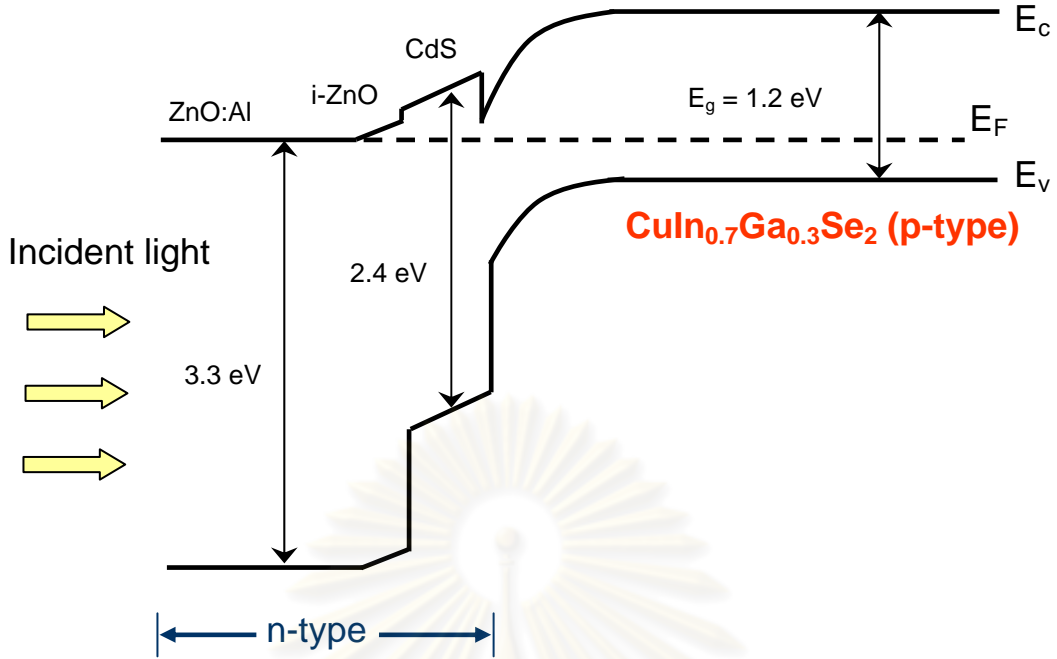


Figure 2.3 Energy band diagram of heterojunction CIGS based thin film solar cell.

2.1.1 The electrical property of a solar cell

The current-voltage characteristic (I-V curve) of the solar cell can be measured by applying an external voltage to the device with and without illumination of light. The I-V curve without illumination (dark mode) can be described by the Shockley-diode equation

$$I_D = I_0 \left(e^{\frac{qV}{AkT}} - 1 \right), \quad (2.1)$$

where I_D is the diode current flowing through device, I_0 is the leakage current or reverse saturation current, q is the electrical charge, V is the bias voltage, A is the diode quality factor, k is Boltzmann's constant and T is the temperature of the device [2]. The p-n junction under the illumination (light mode) at a zero bias ($V=0$), electron-hole pairs are generated from photon absorption. The electrons are swept to the n-side, and the holes are swept to p-side by the electric field across the junction as described previously. Therefore, the junction generates a current known as photocurrent (I_L) in the short-circuited device. The photocurrent is a drift current that has an opposite direction with the forward bias diffusion current (I_D) in dark mode. Thus, the Shockley-diode equation under illumination changes to

$$I = I_D - I_L = I_0 \left(e^{\frac{qV}{AkT}} - 1 \right) - I_L \quad (2.2)$$

where I is total current, I_L is the photocurrent at zero bias and I_D is the forward bias

diffusion current. The equivalent circuit of the single junction solar cell and I-V curve are shown in Fig. 2.4. The circuit consists of a current generator in parallel with a diode and a shunt resistor, leading through a series resistor to the output terminals. The series (R_s) and shunt (R_{sh}) resistances are defined as the following

$$R_s = \frac{\partial V}{\partial I}, \text{ at } V = V_{oc} \text{ and } R_{sh} = \frac{\partial V}{\partial I}, \text{ at } V = 0 \quad (2.3)$$

The series resistance is the resistance of the overall solar cell device and the shunt resistance indicates the leak path or tunneling pathways at the p-n junction. Two parameters can be used to describe the quality of p-n junction at which the low R_s and the high R_{sh} are appropriated for the solar cell. In general, the performance of solar cell can be described by considering the I-V curve and the solar cell parameters such as a short-circuit current (I_{sc}), an open-circuit voltage (V_{oc}), a fill factor (FF), a series resistance and a shunt resistance as well as an efficiency (η) can be extracted. According to Eq. 2.2, the short-circuit current obtained under the short-circuit condition ($V=0$) and the open-circuit voltage obtained under the open-circuit condition ($I=0$) are given by

$$I_{sc} = I(V = 0) = I_L, \quad (2.4)$$

and

$$V_{oc} = \frac{AkT}{q} \ln\left(\frac{I_L}{I_0} - 1\right), \quad (2.5)$$

respectively. The maximum power at (I_{max} , V_{max}) of I-V curve indicates the maximum converting performance of the solar cell. The fill factor (FF) is an expression of how square the output characteristics is, given by

$$FF = \frac{V_{max} \times I_{max}}{V_{oc} \times I_{sc}}. \quad (2.6)$$

The typical values of FF for high quality junction are in the range of 0.7-0.85. Finally, the conversion efficiency (η) of solar cell can be calculated by determining the ratio of the input power (light power) and the output power (electrical power)

$$\eta = \frac{V_{max} \times I_{max}}{P_{input}} = \frac{V_{oc} \times I_{sc} \times FF}{P_{in}} \quad (2.7).$$

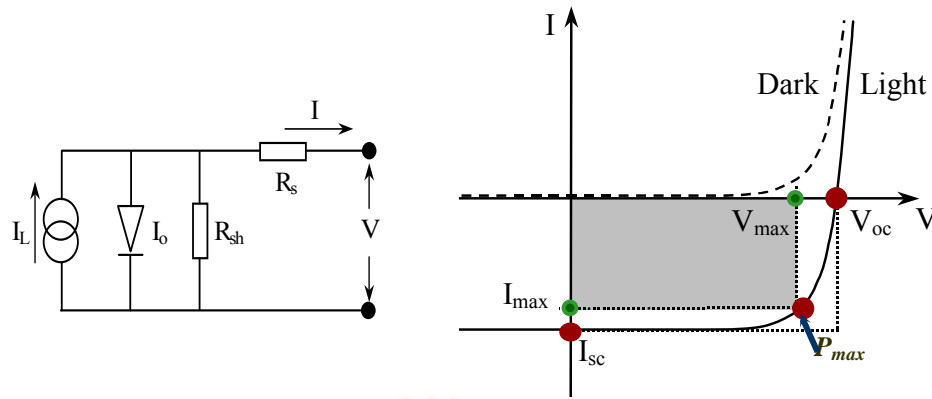


Figure 2.4 Equivalent circuit diagram of solar cell and I-V characteristic of solar cell.

2.2 Physical Vapor Deposition (PVD)

PVD is one of the most popular techniques for thin film coating in material science, nano-technology, surface engineering, etc. The PVD process generates vapor of coating material by physical methods such as thermal evaporation, electron beam, sputtering etc. and then the evaporating material deposits on the substrate surface. Usually, the PVD coating systems require high vacuum equipment for removing the contamination, e.g. O₂, N₂, H₂O etc. In addition, PVD technique can be used for many kinds of material and the physical parameters can be varied in order to obtain the desired films. In this section, the physics and chemistry of the evaporation based on the growth and the formation of films by the PVD technique are described.

2.2.1 The physics and chemistry of evaporation

In 1882, Hertz described the evaporation phenomena by his experimental measurement on the evaporation of Mercury. He found that the evaporation rates were not limited by insufficient heat supplied to the surface of the molten evaporant. It was proportional to the difference between the equilibrium pressure, P_e , of H_g at the given temperature and the hydrostatic pressure, P_h , acting on the evaporant. In addition, a liquid evaporant at a given temperature has a specific evaporating ability. If the number of emitted vapor molecules correspond to the number of required exerting the equilibrium vapor pressure, it will give a maximum evaporation rate. The evaporation rate of the liquid and solid surfaces can be expressed by

$$\Phi_e = \frac{\alpha_e N_A (P_e - P_h)}{(2\pi MRT)^{1/2}} \quad (2.8),$$

where Φ_e is the evaporation flux in number of atoms or molecules per unit area, per

unit time, and α_e is the coefficient of evaporation which has a value between 0 and 1 [24]. The maximum rate will be given when $\alpha_e = 1$ and P_h is zero. By considering gas impingement on surfaces, the number of molecules that strike an element of surface, perpendicular to coordinate direction, per unit time and area can be written as

$$\Phi_e = \frac{3.513 \times 10^{22}}{(MT)^{1/2}} P_e \text{ molecules/cm}^2\text{s}, \quad (2.9)$$

where P_e is the equilibrium pressure expressed in Torr unit and a useful formula is

$$\Gamma_e = 5.84 \times 10^{-2} (M/T)^{1/2} P_e \text{ g/cm}^2\text{s}, \quad (2.10)$$

where Γ_e is the mass evaporation rate. For example, when the pressure is 10^{-2} Torr, a typical value of Γ_e for many elements is approximately 10^{-4} grams per second per cm^2 of evaporated area. Therefore, the temperature is more important key parameter of evaporation rates than an effect on equilibrium vapor pressure.

Another important parameter in physics of evaporation is the vapor pressure of elements. The relation between temperature and vapor pressure can be expressed by the Clausius-Clapyeron equation given by

$$\frac{dP}{dT} = \frac{\Delta H(T)}{T\Delta V} \quad (2.11)$$

This equation can be used in both solid-vapor and liquid-vapor equilibrium. The derivation of enthalpy, $\Delta H(T)$, and volume, ΔV , relate to the differences between the vapor (v) and the condensed solid or liquid phase (c), while T is the transformation temperature. By simply considering the ideal gas, the volume can be expressed by $V_v = RT/P$ and $\Delta V \approx V_v$. The Clausius-Clapyeron equation can then be rewritten as

$$\frac{dP}{dT} = \frac{P\Delta H(T)}{RT^2}. \quad (2.12)$$

When the molar heat of evaporation equals to enthalpy $\Delta H(T) = \Delta H_e$, the relation of vapor pressure can be expressed by

$$\ln P \approx -\frac{\Delta H_e}{RT} + I \quad \text{or} \quad P = P_0 e^{-\frac{\Delta H_e}{RT}}, \quad (2.13)$$

where I (or $P_0 = e^I$) is the constant from the integration.

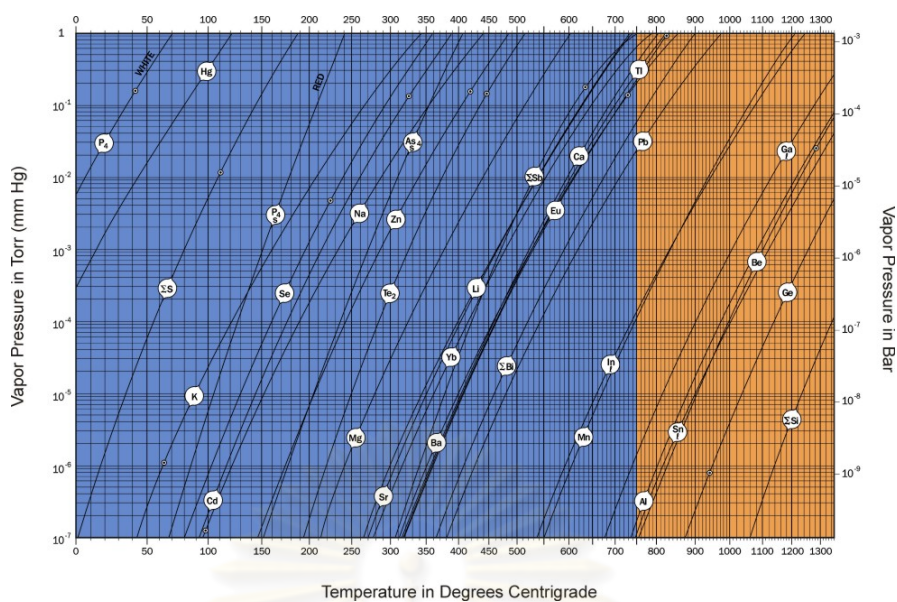


Figure 2.5 Relation between vapor pressure and the temperature of several materials.

The value of I can be determined by the substitution of ΔH_e with the latent heat of vaporization (ΔH_v), the temperature T with boiling point and 1 atm for P . This equation known as Arrhenius equation simply describes the relation between the temperature dependence and the vapor pressure in many materials over a small temperature. However, the extended range of validity of the temperature dependence of $\Delta H(T)$ must be taken into account with the thermodynamic data. For example, the vapor pressure of liquid Al is given by

$$\log P (\text{torr}) = -15,993/T + 12.409 - 0.999 \log T - 3.52 \times 10^{-6}T. \quad (2.14)$$

The Arrhenius character of $\log P$ vs $1/T$ is essentially kept by the first two terms on the right-hand side while the remaining terms are the small corrections. The relationship between the vapor pressure and the temperature of several materials is shown in Fig. 2.5.

2.2.2 Evaporation of multi-element material

In general, the evaporation of metals is in a form of evaporated atoms and clusters of atoms but the evaporation of compounds seems to be different. Inorganic compounds mostly evaporate with the change of molecule and, therefore, the vapor composition condensed is non-stoichiometry as original solid or liquid source. The molecular association and dissociation processes frequently occur in the vapor phase.

Table 2.1 The chemical reaction during the evaporation phenomena in compound where $M = \text{metal}$, $X = \text{nonmetal}$ [24].

Reaction	Chemical reaction	Examples	Comments
Evaporation without dissociation	$\text{MX}(\text{s or l}) \rightarrow \text{MX}(\text{g})$	SiO, B ₂ O ₃ , GeO, SnO, AlN, CaF ₂ , MaF ₂	Compound stoichiometry maintained in deposition
Decomposition	$\text{MX}(\text{s}) \rightarrow \text{M}(\text{s}) + 1/2\text{X}_2(\text{g})$ $\text{MX}(\text{s}) \rightarrow \text{M}(\text{l}) + 1/n\text{X}_n(\text{g})$	Ag ₂ S, Ag ₂ Se III-V semiconductors	Separate sources are required to deposit these compound Deposits are metal-rich
Evaporation with dissociation			Separate sources are usually required to deposit these compounds
(a) Chalcogenides	$\text{MX}(\text{s}) \rightarrow \text{M}(\text{g}) + 1/2\text{X}_2(\text{g})$ $X = \text{S, Se, Te}$	CdS, CdSe, CdTe SiO ₂ , GeO ₂ , TiO ₂ ,	Metal-rich discolored
(b) Oxides	$\text{MO}_2 \rightarrow \text{MO}(\text{g}) + 1/2\text{X}_2(\text{g})$	SnO ₂ , ZrO ₂	deposits; dioxides are best deposited in O ₂ partial pressure (reactive evaporation)

The reactions during evaporation phenomena in compounds can be occurred, and these are categorized briefly in Table 2.1. A troublesome decomposition of multivalent metal oxides to lower oxides can be compensated by reactive evaporation with oxygen gas.

2.3 Cu(In,Ga)Se₂ material

2.3.1. Optical Property of Cu(In,Ga)Se₂ material

The solar spectrum of the sun irradiated on the earth surface is illustrated in Fig. 2.6. AM 1.5 is a standard terrestrial solar spectral irradiance distributions on the earth surface and AM 0 is the outer space. The chalcopyrite CuInSe₂ or CIS semiconductor has been demonstrated the highest absorption coefficient when compared with that of other photovoltaic semiconductors such as CdTe, GaAs and c-Si as seen in Fig. 2.7. In addition, it has a direct band gap that the absorption coefficient does not depend on the photon energy. The absorption coefficient $\alpha(h\nu)$ of CIS is about $2 \times 10^5 \text{ cm}^{-1}$ at photon energy $h\nu = E_g + 0.2 \text{ eV}$ where E_g is the band gap energy. In principle, the absorption property of material can be expressed by

$$I(h\nu, d) = I(h\nu, 0)e^{-\alpha(h\nu)d}, \quad (2.15)$$

where I is intensity of light at photon energy $h\nu$ and d is the thickness of material [25].

The intensity of light exponentially decreases with the thickness of material. The CIS material is chosen for using as an absorber layer in high efficiency solar cells because of its effective absorption. Generally, a 1 micron thick CIS film can almost absorb the entire sun light incident on it.

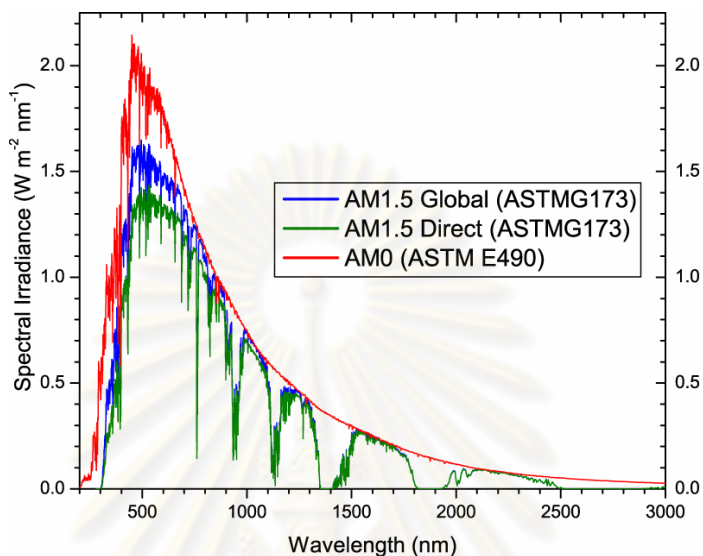


Figure 2.6 Standard solar spectrum of space and terrestrial (American Society for Testing and Materials (ASTM)) [26].

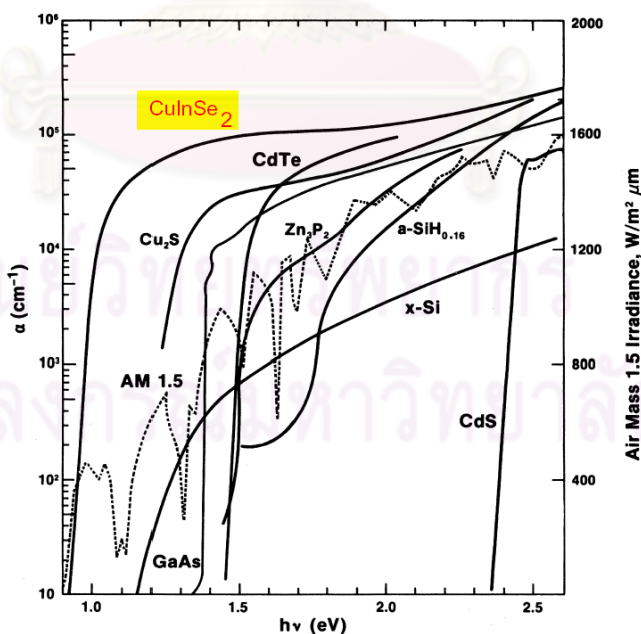


Figure 2.7 Absorption spectrum of CuInSe_2 compared with that of other photovoltaic material [27].

2.3.2. The variation of band gap in CIGS material

A special property of Cu(In,Ga)Se₂ material is that its band gap energy can be adjusted in the range between 1.04-1.68 eV by varying the ratio of group III elements; In and Ga atoms. The change of band gap is an important role to the performance of solar cell by changing the range of photon absorption and the level of built-in potential. The band gap energy of α -CuIn_{1-x}Ga_xSe₂ phase can be expressed by

$$E_{g,CIGS(x)} = (1-x)E_{g,CIS} + xE_{g,CGS} - bx(1-x), \quad (2.16)$$

where b is between 0.15-0.24 is a bowing parameter and x is [Ga]/([In]+[Ga]) ratio [28]. When the band gap increases, the range of the photon absorption decreases and then leads to the reduction of current in the device. However, the built in potential increases with the band gap and leads to the higher open-circuit voltage. A method to increase the cell efficiency is the fabrication of band gap grading. The band gap grading film can be prepared by varying the Ga ratio in depth profile. It has been shown from theoretical and simulation works elsewhere that the continuously increasing of the band gap energy towards the back contact (Mo) called band gap grading causes the electric field that assists in driving electrons in the absorber region, resulting in the increase of the minority carriers life time and diffusion length. Thus the efficiency of the solar cell is improved. The band gap grading will be discussed in the next section. The theoretical calculation of solar cell efficiency vs. the band gap is shown in Fig. 2.8. The high efficiency solar cells have been achieved with the band gap between 1.1-1.5 eV that corresponds to the solar irradiation (AM 1.5). The highest conversion efficiency is about 30%. The band gap property of materials is important for the solar cells because it relate to the output voltage and the generating current of device. The wide band gap materials lead to the high output voltage but loss in solar spectrum absorption for generating current. However, in module application, wide band gap material is preferred to obtain high output voltage.

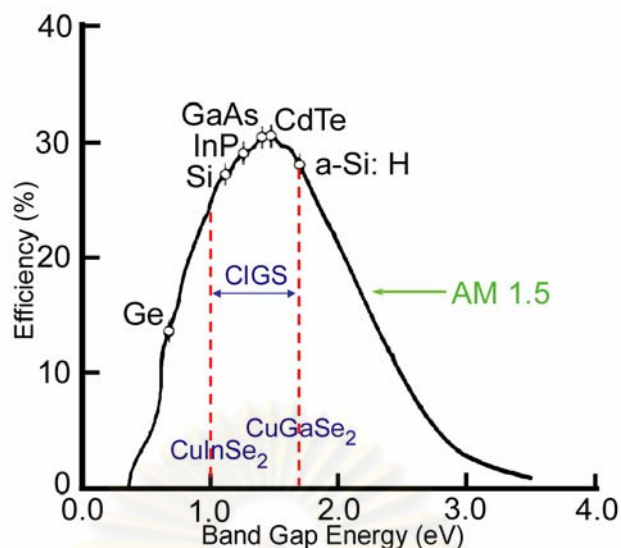


Figure 2.8 Ideal solar cell efficiency as a function of band gap energy at AM 1.5.

2.3.3. Structural properties of $\text{Cu}(\text{In,Ga})\text{Se}_2$

The crystal structure of α -CIS is a chalcopyrite at room temperature as seen in Fig. 2.9. The space group of chalcopyrite α -CIS is $I\bar{4}2d$ with a unit cell of tetragonal structure. It is related to two stacked zincblende structures along c direction. The metal atom (Cu, In) has four Se atoms as the nearest neighbors and Se atom is tetrahedral bonded with two Cu and two In atoms. The chalcopyrite structure can be illustrated as two interpenetrating anion and cation sublattices with face-centered cubic structure. The partial substitution of indium (In) atom with gallium (Ga) atom in the CuInSe_2 structure leads to the change on the lattice constants (a and c) of the material. Because Ga atom has a smaller atomic radius compared to In atom, the partial replacement of In by Ga results in a reduction of bond lengths and thus in the decrease of the lattice constant. The decrease of bond length reduces the photon wavelength absorption and thus the band gap increases. The theoretical variation of lattice parameters with Ga alloying in CIS is shown in Table 2.1. The crystal lattice parameter is calculated from Vegard's law which is an approximation of an alloy and the concentrations of the elements [29].

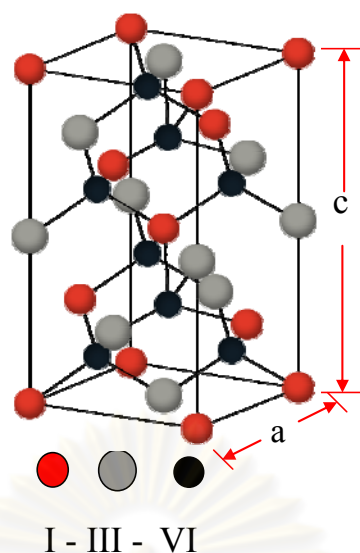


Figure 2.9 The chalcopyrite structure of $\text{Cu}(\text{In,Ga})\text{Se}_2$ where red atoms are Cu, gray atom are In or Ga and black atom are Se.

Table 2.2 Theoretical variation of the lattice parameters a and c in chalcopyrite alloys calculated from Vegard's law for $\text{Cu}(\text{In}_{1-x}\text{Ga}_x)\text{Se}_2$.

Gallium concentration $x = [\text{Ga}]/([\text{Ga}]+[\text{In}])$	Lattice parameter a (Å)	Lattice parameter c (Å)
0	5.781	11.642
0.05	5.772	11.610
0.10	5.763	11.578
0.15	5.753	11.546
0.20	5.744	11.514
0.25	5.735	11.483
0.30	5.726	11.451
0.35	5.716	11.419
0.40	5.707	11.387
0.45	5.698	11.355

2.4 Formation of CuInSe_2 , CuGaSe_2 and Cu(In,Ga)Se_2 compounds

2.4.1 Phase diagram of Cu-In-Se system

The formation of CuInSe_2 compound can be described by a phase diagram along Cu_2Se - In_2Se_3 pseudobinary phases as shown in Fig. 2.10 [30]. There are a number of different phases in the phase diagram which depend on the Cu concentration and the substrate temperature. The α -CIS phase has Cu concentration between 24.0-24.5 atomic percent or slightly Cu deficient as seen in the red area. Because of the glass substrate used in the fabrication, then the maximum substrate temperature is limited (below 600°C). Thus, there is a narrow region to obtain α -CIS. An effective *in situ* monitoring is then required for an end point detection (EPD) that will be explained in the next section. However, the stoichiometric CIS still has the mixture of two phases consisting the α -CIS and Cu_2Se . The quantity of Cu_2Se will increase with the Cu concentration (Cu-rich). The liquid Cu_xSe phase is very important in the growth process because it segregates on the CIGS surface and enhances the formation of large-grained CIGS thin film that is suitable for the solar cell applications. On the other hand, the Cu deficient regions (Cu-poor), there are two interesting phases consisting of β -CIS and γ -CIS. β -CIS is known as ordered vacancy compound (OVC) or ordered defect compound (ODC) while γ -CIS is a layered structure.

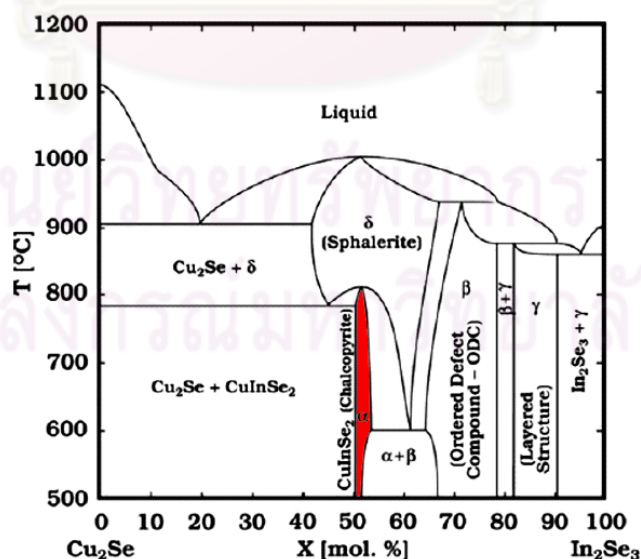


Figure 2.10 Phase diagram along the Cu_2Se and In_2Se_3 for the formation of CuInSe_2 compound.

2.4.2 Phase diagram of Cu-Ga-Se system

The formation of CuGaSe_2 compound can be explained by a phase diagram along the $\text{Cu}_2\text{Se}-\text{Ga}_2\text{Se}_3$ pseudobinary section as shown in Fig. 2.11 [31]. The study of Cu-Ga-Se system is rare compared to the study of Cu-In-Se system and has many contradictions due to the disagreement of experimental results. The chalcopyrite CuGaSe_2 phase is wider than the $\alpha\text{-CuInSe}_2$ when comparing their phase diagrams. It starts from stoichiometric ratio with Cu-concentration 25 at.% to Cu-poor with Cu-concentration of 20.7 at.%. In the Cu-poor region, there is a mixture of only two phases, consisting of CuGaSe_2 and the defect zincblende (sphalerite) Ga_2Se_3 with less complexity than the Cu-In-Se system. In the Cu-rich region, there are two phases same as in the Cu-In-Se system. Because the melting point of CuGaSe_2 is higher than CuInSe_2 ($T_{m,\text{CGS}} = 1080^\circ\text{C}$ and $T_{m,\text{CIS}} = 980^\circ\text{C}$), it is more difficult to grow high quality CGS thin films at the same substrate temperature. The grain size of the CGS thin film is smaller than that of the CIS thin film. The CGS films have been fabricated for the wide band gap solar cells and used as the top cell in tandem cells.

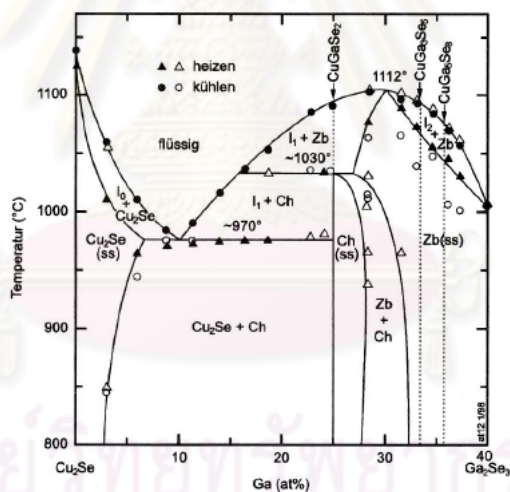


Figure 2.11 Phase diagram of Cu_2Se and Ga_2Se_3 for a formation of CGS compound.

2.4.3 Phase diagram of Cu-In-Ga-Se system

The formation of $\text{Cu}(\text{In,Ga})\text{Se}_2$ compound is more complicated than CIS and CGS compounds. It can be described by considering the isothermal quasi-ternary $\text{Cu}_2\text{Se}-\text{In}_2\text{Se}_3-\text{Ga}_2\text{Se}_3$ phase diagram as shown in Fig. 2.12 [32]. It has two narrow interesting regions in the triangle. First region, the chalcopyrite phase (Ch), used to fabricate the absorber, has a wider range when incorporated with Ga. Second region, the mixture of three phases (β -phase, γ -phase and δ -phase) that cannot be seen in Cu-In-Se and Cu-Ga-Se systems.

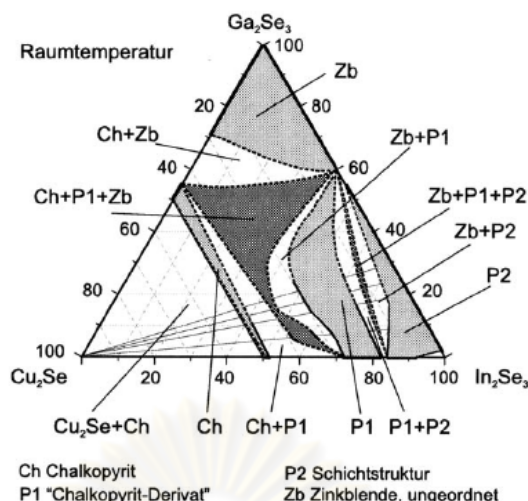


Figure 2.12 Isothermal quasi-ternary $\text{Cu}_2\text{Se}-\text{In}_2\text{Se}_3-\text{Ga}_2\text{Se}_3$ phase diagram where Ch is the α -phase, P1 is the β -phase, P2 is the γ -phase or layered structure and Zb is the δ -phase.

2.5 Defect in $\text{Cu}(\text{In},\text{Ga})\text{Se}_2$ compound

The electrical conductivity of $\text{Cu}(\text{In},\text{Ga})\text{Se}_2$ directly relates to the defects in crystal structure that have a high degree of compensation between defect donors and acceptors. However, both types of defect can be constituted by varying the ratio $\text{Cu}/(\text{In}+\text{Ga})$ used in the fabrication and by the pressure of Se used during growth or annealing. The defect formation energies of various point defects in CuInSe_2 calculated from *Ab initio* are illustrated in Table 2.3 [33]. The majority defect pair in CuInSe_2 under the condition of excess In_2Se_3 with an excess or deficiency of selenium (ΔS) is shown in Table 2.4. The V_{Cu} and $(2V_{\text{Cu}}+\text{In}_{\text{Cu}})$ neutral defect complexes (NDCs) have low formation energies and seem to be dominated in $\text{Cu}(\text{In},\text{Ga})\text{Se}_2$ films. In order to obtain the low receptivity of p-type CuInSe_2 film, the ratio $\text{Cu}/(\text{In}+\text{Ga})$ and Se flux must be precisely controlled in the fabrication processes.

Table 2.3 Formation energies of intrinsic defects in CuInSe_2 .

Types of defect		Formation energy (eV)
Vacancies	V_{Se}	2.4
	V_{Cu}	2.6
	V_{In}	2.8
Interstitials	Cu_i	4.4
	In_i	9.1
	Se_i	22.4
Antisites	In_{Cu}	1.4
	Cu_{In}	1.5
	In_{Se}	5.0
	Se_{In}	5.5
	Se_{Cu}	7.5
	Cu_{Se}	7.5

Table 2.4 Majority defect pair in CuInSe_2 under the condition of an excess of In_2Se_3 with an excess or deficiency of selenium (ΔS).

Majority defect pair		Stoichiometry deviation
Acceptor	Donor	ΔS
V_{Cu}	In_{Cu}	<0
V_{Cu}	V_{Se}	<0
V_{Cu}	In_i	>0
Se_i	In_{Se}	>0
Se_i	In_i	>0

CHAPTER III

EXPERIMENTAL PROCEDURES

This chapter, I will first describe the experimental procedures in the fabrication of the CIGS thin film. In the fabrication of the CIGS absorber, there are several well known processes, e.g. single-stage, two-stage, three-stage as well as Ga-grading growth processes. The growth profiles of the processes will be described. Then, the importance of *in situ* monitoring will be discussed why it can be used to control the growth process and obtain the end point detection (EPD). Finally, the procedures in the fabrication of the CIGS solar cells will be described in details and the characterization tools used in this work will be explained.

3.1 Fabrication processes of CIGS thin films

3.1.1 Single-stage process

A single-stage process is perhaps the simplest method to grow the $\text{Cu}(\text{In,Ga})\text{Se}_2$ absorber thin films. Cu, In, Ga and Se sources are co-evaporated at a constant rate with Cu-poor concentration about 10% from stoichiometric ratio for obtaining chalcopyrite phase. The substrate temperature is kept constant during the growth process in the range of 500-580°C. The CIGS films fabricated with this process show small columnar grains. The solar cell efficiency of this absorber is relatively low when compared with the other growth processes.

3.1.2 Two-stage process

The two-stage process or also known as bilayer process was first proposed by Mickelsen and Chen in 1980 [34, 35]. The process starts with the deposition of Cu-rich precursor at the substrate temperature of 400-450°C and is followed by the deposition of Cu-poor composition at 500-550°C until the overall composition is slightly Cu deficient (α -CIGS). Klenk *et al.* and Tuttle *et al.* explained that the Cu_xSe in the first stage is liquid phase that assisted in grain growth formation [36]. Therefore the CIGS film fabricated by the two-stage process shows large columnar grains and rough surface. Practically, this process is employed in the solar cell industry.

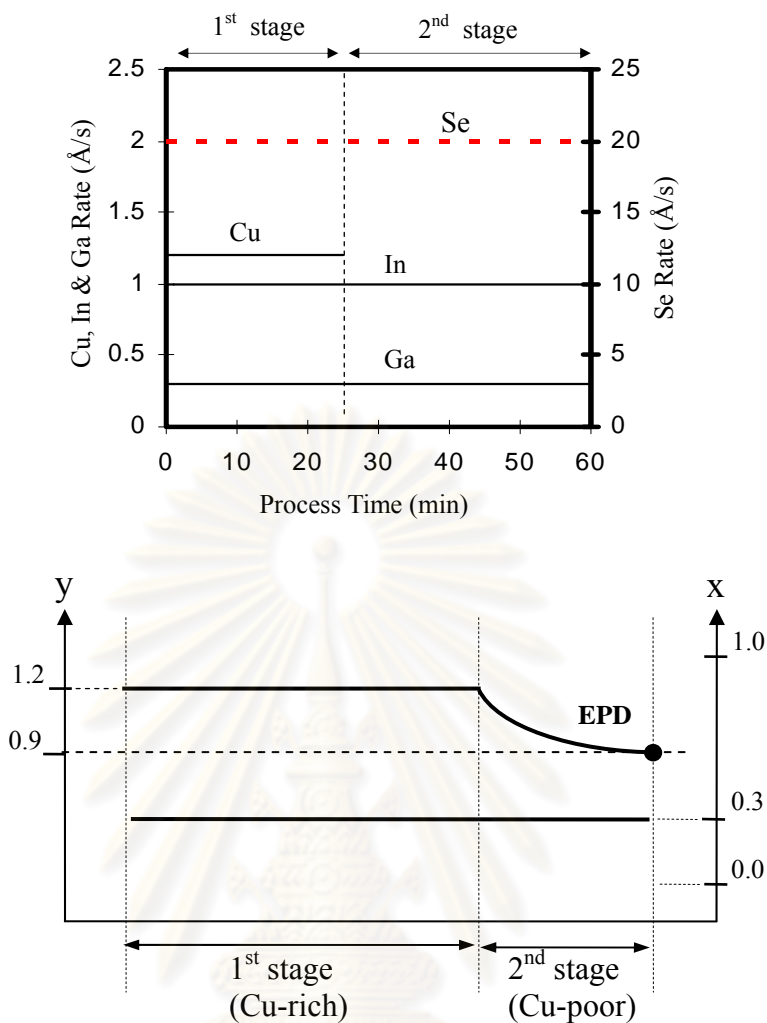


Figure 3.1 Deposition rate of any elements and the evolution of $[Cu]/([In]+[Ga])$ ratio (y) and $[Ga]/([In]+[Ga])$ ratio (x) in two-stage growth process of CIGS thin films.

In our two-stage recipe, a growth profile is shown in Fig. 3.1. The process starts with the deposition of Cu, In, Ga and Se at the substrate temperature of 550°C i.e. the Cu-rich stage which has the ratio of $y = [Cu]/([In]+[Ga])$ greater than unity (relative to the stoichiometric ratio) for the formation of $Cu(In,Ga)Se_2$ and $Cu_{2-x}Se$ compounds [37]. The $Cu_{2-x}Se$ liquid phase is very important in the growth process because it segregates and covers on the CIGS surface and induces the formation of large-grained CIGS thin film that is suitable for the solar cell applications. However, the more quantity of $Cu_{2-x}Se$ in the first stage has an influence on grain growth by inducing the rough surface and the formation of crevices. Our standard two-stage process is generally set up for $y = 1.5$ for the best cell. In the second stage, the

deposition of In, Ga and Se converts the excess Cu_{2-x}Se entirely into $\text{Cu}(\text{In,Ga})\text{Se}_2$ (for $y < 1.0$ or a Cu-poor stage). The growth mechanism of the Cu-rich to the Cu-poor stages is described by vapour-liquid-solid (VLS) model [36]. The model describes a beneficial impact of Cu_{2-x}Se on grain growth that would be the consequence due to improved mobility of the constituent atoms in the liquid phase. The y ratio is about 0.9, slightly less than stoichiometric ratio, in order to obtain the chalcopyrite $\text{Cu}(\text{In,Ga})\text{Se}_2$ phase at the EPD. The duration of the growth process is about 90 minutes which typically yields the thickness of the CIGS of about 1.5 μm .

3.1.3 Three-stage process

The high efficiency CIGS solar cells mostly use the three-stage process in the fabrication of $\text{Cu}(\text{In,Ga})\text{Se}_2$ thin film. The growth profile is shown in Fig. 3.2. The process starts with the deposition of In, Ga and Se at a substrate temperature (T_{sub}) of 340°C in the first stage for a formation of $(\text{In,Ga})_2\text{Se}_3$ layer. In the second stage, only Cu and Se vapors are allowed at T_{sub} of 550°C at which there is a transformation from $(\text{In,Ga})_2\text{Se}_3$ layer via $\gamma\text{-CI(G)S}$ and $\beta\text{-CI(G)S}$ to $\alpha\text{-CI(G)S}$. The formation of polycrystalline $\text{Cu}(\text{In,Ga})\text{Se}_2$ occurs until the composition of film is slightly Cu-rich ($y > 1$) at the end of the second stage. Our standard three-stage process uses $y = 1.2$. During the last stage, the deposition of In, Ga and Se at T_{sub} of 550°C converts excess Cu_xSe entirely into Cu-poor at EPD ($y = 0.9$). The duration of the growth process is about 90-120 minutes which typically yields the thickness of CIGS of about 1.25-1.5 μm .

CIGS films prepared with the three-stage process show a large grain and smooth surface compared with the single-stage and the two-stage processes. The grain sizes increase throughout the second stage was observed by Nishiwaki *et al.* [38]. However, Gabor *et al.* reported that the large grain sizes constitute in the third stage [39]. They observed the small grain sizes towards the end of the second stage before the film reached stoichiometric composition [40]. Scheer *et al.* reported the development of surface roughness during the three-stage process observed with spectroscopic light scattering [41]. Their results suggest an optimum of a Cu excess of about 10% or $y = 1.1$ at the end of the second stage in order to obtain a minimum surface roughness.

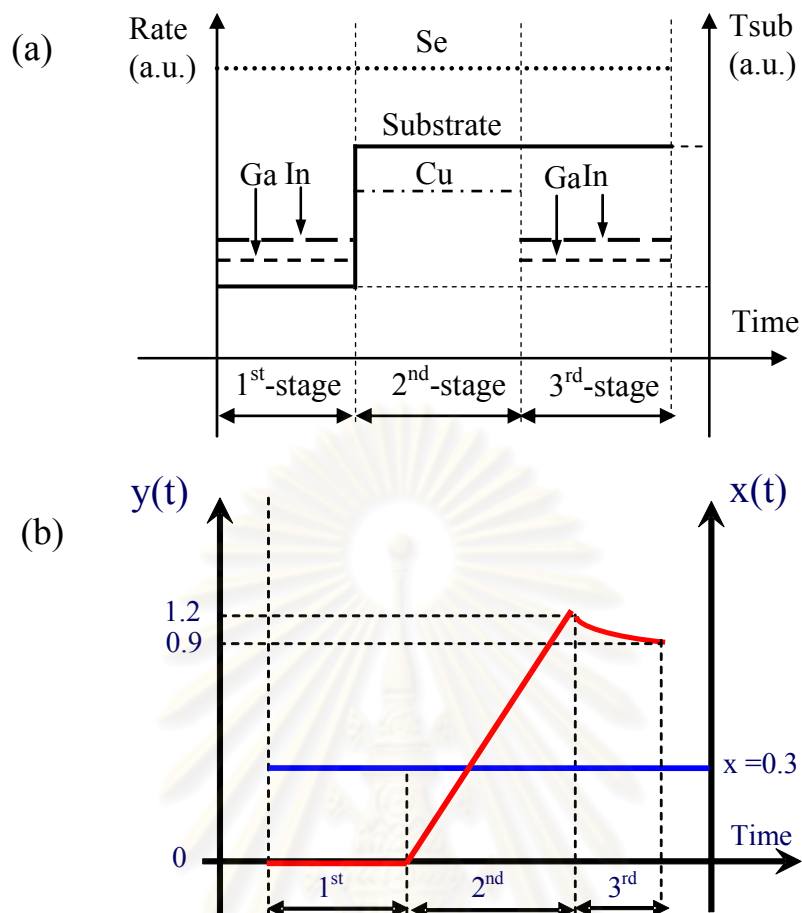


Figure 3.2 (a) Deposition rate of any elements and the substrate temperature. (b) Evolution of Cu-content (y) and Ga-content (x) in three-stage growth process of CIGS thin films.

The modification of the three-stage process known as CUPRO (Cu-poor, rich, off) was proposed by J. Kessler and co-workers [42]. The process starts with deposition of Cu-poor precursor instead of deposition $(\text{In,Ga})_2\text{Se}_3$ layer in the usual three-stage process. Then the process is followed with the deposition of Cu rich and Cu poor stages again as in the three-stage process. The CIGS film fabricated with CUPRO process shows larger columnar grains and rough surface than the single-stage process. The phase transformation of CIGS film in CUPRO process is less than in three-stage process. In addition, the gradient of Cu during the second stage might be the driving force for the grain growth and the formation of crevices depending on the amount of Cu excess at the end of the second stage.

3.1.4 Band gap grading

According to the material property, the band gap of CIGS thin film can be adjusted by varying the ratio of $[\text{Ga}]/([\text{In}]+[\text{Ga}])$. A method that helps to increase the solar cell efficiency in the CIGS film is known as band gap grading [43]. The variation of the band gap energy towards the back contact causes the electric field, namely back-surface field (BSF) [44]. It assists in sweeping electrons in the quasi-neutral region of absorbers across the junction, resulting in the increase of the minority carrier's life time and diffusion length as well as reduction of the recombination [45]. Thus the solar cell efficiency improves by the increase of probability for carrier collection. The variation of band gap in CIGS thin film can be obtained by varying the $[\text{Ga}]/([\text{In}]+[\text{Ga}])$ ratio at different depths in the CIGS film. The change of Ga ratio affects the increasing of conduction band minimum while the valence band maximum is nearly unaffected as seen in Fig. 3.3. However, there is a trade-off between the increase of carrier collection and the loss of created electron-hole pair from low-energy photons due to the increase in band gap. The band gap grading is beneficial in reducing the thickness of the absorber layer. It has been shown from theoretical and simulation works elsewhere that the band gap grading can increase the solar cell efficiency and agree with experimental works [46, 47].

In our experiment, the band gap grading can be done by modifying the two-stage growth process. In our typical CIGS film, the $[\text{Ga}]/([\text{In}]+[\text{Ga}])$ ratio (x) is always a constant ($x = 0.3$) throughout the process as seen in Fig. 3.4. For a Ga-graded profile, the structure begins with a Cu-rich CuGaSe_2 film (25-30% of the process time) and the Cu-rich CuInSe_2 is subsequently deposited onto the CuGaSe_2 . The $[\text{Cu}]/([\text{In}]+[\text{Ga}])$ ratio is more or less the same as the CIGS film ($y = 1.2$). In the 2nd stage, In and Se vapor, are maintained to convert Cu_xSe in Cu-rich to Cu-poor $\text{CuIn}(\text{Ga})\text{Se}_2$, ended at EPD. The inter-diffusion of Ga and In between the interface layer can create the variation of the band gap energy towards the back contact due to the variation of Ga-content [46]. The key physical parameters consist of a process time and a substrate temperature which affect the diffusion of In and Ga atoms. Some experiment reported the effect of Na on diffusion of Ga and In in CIGS thin film. The presence of Na reduces the inter-diffusion of In and Ga that can be observed in the separated peaks of X-ray diffraction.

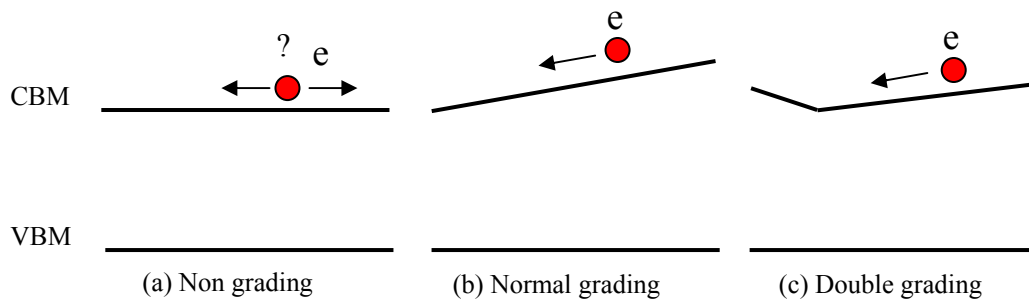


Figure 3.3 Schematic diagram of band gap grading profile (a) non-grading, (b) normal-grading and (c) double grading.

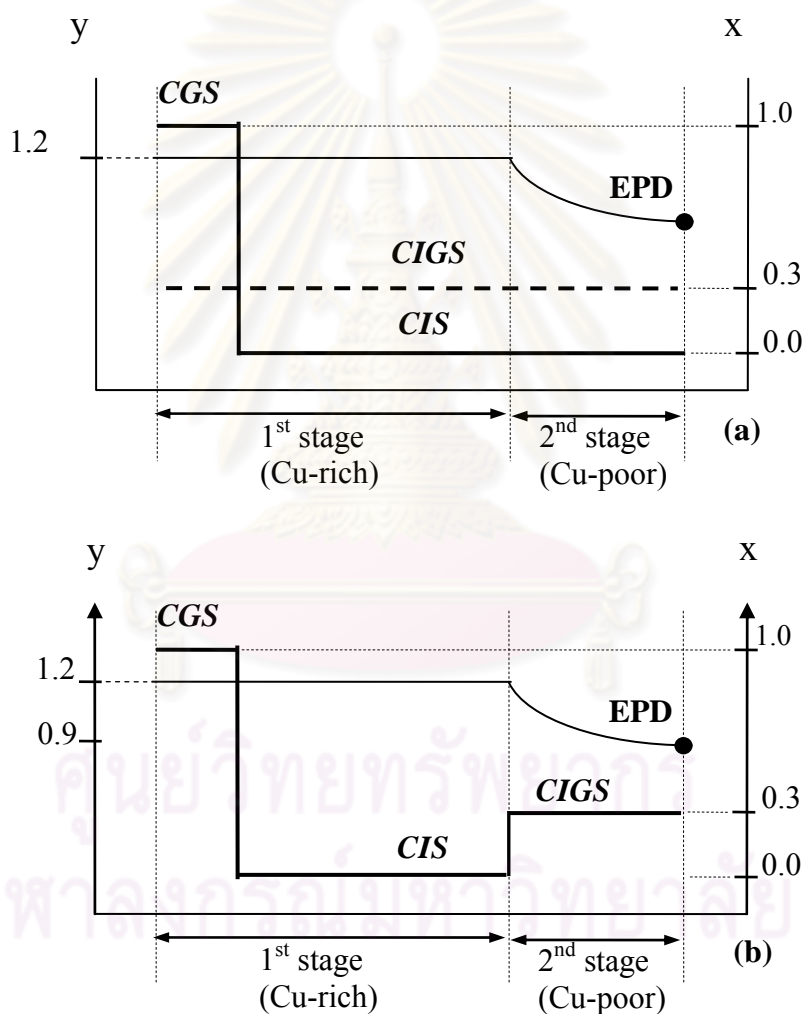


Figure 3.4 Two-stage growth process for the CIGS film (dash line) and normal Ga-graded CIGS film (solid line) (a) and double grading (b).

The second method of fabricating Ga-graded CIGS film is known as the double Ga-graded profile. The rise of band gap in the front layer can enhance the

built-in electric field and thus expect to gain V_{oc} . In our recipe, the profile begins with $x = 1.0$ about 25% of the process time and subsequently deposits with $x = 0$ about 50% of the process time. Finally, In, Ga and Se vapor with $x = 0.35$ are supplied until the end of the process as shown in Fig. 3.4. The process time is within 80 minutes for 0.7 μm thick of Ga-graded CIGS film.

3.2 *in situ* monitoring and end point detection

In the fabrication processes such as the two-stage and the three-stage, CIGS thin film has a phase transformation from Cu-rich to Cu-poor film during the process. It is very difficult to stop at chalcopyrite phase because of the narrow region in the phase diagram. Therefore, various *in situ* monitoring signals e.g. substrate heating power and pyrometer are used to control the growth process and end point detection (EPD) as shown in Fig. 3.5. By observing the variation of the controlled signals, the desired final composition of the CIGS film can be obtained. The principle of film monitoring is based on the different emissivity of Cu_xSe , stoichiometric and Cu-poor CIGS compounds, or the change of $[\text{Cu}]/([\text{In}]+[\text{Ga}])$ ratio [49].

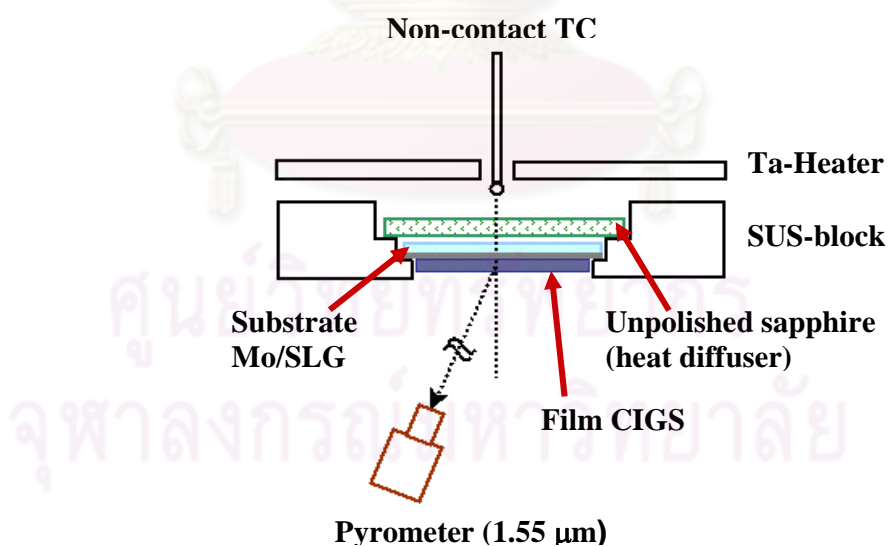


Figure 3.5 The *in situ* monitoring consisting of pyrometer signal and substrate heating output power during the CIGS growth.

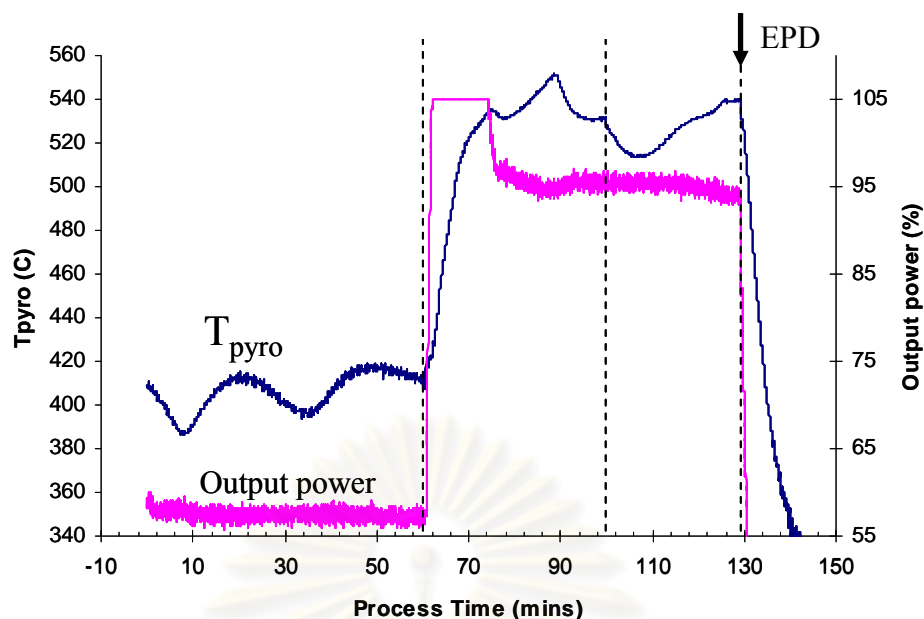


Figure 3.6 The in situ monitoring signals e.g. substrate heating output power and pyrometer signal from the three-stage growth process.

The monitoring signal is sensitive to the phase change. Due to the segregation of Cu_{2-x}Se on the CIGS surface or metallic surface, the Cu-rich CIGS film has higher emissivity than stoichiometric and Cu-poor CIGS film [50, 51], thus the Cu-rich stage requires more substrate heating power when the substrate temperature is kept constant while the substrate heating power is regulated in constant temperature mode. The pyrometer then reads the surface temperature of Cu-rich stage lower than that of Cu-poor stage. The pyrometer measures the temperature of CIGS surface by observing irradiation of photon at wavelength $1.5 \mu\text{m}$. In addition, the pyrometer signal can tell the deposition rate of film by observing the period of oscillations. The multiple reflections based on black body radiation at the back and front surfaces of the growing film leads to the interference pattern. The damping of the oscillation amplitude occurs probably due to the increase of absorption in the band gap and also the increasing roughness of reflecting surface. For example, signals of heating output power and pyrometer signals from the three-stage process are shown in Fig. 3.6 which indicate the end of each stage as well as the EPD.

3.3 Device structure and fabrication of CIGS thin film solar cells

The device structure of the CIGS thin film solar cells consists of Ni-Al grid/ZnO/CdS/CIGS/Mo. The p-n junction is formed between Cu(In,Ga)Se_2 as the p-type semiconductor and CdS+ZnO as the n-type semiconductors. Mo and Ni-Al grid are the back and the front electrical contacts, respectively. Soda-lime glass (SLG) containing Na impurity and flexible substrate such as stainless steel (SS) sheet are used in the fabrication of CIGS film in this work. The substrate dimension used in the fabrication is $30 \times 30 \text{ mm}^2$ with 2 mm thick for SLG and 0.1 mm thick for SS. The schematic diagram of the CIGS solar cell is shown in Fig. 3.7. The device structure is the heterojunction of several metallic and semiconductor thin films. In the fabrication process, the substrates are coated with a thin Mo layer of $0.6 \text{ }\mu\text{m}$ by DC magnetron sputtering. The next step is the fabrication by molecular beam deposition (MBD) of $1.25\text{-}1.5 \text{ }\mu\text{m}$ of CIGS, and followed by chemical bath deposition (CBD) of 500 \AA of CdS. Then RF magnetron reactive sputtering of about 500 \AA of intrinsic ZnO and $5,000\text{-}8,000 \text{ \AA}$ of Al-doped ZnO is employed. The solar cell devices are completed by the evaporation of $1.5\text{-}2.0 \text{ }\mu\text{m}$ thick Ni/Al contacts through a metal shadow mask. The total area of solar cell is about 0.5 cm^2 with approximately 2.5% shading loss. The experimental details of each fabricating layers will be described in the next section.

3.3.1 Substrate preparation

The first important step in solar cell processing is the substrate cleaning because the dirt and/or contamination on the substrate surface can lead to a loss of adhesion, and

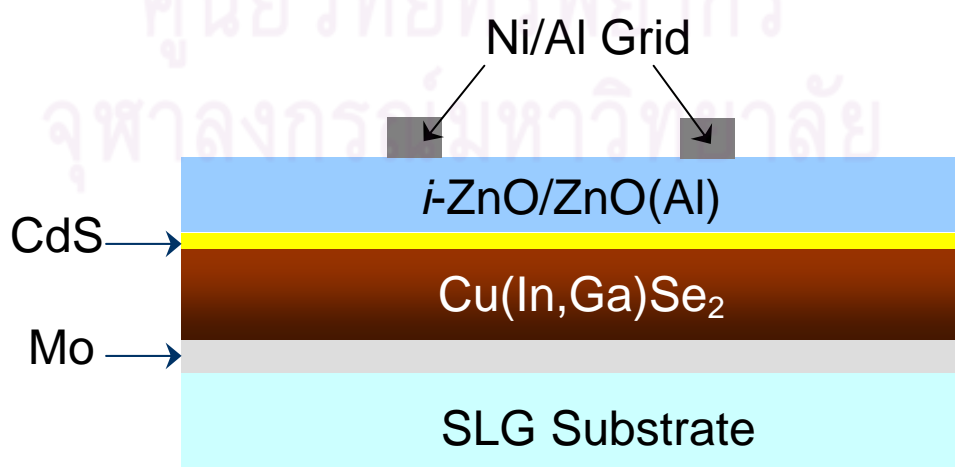


Figure 3.7 Schematic diagram of a structural Cu(In,Ga)Se_2 thin film solar cell.

unknown defects in the films, resulting the poor device performance. The cleaning process is started by soaking the SLG substrates in deionize water (18 M Ω ·cm) with dishwashing liquid for ten minutes. Then the SLG substrates are rubbed thoroughly with a wet soapy cellulose sponge and placed in the substrate holders. They are then placed in an ultrasonic bath with a mixture of dishwashing liquid and deionized water at 60°C for one hour. Then, the substrates are rinsed with deionized water and ultrasonic cleaned again in deionized water at 60°C for one hour to completely decompose the dishwashing liquid. Finally, the substrates are dried with compressed nitrogen gas and keep in a dry cabinet before loading into the next process.

To reduce or block sodium from SLG, the Al₂O₃ films are deposited on the SLG substrate before the next deposition. The Al₂O₃ film is prepared by using a 4-inch in diameter Al₂O₃ target and sputtered at the RF power of 280 W, Ar gas pressure of 2.0 x 10⁻³ mbar for 60 mins. The thickness of Al₂O₃ layer is about 800 nm. The Al₂O₃ film is an insulator with an amorphous structure similar to the glass substrate and thus does not affect the Mo growth. The surface of Al₂O₃ films is smooth with a nanoscale grain size.

3.3.2 Mo back contact

Mo is the preferred material for a back contact of CIGS solar cell in many reasons. First, the melting temperature of Mo is quite high ($T_m = 2623^\circ\text{C}$) [51], it can tolerate the high temperatures and does not degrade during Cu(In_{1-x}Ga_x)Se₂ growth. Second, Mo film does not react with Cu, In and Ga but can react with selenium to form MoSe₂ interface layer at high temperature (600°C) [52]. The presence of MoSe₂ might be the beneficial in the CIGS growth to obtain an ohmic contact. Third, Mo film has a good adhesion property to glass substrates due to the suitable thermal expansion between the Mo film and the glass substrate. Finally, Mo film forms a low-resistivity contact to CIGS and has cost effectiveness.

Mo films are deposited by DC magnetron sputtering from a 4-inch in diameter Mo target using the Univex 350 sputtering system. The main sputtering parameters are sputtering power, sputtering gas pressure and substrate temperature which affect the properties of Mo film. The higher sputtering power and the lower sputtering pressure lead to the lower resistive film and denser film. The Mo film properties relate to the kinetic energies of the sputtered atoms arriving at the film surface [53]. The adhesion of Mo film is better when increase the sputtering pressure

and heat up the substrate. The stress in Mo film depends on sputtering condition that can change from tensile to compressive stress via the increase of sputtering power.

I have used two recipes to prepare the Mo films on the SLG substrates. The first recipe is the single-layer process. The sputtering condition is optimized to obtain the low resistivity, good adhesion as well as good morphology to allow Na diffusion. The substrate-target distance is about 6 cm and the substrate holder is rotated at 3 rpm for the relaxation of the Mo films. The sputtering power is 550 W with the sputtering pressure of 6.0×10^{-3} mbar for 12 mins. The thickness is about 0.6 μm . In order to obtain the low resistive and the good adhesion films, a bilayer process was proposed to solve both problems [54]. The process starts with a thin Mo layer deposited at high sputtering pressure (1.2×10^{-2} mbar) and is subsequently followed by a thicker Mo layer deposited at lower sputtering pressure (6.0×10^{-3} mbar) at the same sputtering power (550 W). The resistivity of bi-layer Mo films is about $2 \times 10^5 \Omega\text{-cm}$. The first layer constitutes the good adhesion between Mo layer and the glass substrate and the second layer produce the low resistive film with a good adhesion. The thickness of each layer is about 200 nm and 400 nm, respectively. The quality of the Mo films affects the transport of Na through the Mo film i.e. the very dense Mo films allow less Na diffusion from SLG [55, 56, 57]. The diffusion of Na through Mo film passes via grain boundaries of molybdenum oxide phases.

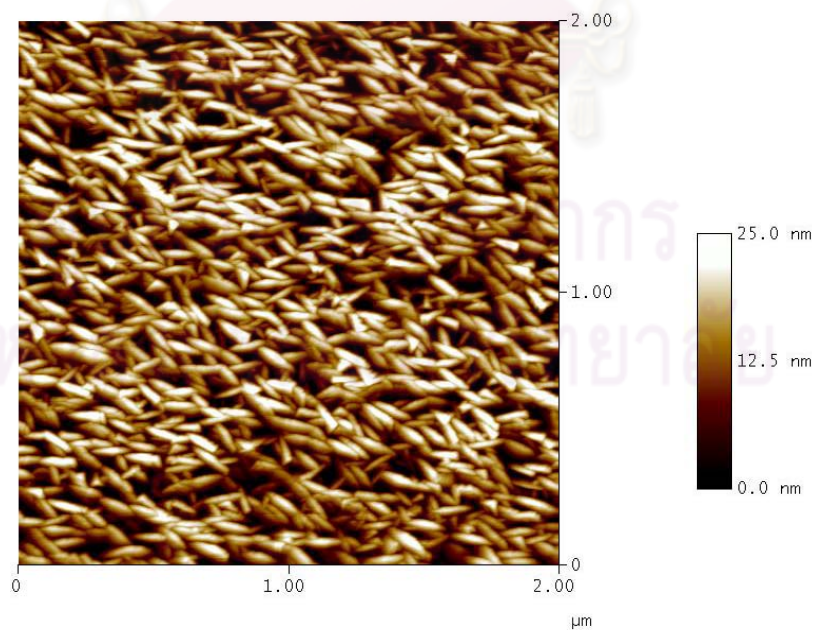


Figure 3.8 Surface morphology of Mo film on SLG substrate using the single-layer process from Atomic Force Microscopy.

Oxygen in Mo film plays an important role to the Na transportation. In general, X-ray diffraction (XRD) spectrum of Mo films usually reveals (110) preferred orientation texture. The AFM surface morphology of Mo film on SLG substrate using the single-layer process is shown in Fig. 3.8.

3.3.3 CdS buffer layer

CdS is an n-type semiconductor with band gap energy of 2.4 eV. It is used as a buffer layer in CIGS solar cell by covering the CIGS surface [58, 59]. It protects the CIGS film from sputtering of damage ZnO layer and prevents the diffusion of Zn into the CIGS layer. CdS layer is deposited by chemical bath deposition (CBD) technique with typical thickness of 50-100 nm. However, CdS has a few disadvantages such as the toxicity of Cd and the partial absorption of photon energy (> 2.4 eV). There are a few disadvantages in the preparation of CdS by CBD. First, CBD is a wet process that is not suitable in industrial productions. A dry process which must not break vacuum during the fabrication line is required for saving time and cost. The other buffer layer such as $Zn_x(S,O,OH)_y$, $(Zn,In)_xSe_y$, $In(OH)_xS_y$ as well as $ZnS(O,OH)$ are widely studied by using dry processes e.g. evaporation and sputtering methods. However, they are not good for using with CIGS solar cells when compared with CdS-CBD. Second, the toxicity of Cd is still an environmental issue, although CdS layer is used with ultra thin thickness (50-100 nm). Finally, the photon absorption in CdS layer cannot produce the photocurrent due to the short diffusion length of minority carrier (hole). Thus, the solar cell will loss the photocurrent when $h\nu > 2.4$ eV. In order to solve the problems, $ZnS(O,OH)$ -CBD is presently used for alternative buffer layer to obtain a high efficiency solar cell because the band gap of ZnS ($E_g = 3.4$ eV) material is greater than CdS which can reduce the loss of photocurrent and ZnS is a non-toxic compound [60, 61].

The CBD technique has some advantages when compared with the dry processes, e.g. CBD helps etching an oxide layer on CIGS surface before growing CdS. The CdS film can be grown epitaxially and covers the CIGS surface with a nano-size grains. The diffusion of Cd into CIGS near the surface results in the n-type conduction by the substitution of Cd into Cu site at which Cd acts as a donor atom. There is a formation of buried junction between p-type absorber and n-type surface region. In the preparation of CdS, the chemical reactions can be divided into 3 phases. First, the nucleation phase CdS with slow growth rate. Second, ion by ion growth

phase with the increase of growth rate by the reaction between Cd^{2+} and S^{2-} ions which coalesce and adhere to form a layer. Finally, the colloidal growth phase which has the large coalescence of CdS suspended in the solution [62].

In our CdS-CBD recipe, the process started with the preparation of solutions at room temperature. CdSO_4 powder is dissolved in 75 ml deionized water with a concentration of 4 mM. Then $\text{SC}(\text{NH}_2)_2$ powder is dissolved in 150 ml deionized water with a concentration of 0.06 M and ammonia solution 25 % is diluted in 52 ml deionized water with a concentration of 4 M. Cd^{2+} and S^{2-} ions are obtained from the hydrolysis reaction of CdSO_4 and $\text{SC}(\text{NH}_2)_2$. Then, $\text{SC}(\text{NH}_2)_2$ solution is filtered by 0.25 μm filter paper to capture the overhang sediments. After that, all solutions are commixed in a beaker. The CIGS samples placed in sample holder are dipped into the solution immediately. The beakers are placed in a water bath at 60°C and the level of water is kept higher than that of the solution. The deposition time is typically 15 min to obtain 50-60 nm thick of CdS film.

3.3.4 ZnO window layer

ZnO is a cost effective transparent conducting oxide (TCO) material when compared with the other TCO e.g. $\text{In}_2\text{O}_3(\text{Sn})$ (ITO) and $\text{SnO}_2(\text{F})$ (FTO). It is widely used as a front contact or window layer in CIGS based thin film solar cells [63, 64]. ZnO is a direct band gap semiconductor with würtzite structure [65]. The first layer of ZnO window is the intrinsic ZnO ($E_g = 3.3$ eV) and may be called a high resistive layer. The properties of this layer are high resistivity and good transmission which is used to prevent current leakage (shunting) and adjust the band alignment. This layer can be neglected when thick CdS is used [66]. The second layer is Al-doped ZnO (ZnO:Al) or AZO which is the actual front contact. The substitution of group III element e.g. Ga or Al atom into the Zn site can increase the carrier concentration (electron), resulting in the good conductivity. The thickness of ZnO:Al film is trade-off between transparency and conductivity. The band gap of ZnO:Al film is about 3.6-3.8 eV depending on the carrier concentration. The higher carrier concentration results in the wider band gap. The oxygen deficiency in ZnO:Al film induces the interstitial of Zn atom in the structure, resulting in the grayish color. By a little addition of O_2 to the sputtering gas, the ZnO:Al film gains the transparency but losses the conduction.

The first layer or high resistive layer is deposited by RF magnetron sputtering technique from ZnO target or ZnO:Al with reactive O_2 gas. In our recipe, ZnO with

2% by weight of Al_2O_3 target is used to sputter both layers. Leybold Univex-350 sputtering system equipped with a 4-inch magnetron sputtering gun and RF power generator is used to deposit ZnO bilayer window. The based pressure is about 2.0×10^{-6} mbar and the substrate target distant is 6 cm as well as substrate holder rotated during the deposition at 3 rpm. In order to minimize the residual gas, i.e. N_2 , O_2 , H_2O , etc., refilling with Ar gas up to an operating pressure and evacuation down to 10^{-6} mbar is performed several times. The high resistive layer is deposited by using 5% of O_2 gas mixed with Ar gas at a total sputtering pressure of 8.0×10^{-3} mbar and a sputtering power of 200 W for 10 min. The conductive layer is deposited by using pure Ar gas at sputtering pressure of 3.0×10^{-3} mbar and sputtering power 200 W for 80 min. The thickness of the first and the second layers are 50 nm and $0.75 \mu\text{m}$, respectively. The average transparent is about 90 % between the wavelength of 300 and 1200 nm. The resistivity of ZnO(Al) film is about $1.5 \times 10^{-3} \Omega\text{cm}$.

3.3.5 Ni-Al grid

CIGS solar cells usually use Ni-Al grid as a current collector. The metal grid is evaporated onto the front surface by thermal evaporation or electron beam evaporation. It reduces the thickness of the front window that gains the transmission of light to the absorber. Ni layer increases the adhesion and prevents the formation of resistive Al_2O_3 while Al layer is the metal contact. In our process, Ni and Al are sequentially evaporated through a Ni metal mask by thermal evaporation method. The evaporation system is shown in Fig. 3.9. The vacuum system has a base pressure of 4.0×10^{-6} mbar and a quartz crystal monitor is used to control the thickness. The boron nitride boat heaters are used as the evaporated sources. A 50-100 Å of Ni film is first deposited on the ZnO layer, followed by the deposition of 1.5-2.0 μm Al film and ended with deposition of 50-100 Å Ni layer.



Figure 3.9 Thermal evaporation system of Ni-Al grid.

3.3.6 Molecular beam deposition technique

Molecular beam epitaxial system (EIKO model EW-100) is used to deposit the CIGS films. The system consists of a main growth chamber and a load lock chamber as seen in Fig. 3.10. In the growth chamber, the base pressure during deposition is in the 10^{-9} Torr range. The elemental source materials consisting of Cu, In, Ga, Se and NaF are evaporated from the Knudsen cells (K-cells) and the deposition rates of any elemental sources are calibrated by the quartz crystal monitor (QCM) as shown in Fig. 3.11. Mo/SLG or Mo/Al₂O₃/SLG substrates are heated by a circular shape Ta-heater with a heat diffuser (unpolished sapphire), leading to the uniform heating distribution. The substrate temperature is controlled by a non-contact thermocouple and the substrate holder is rotated during the deposition. The deviation between the temperature of thermocouple and the temperature of substrate can be calibrated by observing desorption of oxide layer on GaAs wafer at 583°C. The change from polycrystalline to single crystal observed by reflection high-energy electron diffraction (RHEED) pattern leads to the real substrate temperature.

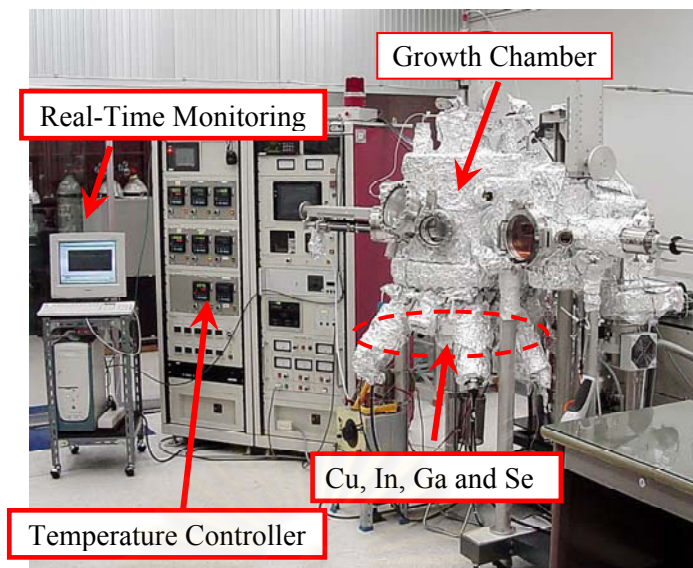


Figure 3.10 Molecular beam epitaxial system (EIKO model EW-100) containing the growth chamber, the evaporation sources, the temperature controllers and real-time monitoring system.

The substrate temperature is controlled using a constant temperature mode by regulating the output power from temperature controller. The pyrometer is used to measure the substrate temperature by detecting the thermal radiation from a sample surface. The emissivity of materials is a ratio of energy radiated by a material to energy radiated by a blackbody at the same temperature. It is the particular property and is lower than unity ($\epsilon_{\text{blackbody}} = 1$). It depends on the reflectivity and transmission properties at infrared energy. The detected radiation intensity at an infrared single wavelength was converted into the temperature by comparing with the blackbody radiation. A computer interfaced with the *in situ* signal consisting of heating output power and film temperature read by pyrometer were used to control the growth process.

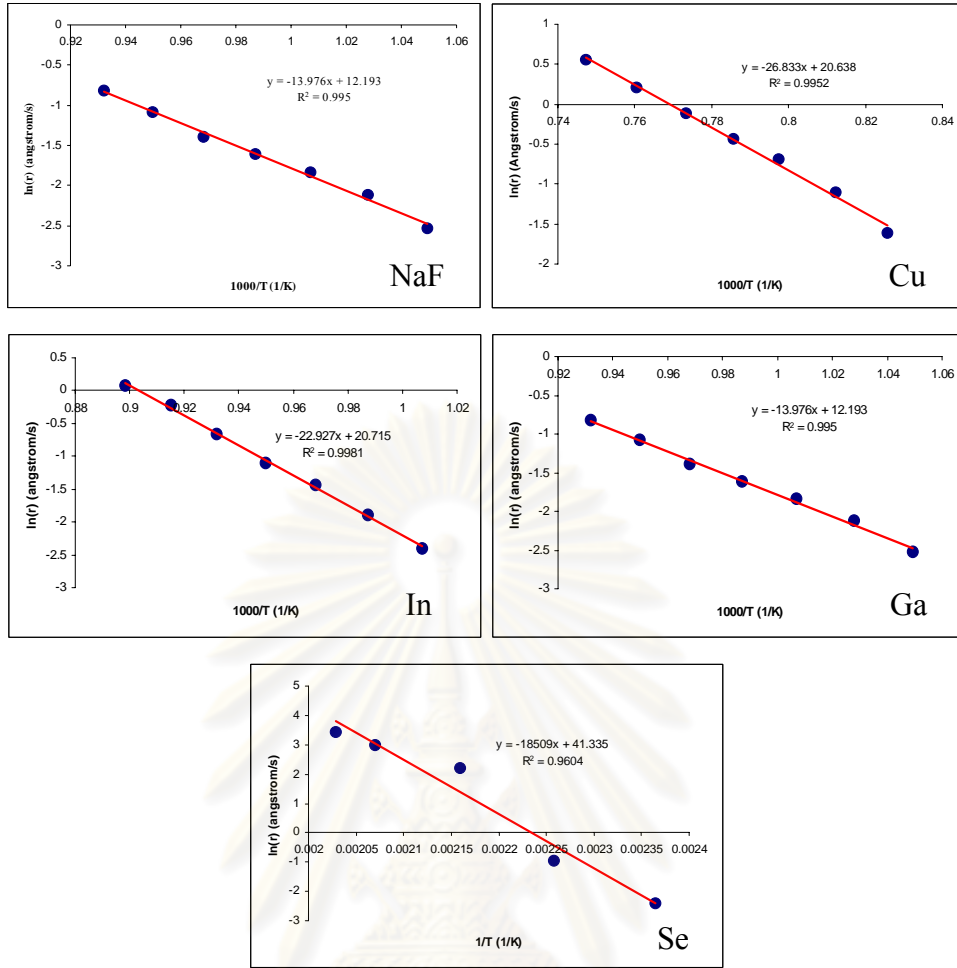


Figure 3.11 Deposition rates of elemental sources; NaF, Cu, In, Ga and Se in MBE system calibrated by QCM.

3.3.7 Calculation of the CIGS deposition process

The chemical composition of $\text{CuIn}_{1-x}\text{Ga}_x\text{Se}_2$ film in the deposition process is defined by the atomic ratios of $x = [\text{Ga}]/([\text{In}]+[\text{Ga}])$ and $y = [\text{Cu}]/([\text{In}]+[\text{Ga}])$ which relate to the properties of the CIGS film. Both x and y can be changed during the growth process by controlling the elemental fluxes used in the deposition. It is quite important to control the chemical composition. The general form of the atomic ratios can be expressed by

$$y = \frac{d_{\text{Cu}} \cdot \rho_{\text{Cu}} \cdot M_{\text{Cu}}^{-1} \cdot A \cdot N_A}{d_{\text{In}} \cdot \rho_{\text{In}} \cdot M_{\text{In}}^{-1} \cdot A \cdot N_A + d_{\text{Ga}} \cdot \rho_{\text{Ga}} \cdot M_{\text{Ga}}^{-1} \cdot A \cdot N_A}, \quad (3.1)$$

and

$$x = \frac{d_{\text{Ga}} \cdot \rho_{\text{Ga}} \cdot M_{\text{Ga}}^{-1} \cdot A \cdot N_A}{d_{\text{In}} \cdot \rho_{\text{In}} \cdot M_{\text{In}}^{-1} \cdot A \cdot N_A + d_{\text{Ga}} \cdot \rho_{\text{Ga}} \cdot M_{\text{Ga}}^{-1} \cdot A \cdot N_A}, \quad (3.2)$$

Table 3.1 Density and molecular mass of the material used in CIGS fabrication process

Material	ρ_i (g/cm ³)	M(g/mol)
Cu	8.96	63.55
In	7.31	114.82
Ga	5.91	69.72
Se	4.79	78.96
CIS	5.89	336.29
CGS	5.27	291.19

where d_i is the film thickness of metal i at time t ,

ρ_i is the density of the metal i ,

M_i is the molecular mass of the metal i ,

A is the unit area of the growing film, and N_A is Avogadro's constant.

The density and molecular mass of the materials are shown in Table 3.1.

In general, the thickness d_i is proportional to the deposition rate of elemental i (r_i) and the deposition time (t_i) when use the constant source temperature by equation

$$d_i = r_i \cdot t_i \quad (3.3)$$

Therefore the chemical composition (x and y) can be calculated from the source calibration (deposition rate) and set the source temperature relating to the desired CIGS deposition. In the two-stage process, the process starts with the deposition of Cu-rich film ($y = 1.5$) at the first stage and then the Cu flux is terminated in the second stage. Thus the y ratio continuously decreases in time during the second stage that can be written as

$$y(t) = \frac{y(t_1)}{t_1} \cdot t \quad (3.4)$$

where t_1 and $y(t_1)$ is the total time and $[\text{Cu}]/([\text{In}]+[\text{Ga}])$ ratio in the first stage, respectively. The calculation of the three-stage process is a little different from the two-stage. The first stage has y equal to zero and continuously increases to Cu-rich film in the second stage by the equation

$$y(t) = \frac{y(t_1)}{t_1} \cdot t \quad (3.5)$$

that is a linear equation in time. After the end of the second stage, the y ratio continuously decreases again corresponding to Eq. 3.4.

3.4 Characterizations

In this section, I will briefly describe the basic principle in thin film characterizations consisting of scanning electron microscope (SEM), X-ray diffraction (XRD), Auger electron spectroscopy (AES), optical transmission (%T) and optical refraction (%R), and current-voltage measurement (I-V curve).

3.4.1 Scanning electron microscope (SEM)

SEM is a structural characterization of films and surfaces that is widely used in thin film characterization. The schematic diagram of SEM is shown in Fig. 3.12. Electrons emitted from a heated tungsten or LaB₆-cathode filament and are accelerated to an anode. The electron beam is focused by two condenser lenses into a spot size of about 10 Å in diameter. Then, a pair of scanning coils placed at the objective lens deflects the beam either linearly or in a raster manner over a surface area of the specimen. The electron beams have energy from a few keV to 50 keV, commonly used at 30 keV. The primary electrons impinge on the specimen and transfer energy to other atomic electrons and to the lattice. The interaction of primary electrons on specimen spreads and fills a teardrop-shaped volume with various electronic excitations as illustrated in Fig. 3.13. Electron and photon signals emanate from tear-shape interaction volume with various energy spectrums.

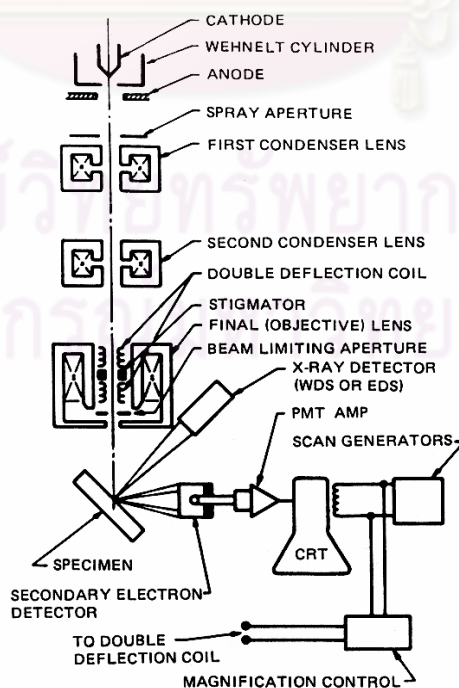


Figure 3.12 Schematic of the scanning electron microscope [24].

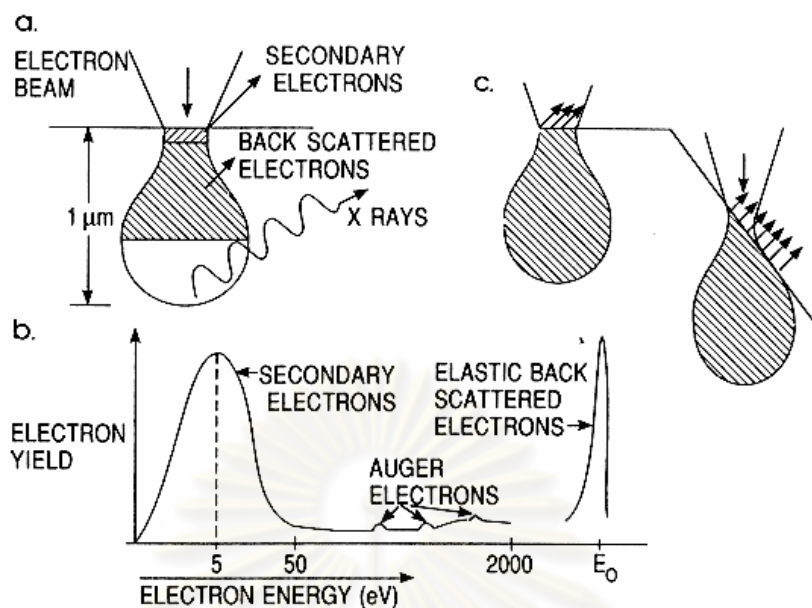


Figure 3.13 (a) Electron and photon signals emanating from tear-shaped interaction volume during electron-beam impingement on specimen surface. (b) Energy spectrum of electrons emitted from specimen surface. (c) Effect of surface topography on electron emission [24].

Effect of surface topography on electron emission can be imaged with an appropriate detector. SEM has three imaging modes based on the detector.

1. Secondary electrons are the common imaging mode. The secondary electron has the lowest energy portion of the emitted energy distribution. The signal is captured by a detector consisting of a scintillator/photomultiplier combination.
2. Backscattered electron imaging mode, backscattered electrons are the high energy electron which are elastic scattering and has the same energy as the primary electrons. The probability of back scattering increases with the atomic number Z of the sample material.
3. X-ray mode, the number of x-ray emitted, the concentration of atoms in the specimen can be determined. This technique is known as X-ray energy dispersive analysis (EDX).

3.4.2 X-ray diffraction (XRD)

XRD technique is used to determine the crystal structure of bulk solid such as lattice constants and crystallography, identification of unknown materials, orientation of single crystals and preferred orientation of poly-crystals, defects, stresses, etc. XRD is

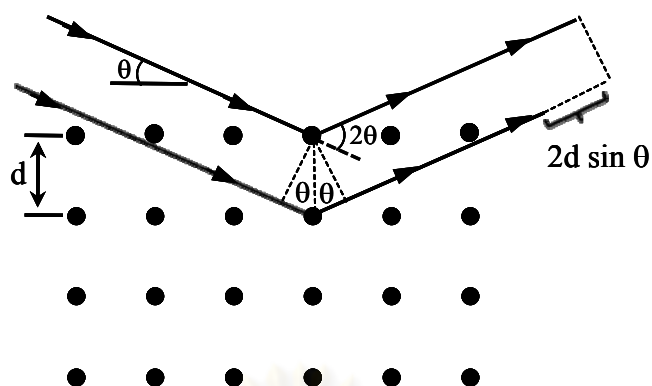


Figure 3.14 X-ray diffraction in crystal lattice satisfied the Bragg's condition.

a non-destructive technique which measures the scattered intensity of x-ray beam colliding a sample. The maximum intensity of x-ray scattered from a crystal lattice relates to the Bragg's conditions. First, the angle of incident beam is equal to the angle of scattering beam and the path length difference is equal to an integral number of wavelengths as seen in Fig. 3.14. It can be expressed the relation by

$$2d \sin \theta = n\lambda \quad (3.1)$$

where d is the interplanar spacing, θ is the Bragg's angle and λ is the wavelength of x-ray. Bruker model D8 x-ray diffractometer equipped with Cu K_{α} radiation source at a wavelength of 1.5406 Å is used to characterize the samples. The d spacing of Cu(In,Ga)Se₂ tetragonal system relates to the lattice parameters by

$$\frac{1}{d^2} = \frac{h^2 + k^2}{a^2} + \frac{l^2}{c^2}, \quad (3.2)$$

where h , k , l are the Miller indices of diffraction plane and a , c are the lattice constants. $\lambda = 1.5406$ Å for Cu $K_{\alpha 1}$ radiation.

3.4.3 Chemical characterization of surface and film

For the chemical characterization e.g. SEM/EDX, AES, XPS and SIMS, all of them can be used to identify the chemical composition on the surface, and depth distributions. These techniques are based on the measuring of atoms through the electron transition. AES, XPS and SIMS analyze the surface by detecting electrons and ions emitted from surface layers less than 15 Å deep. The depth profile can be probed by using sputter etching of the film and analyzing the newly exposed surface.

For the CIGS films in the work, Auger electron spectroscopy (AES) was used to identify elemental compositions by measuring the energies of Auger electrons. A schematic diagram of AES is illustrated in Fig. 3.15 which consists of electron gun, electron detector and Ar^+ -gun. The electron beam from the gun bombards the film surface and then the detector measures the energy of Auger electrons released from the interactions. In addition, Ar^+ ions are used to etch the film surface in depth profile mode. By considering the electronic structure of an unexcited atom as seen in Fig. 3.16, electrons are occupied in the states that can be separated into K, L, M, etc. shells corresponding to 1s, 2s, 2p, 3s, etc. configuration. An Auger process starts with a removal of an inner shell atomic electron to form a vacancy by commonly bombarding with an electron beam. Then, the inner shell vacancy or electron vacancy is filled by a second atomic electron from higher shell. Therefore, the photon energy must be simultaneously released and then strike a third electron or Auger electron emitted from atom.

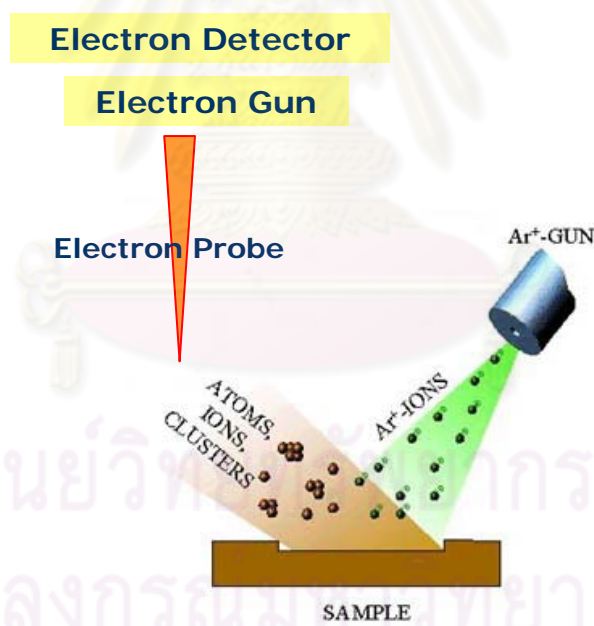


Figure 3.15 Schematic diagrams of AES in depth profile mode consisting Ar^+ -gun, electron gun and electron detector.

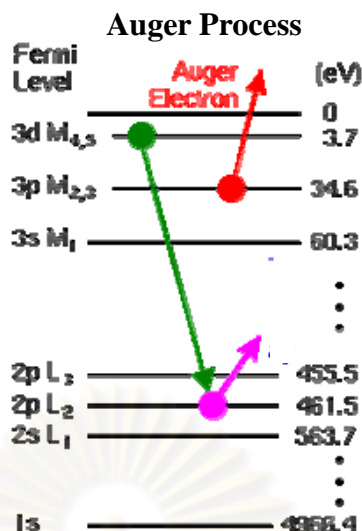


Figure 3.16 Electron configurations of an atom and the Auger electron process.

The kinetic energy of the Auger electron is a characteristic property of any element due to the difference of electron configuration. The energy of Auger electron can be expressed by

$$E_{\text{Auger}} = E_{L_2} - E_{M_4} - E_{M_3} \quad (3.3)$$

3.4.4 Optical transmission and Optical reflection

Optical property of semiconducting films can be determined by the transmission or the reflection measurements. Perkin Elmer model Lambda 900 double-beam spectrometer in the wavelength 200-2600 nm is used to measure the CIGS thin films. The spectrometer consists of a halogen lamp and a deuterium lamp covering a near infrared (NIR), visible (VIS) and ultraviolet (UV) ranges. The near infrared and visible ranges come from the halogen lamp while the UV is from the deuterium lamp. The transmission is defined by the ratio of the intensity of the transmitted radiation to that of the incident radiation. It is related to the absorption coefficient (α) or absorbance and the film thickness (d) given by

$$I = I_0 e^{-\alpha d} \quad (3.4)$$

By considering the reflection at the film surface, the transmitted radiation are reduced to $(1-R)I_0$, where R is the reflection. Therefore, the radiation reflecting from the back surface is $(1-R)I_0 e^{-\alpha d}$. By considering the multiple reflections, the total transmitted radiation can be given by

$$T = \frac{I}{I_0} = \frac{(1-R)^2 e^{-\alpha d}}{1-R^2 e^{-2\alpha d}} \quad (3.5)$$

and

$$e^{-\alpha d} = \frac{\sqrt{(1-R)^4 + 4T^2 R^2} - (1-R)^2}{2TR^2} \quad (3.6)$$

Optical transmission of a semiconducting film at the long wavelength is related to the free carrier absorption that corresponds to the doping and defects. In addition, the number of oscillation fringes and interference intensity are related to the thickness and the surface roughness, respectively. The direct band gap energy can be determined from [67, 68]

$$\alpha = \frac{A}{hv} (hv - E_g)^{1/2} . \quad (3.7)$$

The quality of the CIGS films can be determined by considering the %R and %T below the band gap energy. The high amplitudes of optical transmission and optical reflection interference fringes refer to low free carrier absorption, i.e. low defects in the CIGS films. The sharp cut off at the band gap indicates the high quality energy level in the band diagram. The optical transmission and optical reflection of the CIGS film is shown in Fig. 3.17.

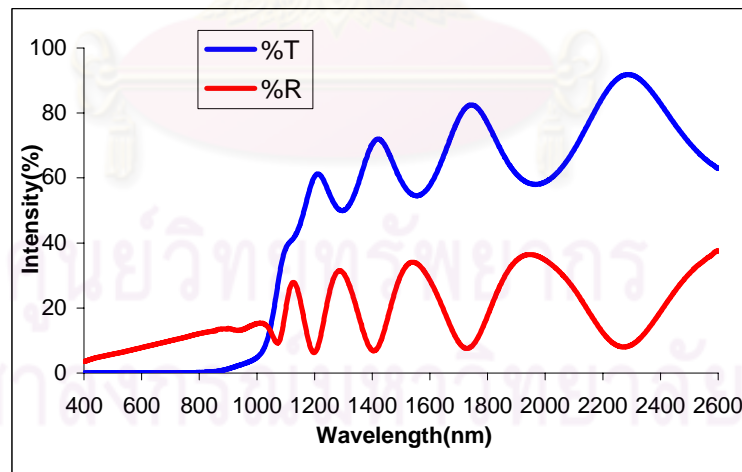


Figure 3.17 Optical transmittance and optical reflectance of the CIGS thin film grown by three-stage process.

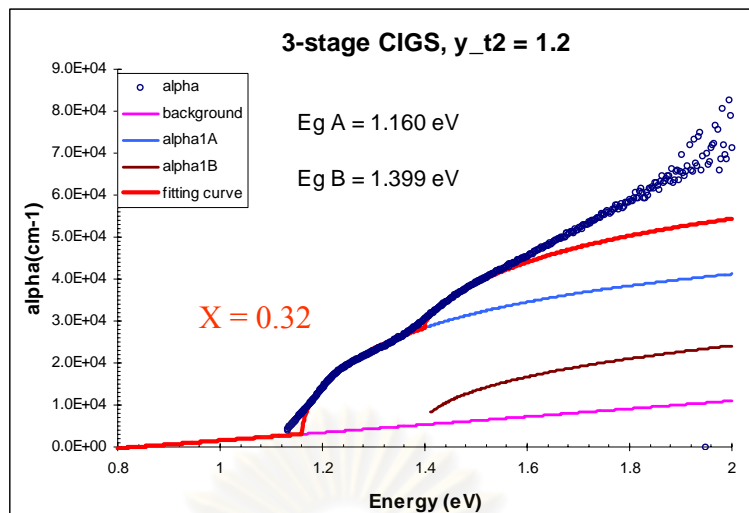


Figure 3.18 Absorption coefficient of the CIGS film calculated from %T, %R and thickness of the CIGS film.

The absorption coefficient of the film calculated from Eq. 3.6 is shown in Fig. 3.18. Note that, the energy gap of the film can be determined by Eq. 3.7.

3.4.5 I-V measurement

The I-V characteristics of the CIGS solar cells are measured using a system that consists of a single 300W-ELH lamp with a DC power supply and a voltage source/current measurement unit (Keithley model 237). The solar cell performance is measured under the standard test condition (AM 1.5 at 25°C). The light intensity is kept at 100 W/cm². The measurement unit is interfaced with a PC via IEEE-488 card. Agilent VEE program is used for the data processing. The solar cell parameters such as open-circuit voltage (V_{oc}), short-circuit current density (J_{sc}), fill factor (FF), series resistance (R_s), shunt resistance (R_{sh}) and efficiency can be determined from the I-V curve.

จุฬาลงกรณ์มหาวิทยาลัย

CHAPTER IV

RESULTS AND DISCUSSIONS

In this chapter, I will discuss and compare the growth of the CIGS thin films with and without Na diffusion into the films in order to study the influence of Na from SLG. The Al_2O_3 thin films, due to the high packing coefficient and high density, are chosen to block and/or reduce the diffusion of Na from the SLG substrate. Then, the comparative study of internal Na from the SLG and the external Na from NaF compound will be investigated leading to the possibility to use NaF as a Na source. After that, the ways to incorporate NaF during the growth profile will be explored to the best approach of using NaF to enhance the solar cell efficiency. Finally, the evolution of the CIGS thin films with NaF precursor will be described during the growth process.

4.1 Effects of internal sodium diffusion and external sodium fluoride precursor in $\text{Cu}(\text{In,Ga})\text{Se}_2$ thin film solar cells

In this work, I first study the influence of internal Na from the SLG substrate using an Al_2O_3 layer as a Na diffusion barrier. The Al_2O_3 barrier with approximately 1 μm thick coated on the SLG is prepared by a sputtering technique to block or reduce the Na diffusion into the CIGS films during growth at high temperature. The other purposes are the study of Sodium-Fluoride (NaF) as an external Na source precursor. NaF precursors with 20 to 200 \AA thick are evaporated on both Mo/SLG and Mo/ Al_2O_3 /SLG substrates before growing the CIGS film. However, too much of NaF precursor thickness decreases the adhesion between Mo and CIGS films. There is a limit in the use of precursor layer in order to maintain the adhesion. The standard three-stage growth process described in the previous chapter is employed in the fabrication of the CIGS films by molecular beam deposition (MBD) technique.

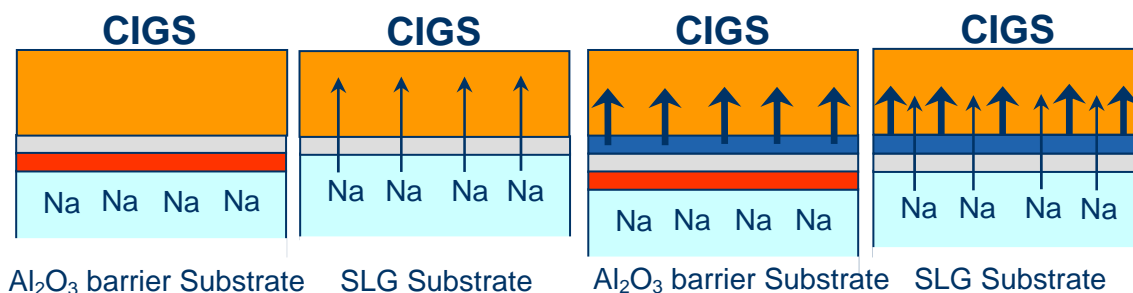


Figure 4.1 CIGS thin films fabricated on different substrate and addition of NaF precursor.

Typical deposition time of ~ 90 min for ~ 1.25 μm thick of the CIGS layers is used in this study. A series of CIGS samples grown on different Na-content substrates are shown in Fig. 4.1. The properties of the CIGS films such as crystal orientation, surface morphology, cross-section and chemical composition are investigated and compared with each other. The high Na content is intentionally chosen to verify the film properties because they are easier to determine the change of the film properties. However, the device performances of the CIGS solar cells are determined by using smaller amount of NaF and find the optimum use of NaF precursor for enhancing the p-type doping and solar cell efficiency.

4.1.1 Surface morphology and cross section

The surface morphologies of the CIGS films typically show rough surface consisting small and large grains as illustrated in Fig. 4.2. The CIGS film grown on Mo/Al₂O₃/SLG substrate shows flat round grains as shown in Fig. 4.2 (a), whereas the CIGS films grown with NaF precursor on Mo/Al₂O₃/SLG and Mo/SLG substrates reveal relatively sharp grains as shown in Fig. 4.2 (b) and (c), respectively. These results indicate that Na from the SLG substrate affects the surface morphology of the CIGS film and the NaF precursor seems to act in a similar manner to the Na from SLG substrate by inducing the sharpness of the grains. The increase of NaF precursor leads to the increase of sharp grains and the decrease of flat grains.

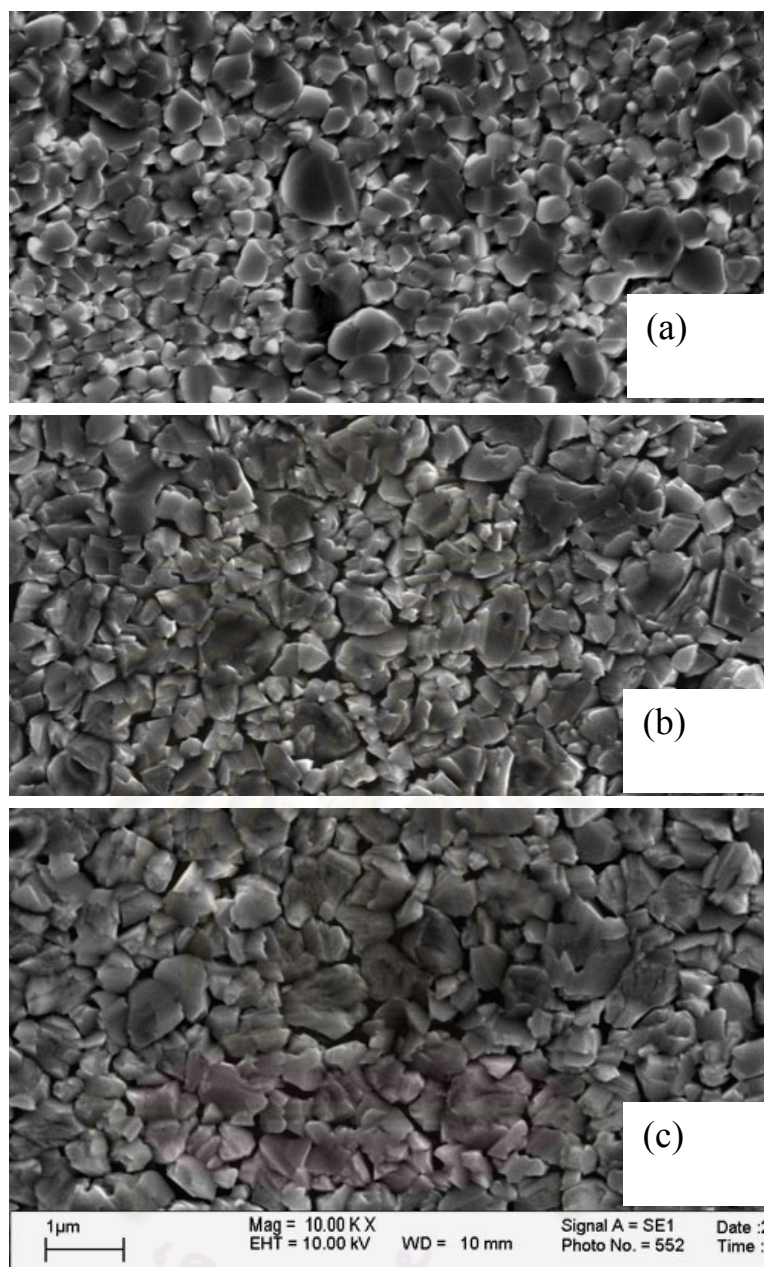


Figure 4.2 Surface morphologies of the CIGS films grown on (a) Mo/Al₂O₃/SLG (b) NaF(100Å)/Mo/Al₂O₃/SLG and (c) Mo/SLG substrates.

The cross-sectional images obtained from a secondary electron mode of SEM typically show dense columnar grains with a compact layer as seen in Fig. 4.3. The thickness of all CIGS films is about 1.25 μm corresponding to the calculation of the growth profile. By considering the grain size of the standard CIGS film grown on Mo/SLG, it shows the large grain size with a few crevices. The increase of grain size and crevices relates to the liquid phase Cu_{2-x}Se in the 2nd stage when the ratio of [Cu]/([In]+[Ga]) (y) in the film greater than 1.0 (in relation to stoichiometry). The

liquid phase Cu_{2-x}Se is very important in the growth process because it segregates on the CIGS surface and induces the formation of large grain CIGS thin film that is suitable for the solar cells. It seems to be similar in CIGS films grown on $\text{Mo}/\text{Al}_2\text{O}_3/\text{SLG}$ with and without NaF precursor. However, a thicker of NaF precursor will reduce the grain size of the CIGS film as seen from Fig. 4.3(d).

By considering the cross-sectional images from backscattered mode of SEM as seen in Fig. 4.4, it reveals an inhomogeneity of the composition on the top of CIGS film grown on $\text{Mo}/\text{Al}_2\text{O}_3/\text{SLG}$ as shown in Fig. 4.5. When measuring the thickness ratio of the ambiguous layer and the homogeneous CIGS layer, the thickness ratio is approximately 0.2. It is related to the quantity of Cu_{2-x}Se in the end of the 2nd stage ($y = 1.2$ in the growth profile) where there is the transition from stoichiometric CIGS into Cu-rich stage. Therefore, the ambiguous layer comes from the incomplete transformation of Cu_{2-x}Se into the stoichiometric $\text{Cu}(\text{In,Ga})\text{Se}_2$ in the 3rd stage. However, the CIGS film grown with (100Å) NaF precursor on $\text{Mo}/\text{Al}_2\text{O}_3/\text{SLG}$ shows a homogeneity of the stoichiometric CIGS and a larger of grain size by determining the grain boundary. This result indicates the enhancement of large grain size and the increase of uniformity by Na incorporation that resulting in the high quality film. Moreover, Na can suppress the β -phase formation during the transformation of Cu_{2-x}Se into CIGS compounds. Our results agree with Karin Granath *et al.* work. Na from internal diffusion and external NaF precursor has the same property to enhance surface and grain growth. Note that, a thin layer on top is a Cu-deficiency CIGS at the end process. These results suggest the necessary of Na on assisting the transformation of Cu_{2-x}Se phase into the α - $\text{Cu}(\text{In,Ga})\text{Se}_2$ phase and enhancing the uniformity of CIGS film.

ศูนย์วิทยทรัพยากร
จุฬาลงกรณ์มหาวิทยาลัย

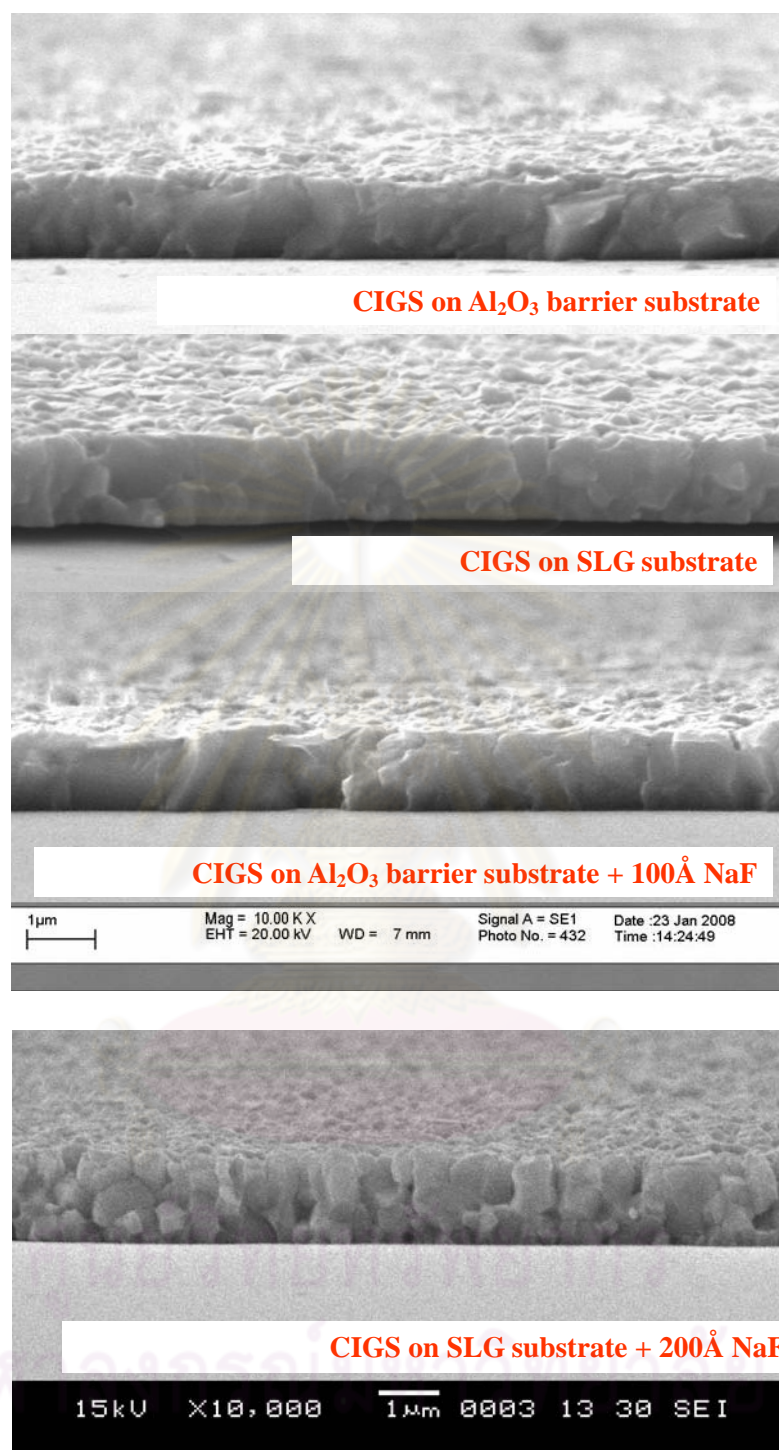


Figure 4.3 Cross-sectional images of the CIGS films grown on (a) Mo/Al₂O₃/SLG, (b) Mo/SLG and (c) NaF(100Å)/Mo/Al₂O₃/SLG (d) NaF(200Å)/Mo/SLG substrates.

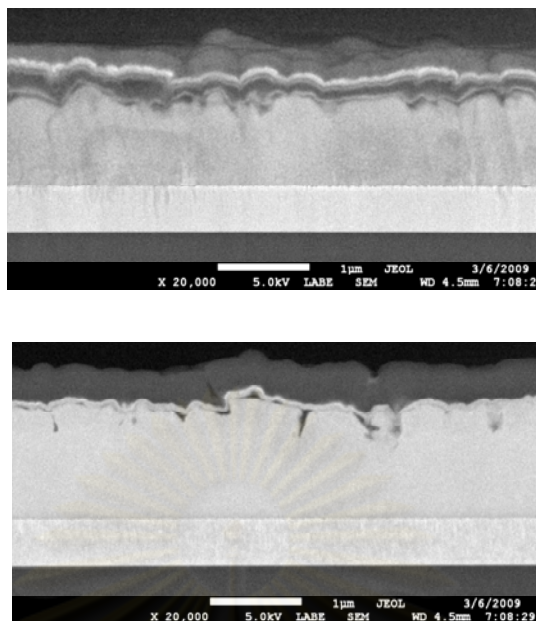


Figure 4.4 BEI Cross-sectional images of the CIGS films grown on (a) $\text{Mo}/\text{Al}_2\text{O}_3/\text{SLG}$ and (b) $\text{NaF}(100\text{\AA})/\text{Mo}/\text{Al}_2\text{O}_3/\text{SLG}$.

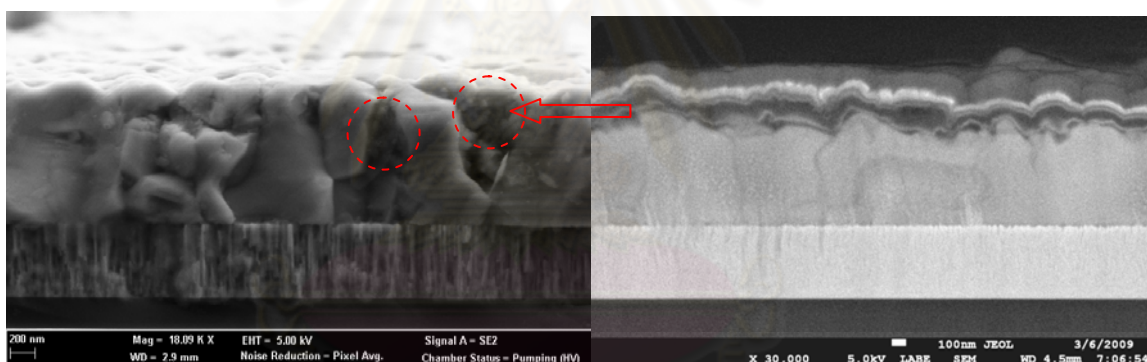


Figure 4.5 Cross-sectional images of the CIGS films grown on $\text{Mo}/\text{Al}_2\text{O}_3/\text{SLG}$ from secondary electron and BEI modes (circles indicate Cu_{2-x}Se).

4.1.2 Structural Property

XRD spectra reveal that all the CIGS polycrystalline thin films show (220)(204) preferred orientation chalcopyrite structure that dominates by nature of the three-stage growth process as seen in Fig. 4.6. It can be noticed that the ratio of (112)/(220)(204) intensities (z-ratio) changes with various substrates as seen in Table 4.1. The CIGS film grown on $\text{Mo}/\text{Al}_2\text{O}_3/\text{SLG}$ substrate has the lowest z-ratio compared with that of the CIGS films grown with NaF precursor on $\text{Mo}/\text{Al}_2\text{O}_3/\text{SLG}$ and Mo/SLG substrates. The z-ratio continuously increases when the thickness of NaF precursor increases. This result indicates the effect of Na on the orientation of crystal growth. Both

internal Na diffusion and external NaF precursor can enhance the (112) preferred orientations of the CIGS films [50]. By considering the centers of the main CIGS peaks shown in Fig. 4.7, they are nearly at the same positions in various Na-content substrates. This indicates that most Na atoms does not dissolve to form $\text{Na}_x\text{Cu}_{1-x}(\text{In,Ga})\text{Se}_2$ compound in the CIGS grain but may separate to $\text{Na}(\text{In,Ga})\text{Se}_2$ and occupy at grain boundary or on the CIGS surface as proposed in many literatures [19, 20, 21]. In addition, Na affects only the change of (112) and (220)(204) orientations but it does not affect (312)(116) orientations. The $[\text{Ga}]/([\text{In}]+[\text{Ga}])$ ratio in the films calculated from Vergard's law of the angle of 2θ is about 0.32 and consistent with the growth profile. The average grain size calculated by Sheerer's formula based on (112) orientation decreases a little bit with the Na quantity as shown in Table 4.1. The changes of the preferred orientation are directly related to the appearance of the surface morphology as seen from the SEM. The increase of (112) texture leads to the increase of sharp grains that look like the triangular shape, while the increase of (220)(204) texture leads to the increase of flat grains.

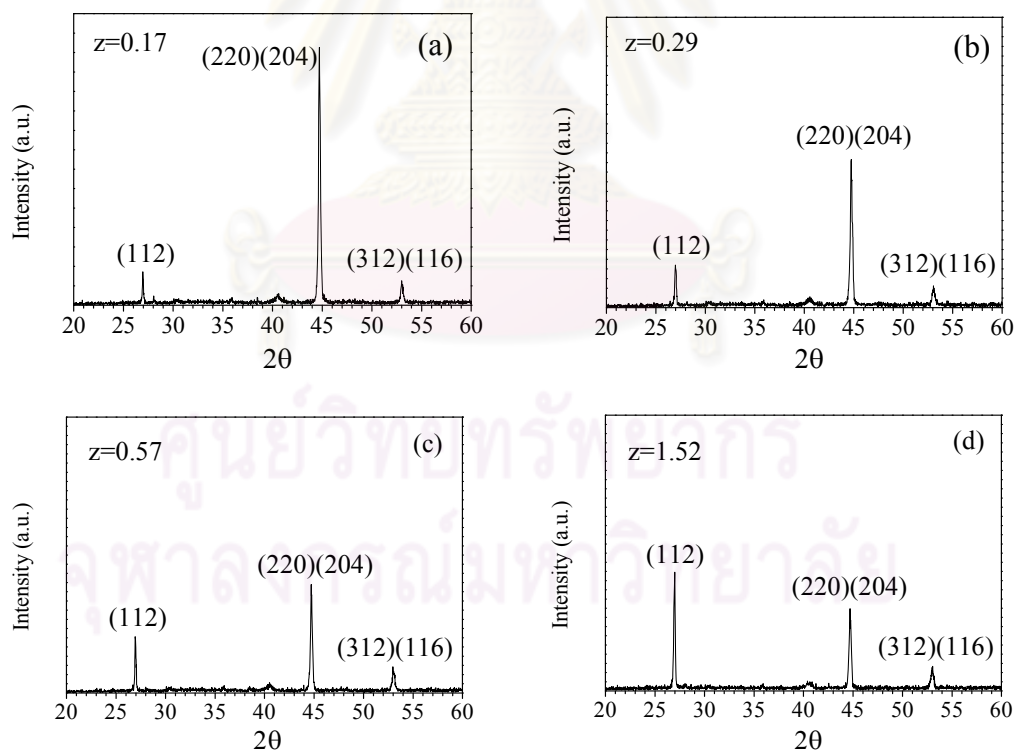


Figure 4.6 XRD spectra of the CIGS films grown on (a) $\text{Mo}/\text{Al}_2\text{O}_3/\text{SLG}$, (b) Mo/SLG , (c) $\text{NaF}(100\text{\AA})/\text{Mo}/\text{Al}_2\text{O}_3/\text{SLG}$ and (d) $\text{NaF}(200\text{\AA})/\text{Mo}/\text{SLG}$ substrates.

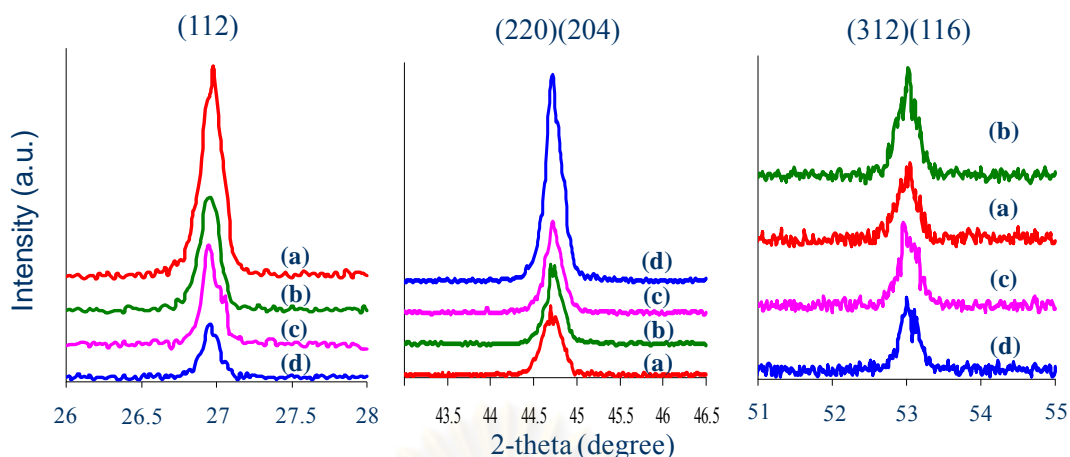


Figure 4.7 Comparison of XRD spectra of the CIGS films grown on (a) $\text{Mo}/\text{Al}_2\text{O}_3/\text{SLG}$, (b) Mo/SLG , (c) $\text{NaF}(100\text{\AA})/\text{Mo}/\text{Al}_2\text{O}_3/\text{SLG}$ and (d) $\text{NaF}(200\text{\AA})/\text{Mo}/\text{SLG}$ substrates.

Table 4.1 Crystal parameters of the CIGS film grown on difference Na contents calculated from the XRD spectra.

Substrate	Ga-content (x)	a (Å)	c (Å)	Average Grain size (nm)	z-ratio
$\text{Mo}/\text{Al}_2\text{O}_3/\text{SLG}$	0.32	5.726	11.425	140	0.17
Mo/SLG	0.32	5.726	11.424	130	0.29
$\text{NaF}(100\text{\AA})/\text{Mo}/\text{Al}_2\text{O}_3/\text{SLG}$	0.31	5.727	11.427	120	0.57
$\text{NaF}(200\text{\AA})/\text{Mo}/\text{Al}_2\text{O}_3/\text{SLG}$	0.33	5.725	11.420	110	1.52

4.1.3 Auger Electron Spectroscopy (AES) Depth Profiling

The Na content and related compound elements (Cu, In, Ga, Se and F) in the CIGS films can be measured by the AES technique. The compositional depth profiles are investigated in the CIGS films grown with internal Na diffusion from Mo/SLG and external NaF precursor on $\text{Mo}/\text{Al}_2\text{O}_3/\text{SLG}$ substrates. The distributions of Na concentration in the CIGS films and the related elements are considered. The depth profiles of the CIGS films are shown in Fig. 4.8. The distribution of Na is in the CIGS films grown with (100Å) NaF precursor on $\text{Mo}/\text{Al}_2\text{O}_3/\text{SLG}$ without a trace of Fluorine, which may decompose during the high temperature growth process. The Na distribution is uniform throughout the depth of the CIGS film. However, there may be

a very low Na concentration in the CIGS films grown on Mo/SLG (<1%) which is below the sensitivity of detector. The Na concentration from the external precursor in the CIGS film is much higher when compared with the internal diffusion from the SLG. There are two assumptions for these observations. First, NaF precursor does not decompose during the growth process and forms some Na compounds at the grain boundary. Second, Na precursor forms a cluster that is more difficult to replace in the crystal structure of the CIGS than atomic diffusion from the SLG. This result suggests that the incorporation of Na during the CIGS growth between the internal Na diffusion from the SLG and the external NaF precursor layer are distinguishable. The atomic diffusion of Na from the SLG into the CIGS film can be easily replaced or removed from the grain boundary during the CIGS growth at high temperature whereas the residual Na atoms from the precursor cannot completely diffuse out at the same temperature.

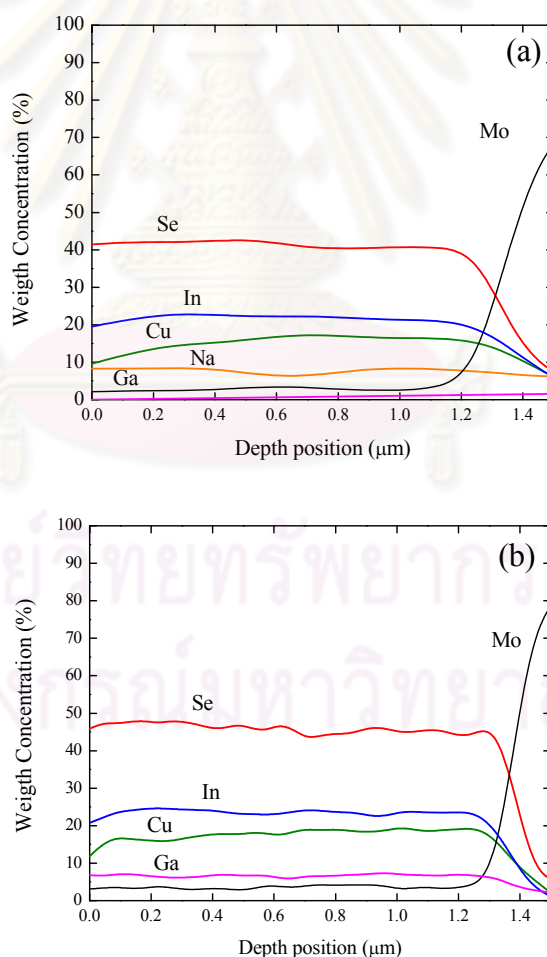


Figure 4.8 AES depth profiles for the CIGS films grown on (a) NaF(100Å)/Mo/Al₂O₃/SLG and (b) Mo/SLG.

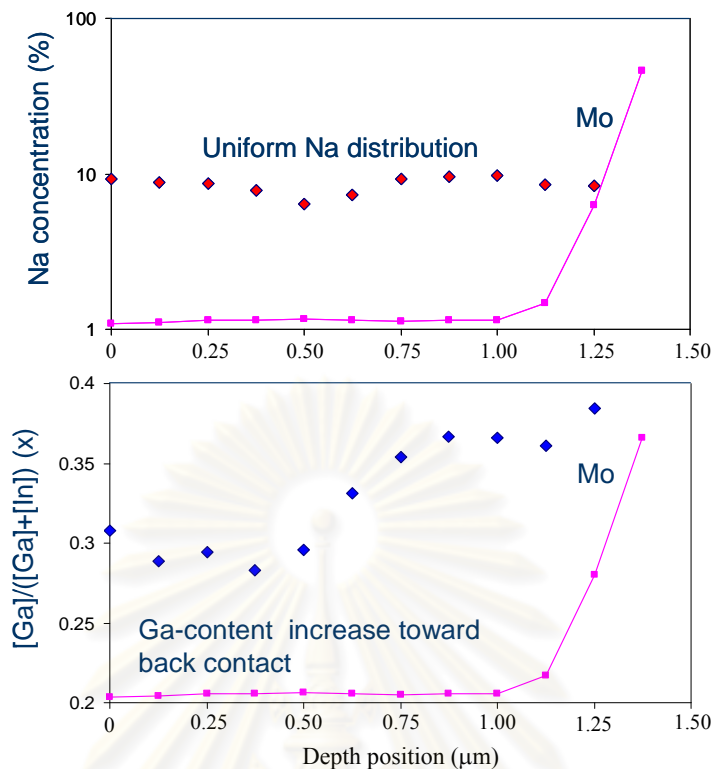


Figure 4.9 The depth profile of Na distribution and $[Ga]/([In]+[Ga])$ ratio in the CIGS film grown on $NaF(100\text{\AA})/Mo/Al_2O_3/SLG$ substrate.

These residual Na atoms may act as $Na(In,Ga)Se_2$ clusters at grain boundary of the CIGS films. The uniform Na distribution in the CIGS films indicates the high mobility of Na atoms in the CIGS film at the temperature above 500°C . In addition, The effect of Na precursor on the inter-diffusion of In and Ga is observed when consider the depth profile of $[Ga]/([In]+[Ga])$ ratio as shown in Fig. 4.9. The Ga content drops on the surface and increases toward the back contact agreed with D. Rudmann *et al.* [15]. The effect of Ga grading (band gap grading) creates the back electric field or back surface field leading to the increase of minority carrier life time as well as carrier collection.

4.1.4 Device Performance

The performances of the selected devices obtained from the I-V measurement are shown in Table 4.2. The solar cell using $Mo/Al_2O_3/SLG$ substrate has a relatively lower efficiency compared to that of the solar cell using Mo/SLG substrate indicating the lack of Na from SLG. The decrease of V_{oc} directly corresponds to the decrease of doping level or the p-type defects in the CIGS film because the internal Na diffusion

is interrupted by the Al_2O_3 barrier. This result indicates the necessary of Na incorporation in the CIGS thin film solar cells. However, the solar cell using a small amount of NaF precursor on Mo/ Al_2O_3 /SLG substrate shows the significantly increase of the V_{oc} , FF and the solar cell efficiency. The increasing of the V_{oc} and FF is related to the increase doping in the CIGS films and the junction formation, respectively. The improvement of crystal quality and the increase of the p-type defects are the main parameters to gain the solar cell efficiency. However, too much NaF precursor or high Na content decreases the solar cell efficiency due to the constitution of Na residual. The optimum thickness of NaF precursor found in this work is about 50 Å with the CIGS thickness of 1.25 μm in order to obtain the high efficiency. Note that, there are some strangeness in the samples using too much of NaF precursor on the Mo/SLG and the Mo/ Al_2O_3 /SLG substrates. The solar cell efficiency using Mo/SLG substrate is always higher than that of the Mo/ Al_2O_3 /SLG substrates, despite higher Na concentration (Na diffusion and Na precursor) in the first one mentioned. These results indicate the occurring of two mechanisms of Na incorporation into the CIGS films. The internal Na diffusion is still better to enhance doping than using the Na precursor layer by comparing the device efficiency. The atomic diffusion is more effective to enhance defects in the CIGS crystal structure than layers of NaF precursor. The relationship between the solar cell efficiency and the Na concentration in CIGS film will be considered in the next section.

Table 4.2 Device performances of the CIGS thin film solar cells using various Na content substrates.

Substrate	V_{oc} (mV)	J_{sc} (mA/cm ²)	FF (%)	η (%)
Mo/ Al_2O_3 /SLG	530	33.6	61	10.6
Mo/SLG	627	34.5	67	14.5
NaF(30Å)/ Mo/ Al_2O_3 /SLG	654	33.0	64	13.8
NaF(50Å)/Mo/ Al_2O_3 /SLG	651	34.8	67	15.2
NaF(100Å)/Mo/ Al_2O_3 /SLG	502	32.9	62	10.2
NaF(100Å)/Mo/SLG	578	34.5	67	13.4

4.1.5 The relationship between atomic concentration of Na and the doping levels in CIGS thin films

According to the device efficiency results, the open-circuit voltages change with the NaF precursor thickness. It directly relates to the Na concentration and the doping levels in the CIGS thin films. In this section, the calculation details of atomic concentration of Na in the CIGS film are described. The optimal concentration of Na to enhance the efficiency in CIGS solar cells is drawn from the experimental results. In general, the number of the evaporated atoms (element) or molecules (compound) can be calculated from

$$N_i = d_i \rho_i M_i^{-1} A N_A \quad , \quad (4.1)$$

where d_i is the film thickness,

ρ_i is the density of the evaporated material,

M_i is the molecular mass (mass per mole),

A is the unit area of the growing film,

N_A is Avogadro's constant (6.02×10^{23} atom/mole).

The α parameter of an element i is given by $\alpha_i = \rho_i M_i^{-1}$ and is shown in Table 4.3.

When normalized with the area of the growing film one obtains

$$N_i/A = d_i \alpha_i N_A \quad . \quad (4.2)$$

The concentration of Na in the CIGS thin film per unit area can be calculated by considering the thickness of NaF precursor.

Table 4.3 Density per molecular mass ratio of Cu, In, Ga, Se and NaF

Material	$\alpha = \rho/M$ (mole/cm ³)
Cu	0.1410
In	0.0637
Ga	0.0848
Se	0.0607
NaF	0.0610

Table 4.4 Number of each evaporated atom per unit area in the CIGS film at $y = 0.9$.

Material	Number of evaporated atoms (atom/cm ²)
Cu	1.38×10^{16}
In	1.08×10^{16}
Ga	4.64×10^{15}
Na (200Å NaF)	7.34×10^{14}

Table 4.5 The ratio of [Na]/[Cu] and at.% Na with the solar cell parameters.

NaF thickness (Å)	[Na]/[Cu] (%)	at.% Na	V_{oc} (mV)	η (%)
0	0	0	530	10.6
30	0.80	0.15	654	14.2
50	1.33	0.25	651	15.5
100	2.66	0.50	502	10.2

For example, 200 Å of NaF corresponds to the 7.34×10^{14} atom/cm² of Na atoms. The number of Na atoms calculated from the total thickness of metal elements in the film is shown in Table 4.4. The number of Se atoms are neglected due to the over flux used during the growth process. According to the crystal structure, Na and Cu are in group I and would be replaced or substituted by each other in the crystal structure. The ratio of N_{Na}/N_{Cu} and atomic concentration of Na in the Cu(In,Ga)Se₂ compound (at.% Na) which enhance the doping in the CIGS film and the efficiency of the solar cell are summarized in Table 4.5. The results show that the solar cell efficiency directly depends on the [Na]/[Cu] ratio or atomic percent in the CIGS compound as seen from Fig. 4.10. The solar cell parameters e.g. FF , V_{oc} and η increase with the Na content when at.% Na < 0.3 and then they rapidly decrease. By considering the V_{oc} , it shows the maximum voltage at about 0.15 at.% Na which indicates the maximum of doping in the CIGS film enhanced by the Na atoms. However, by considering the FF , it shows the different point of maximum value at about 0.25 at.% Na which indicates the quality of the CIGS film when forming the p-n junction.

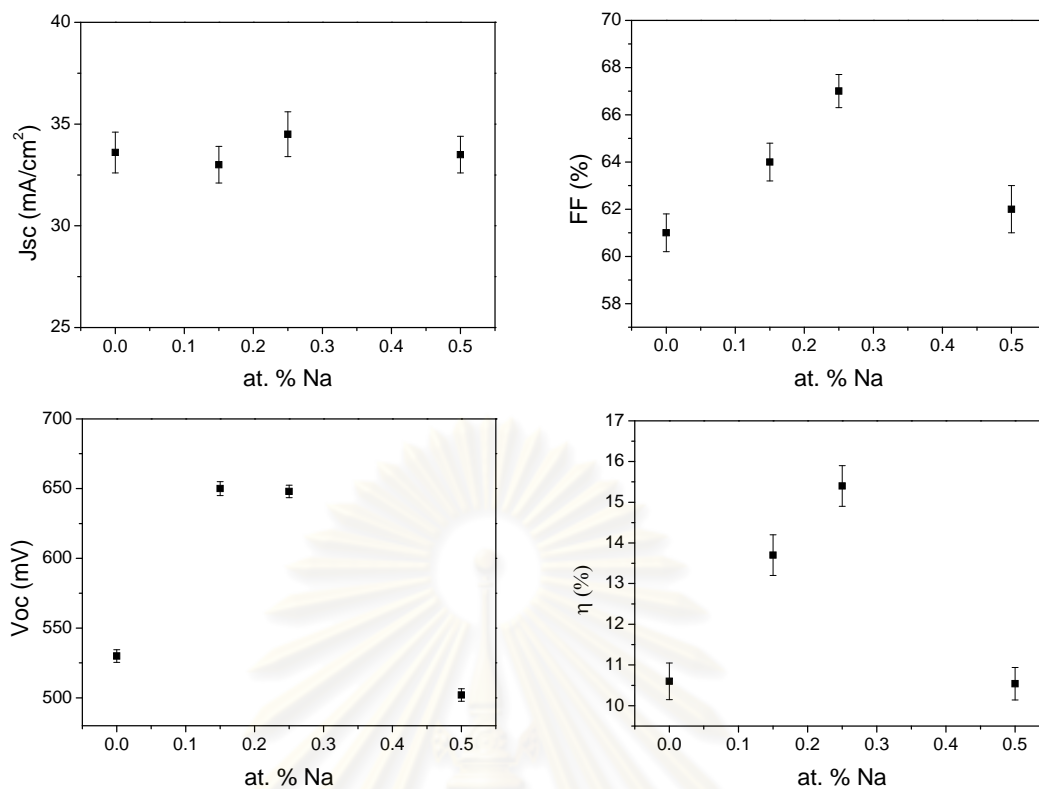


Figure 4.10 Solar cell parameters such as J_{sc} , FF, V_{oc} and η of the CIGS solar cells grown with various at. % Na.

However, Na contents have a small effect on the J_{sc} of the devices. These results are used as the guideline for the optimum ratio of at.% Na to enhance both the V_{oc} and the FF of the CIGS solar cells. The optimum atomic concentration is approximately 0.25 % which is higher than what proposed by R. Herberholz *et al.* [9]. The crystal growth mechanism and the doping mechanism enhanced by Na will be explained in chapter V.

ศูนย์วิทยทรัพยากร
จุฬาลงกรณ์มหาวิทยาลัย

4.2 Evolution of Cu(In,Ga)Se₂ thin film using Na precursor in three-stage growth process

In this work, the influences of Na precursor on the growth of the Cu(In,Ga)Se₂ thin films in the three-stage process are studied. The evolutions of the CIGS films passing through different phases e.g. γ -(In,Ga)₂Se₃, Cu(In,Ga)Se₂ + Cu_xSe are investigated by comparing with and without Na precursor. A series of samples are grown by molecular beam deposition method on the Mo coated SLG substrates with and without the NaF precursor. The Na precursor is evaporated for a total thickness of 200 Å at room temperature from the NaF source. The changes of the film properties during the three-stage growth process are investigated by interrupting the process at four points as illustrated in Fig. 4.11;

- (1) At the end of the 1st stage,
- (2) After a rapid increasing of the substrate temperature from 340°C to 500°C,
- (3) At the end of the 2nd stage or in the Cu-rich stage ($y = 1.35$), and
- (4) At the end point ($y \approx 0.9$).

The samples entitled (I), (III), (V), and (VII) are with the Na precursor and (II), (IV), (VI), and (VIII) are without the Na precursor.

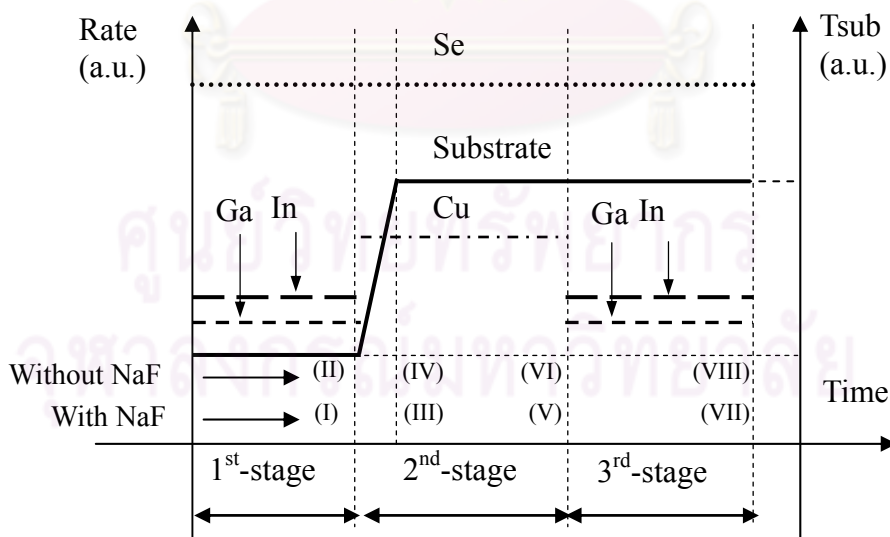


Figure 4.11 Three-stage growth profile and the interrupted points in the growth process (I), (III), (V), and (VII) refer to the films with NaF and (II), (IV), (VI), and (VIII) refer to the films without NaF.

The growth mechanism during the process is determined by characterizing the film properties at each point. In the previous work, the Na effects in the CIGS films have been investigated by K. Granath *et al.* and D. Rudmann *et al.* at a slightly Cu-poor concentration with $[Cu]/([In]+[Ga]) \approx 0.8-0.9$ but did not describe the Na effects during the growth process [11-15]. Here, I look into the entire evolution of film fabrications starting from the deposition of the Na precursor on the substrate until the complete conversion of the CIGS film. The small amount of Na-diffusion from the SLG is normally blocked by alkaline barrier such as Al_2O_3 or SiO_2 . I also intentionally exaggerate the amount of Na by ten folds in order to illustrate their dynamics and interactivities with other compounds. A simplified Na-enhancement CIGS thin film growth model based on the experimental results is introduced to explain the growth and doping mechanisms.

4.2.1 Crystal structure

The structural evolution during the growth process examined by the XRD is shown in Fig. 4.12. The samples labeled by (I), (III), (V), and (VII) are grown with NaF precursor, while the samples labeled with (II), (IV), (VI), and (VIII) are grown without NaF precursor. All significant peaks are fitted using Gaussian profile to locate the peak positions and their widths as illustrated in Fig. 4.13-4.14. A γ -phase of polycrystalline $(In,Ga)_2Se_3$ indexed by JCPDS file 00-040-1407 is found at the end of the first stage. The XRD spectra of the γ - $(In,Ga)_2Se_3$ in the films with and without NaF precursor show a dominant peak of (105) crystal orientation as seen in Fig. 4.12 (a) and (b). It is believed that Na from the precursor enhances the (105) preferred orientation of γ - $(In,Ga)_2Se_3$ and suppresses other planes, e.g. (110), (300) and (306) which are observed in the films without the NaF precursor. The crystal grain sizes based on the (105) peak calculated by Scherrer's formula are 28 and 25 nm in films (I) and (II), respectively. After rapidly increasing T_{sub} to 550°C, the (105) crystal orientation is barely observed in the films with NaF precursor and disappeared in the films without NaF precursor as shown in Fig. 4.12 (c) and (d), respectively. More random orientations are also observed in the structure of the films during the increase of the substrate temperature compared to those in the first stage. The film with NaF precursor exhibits higher random orientations than those of the film without NaF precursor. Na atoms within the precursor at the bottom layer presumably diffuse into the films and behave as defects or cluster of defects causing a nucleation of random

orientations of the γ -(In,Ga)₂Se₃ film. At the end of the second stage, there are constituents of CIGS and Cu_{2-x}Se compounds due to the excess supply of Cu during the growth as seen in the XRD spectra in Fig. 4.12 (e) and (f). The XRD spectrum of the film with NaF precursor indicates lower intensity of (220)(204) orientation than that of the film without NaF. In addition, the (112)/(220)(204) ratios of the films with and without NaF precursor are 0.8 and 0.2, respectively. The center of the CIGS (112) and the Cu_{2-x}Se (111) are approximately at the same position as well as that for CIGS (220)(204) and Cu_{2-x}Se (022). This indicates that the incorporation of Na into the CIGS and Cu_{2-x}Se to form Na-related compound has negligible effect on the crystal structures of the CIGS and the Cu_{2-x}Se. Finally, at EPD, film (VII) with Na precursor shows stronger (112) preferred orientation when compared with film (VIII) without Na precursor. The (112)/(220)(204) ratios are found to be 2.9 in the film with Na precursor and 1.2 without Na precursor. I note here that the (220)(204) preferred orientation is typically the dominant peak in the three-stage process without the NaF precursor and depends upon the y value. In our experiment, the CIGS film without NaF precursor and y ~ 1.2 exhibits the dominant (220)(204) preferred orientation (not shown here) whereas (112) preferred orientation becomes stronger in the film with y ~ 1.4. With all these evidences described, it could be deduced that the presence of Na-related compound, e.g. Na(In,Ga)Se₂, in the film could be a factor enhancing the nucleation of (112) orientation due to the structural matching of the compounds. This also agrees with the first-principle calculation of the formation of NaInSe₂ phase by Wei *et al.* [23].

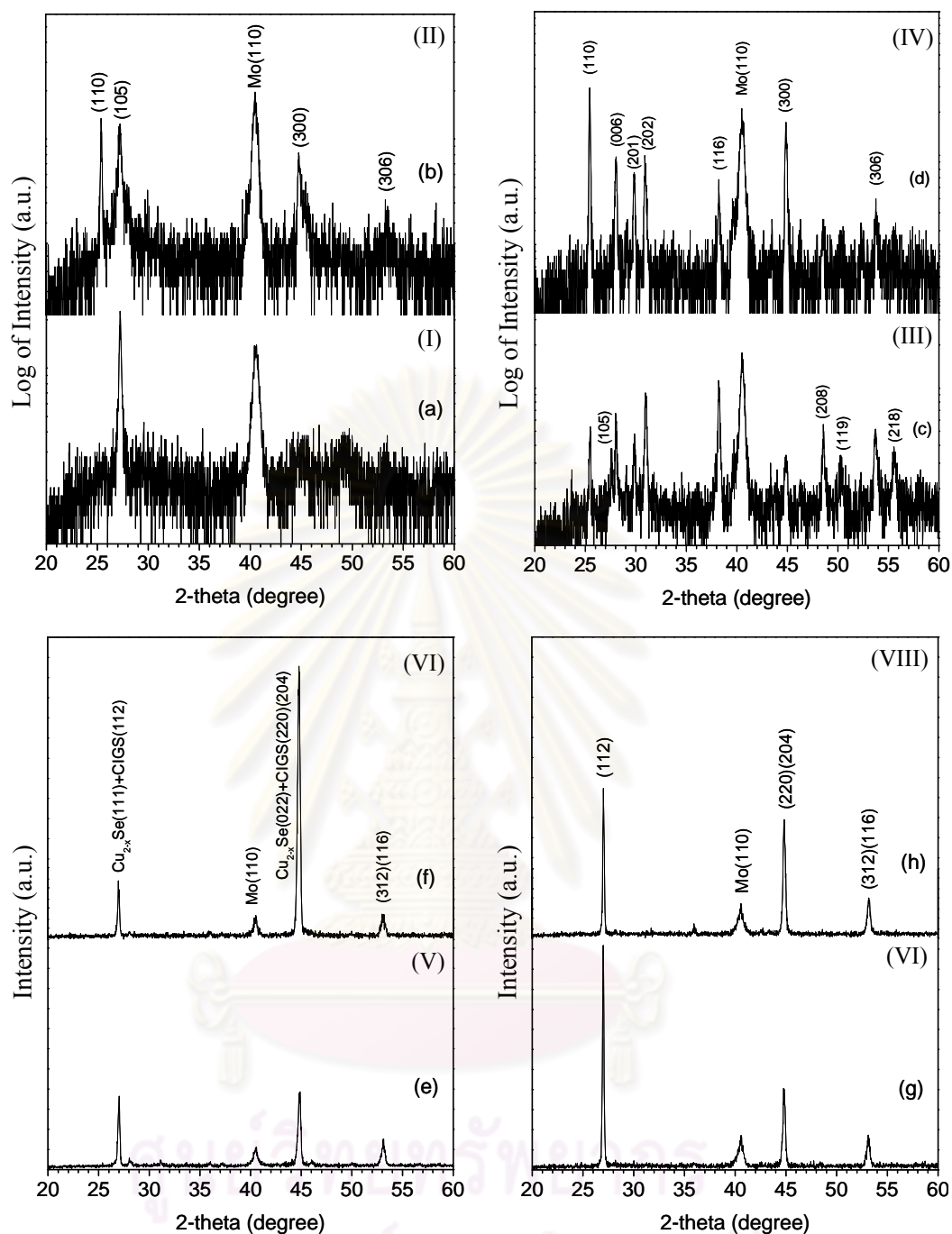


Figure 4.12 XRD spectra of the films at the end of each stage; at first stage: (a) with NaF, (b) without NaF; at the transition temperature: (c) with NaF, (d) without NaF; at the end of second stage: (e) with NaF, (f) without NaF; and at EPD: (g) with NaF, (h) without NaF.

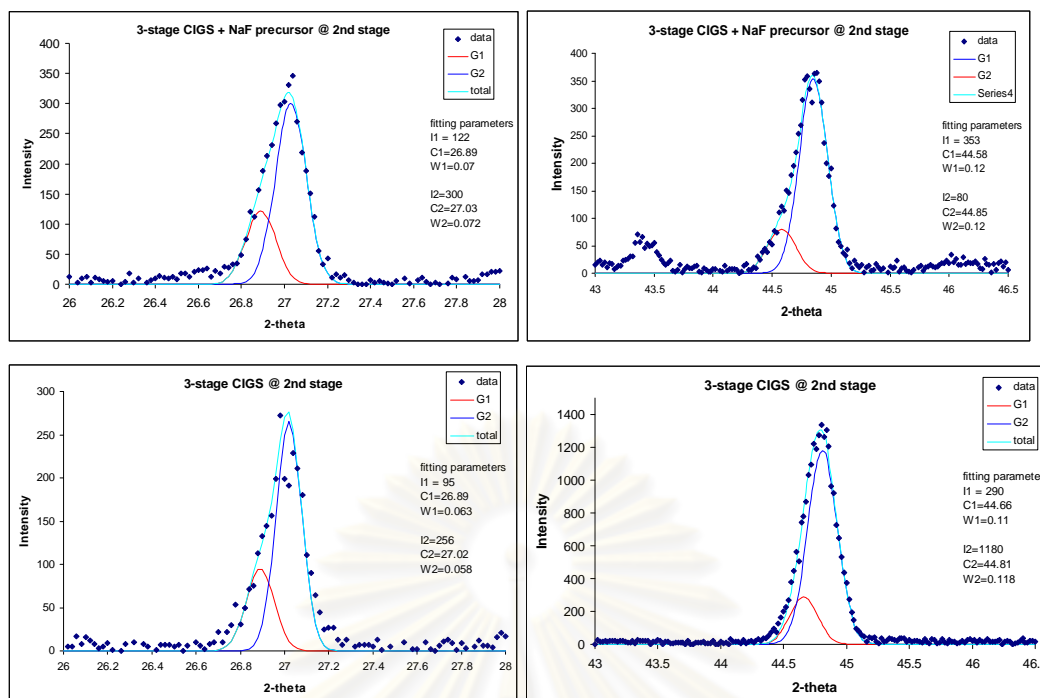


Figure 4.13 Gaussian fitting XRD spectra of the films at the end of the 2nd stage consisting of (112) and (220)(204) CIGS orientations as well as (111) and (022) $Cu_{2-x}Se$ orientations.

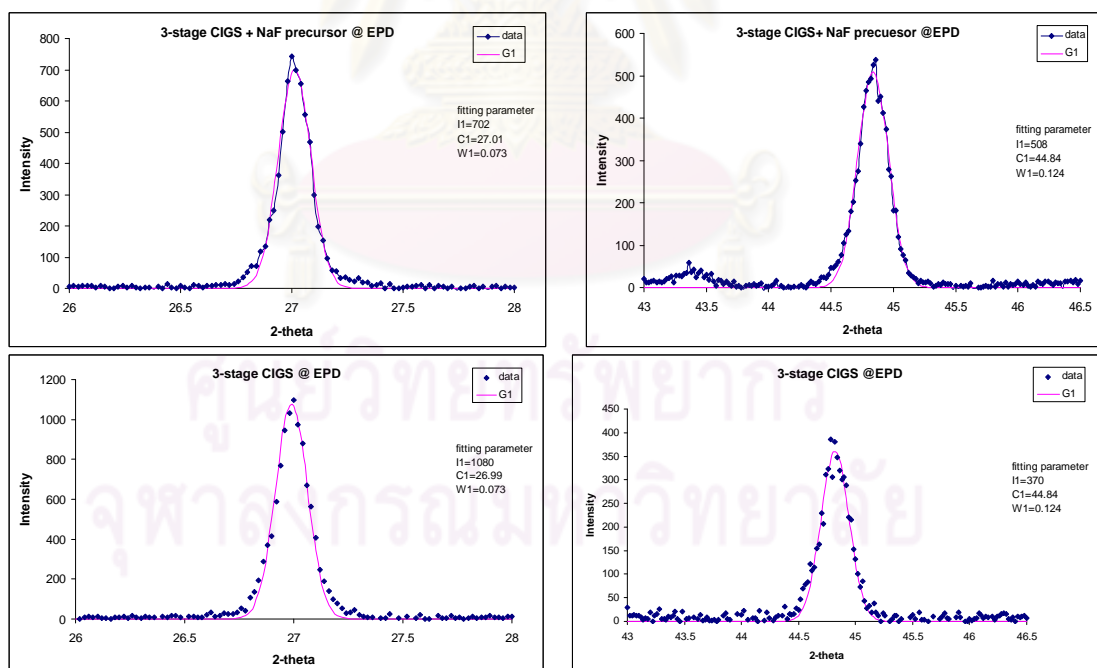


Figure 4.14 Gaussian fitting XRD spectra of the CIGS films at EPD consisting of (112) and (220)(204) orientation.

4.2.2 Surface morphology

Fig. 4.15 shows the surface morphology of the films at the interrupted points obtained by the AFM. The γ -(In,Ga)₂Se₃ films with and without Na precursor shown in Fig. 4.15 (a) and (b) show similar smooth surface with the rms roughness of approximately 50 nm. Film (I) shows a similar grain shape overall where as film (II) consists of various grain shapes such as small round grains and agglomerated long grains indicating several crystal orientations consistent with various crystal planes from the XRD result in Fig. 4.15(b). However, the average grain size of film (I) is approximately 10% larger than that of film (II) and agrees with the calculation from the XRD spectra. The homogeneity of (In,Ga)₂Se₃ films increases after the substrate is heated up to higher temperature. The reduction in grain size and surface roughness of (In,Ga)₂Se₃ films is observed in samples (III) and (IV). At the end of the second stage, films (V) with NaF precursor and (VI) without NaF precursor consist of typical stoichiometric CIGS and the excess Cu_{2-x}Se formed on the surface or grain boundaries as proposed by Klenk *et al.* [36]. Film (V) shows relatively rough surface with slightly sharp grains while film (VI) shows smoother surface due to the dominant (220)(204) preferred orientation. The result of the increasing roughness is related to the Na from the precursor. Finally, at EPD, the surface of film (VII) with NaF precursor shows typically sharp grains with small grain sizes due to the growth of (112) orientation while the smoother surface with larger grain sizes is observed in film (VIII) without NaF precursor.

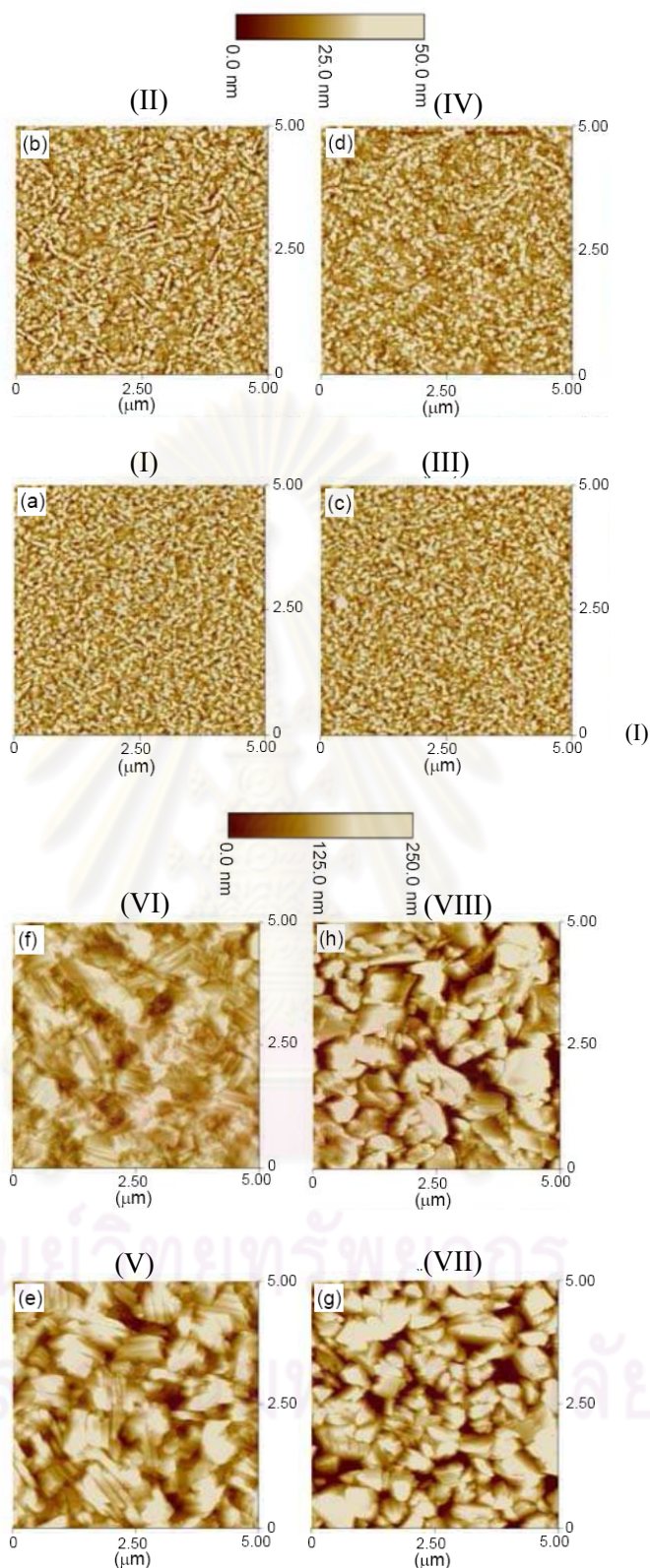


Figure 4.15 Surface morphology of the films at the end of each stage; at first stage: (a) with NaF, (b) without NaF; at the transition temperature: (c) with NaF, (d) without NaF; and at the end of second stage: (e) with NaF, (f) without NaF; and at EPD: (g) with NaF, (h) without NaF.

4.2.3 Cross-section images

Selective SEM images of the films at the end of the second stage and at EPD are shown in Fig. 4.16. Films (V) and (VI) show similarly dense grains due to the recrystallization and the formation of Cu-rich CIGS film (CIGS+Cu_{2-x}Se compounds) as indicated in the XRD results. It is believed that the excess Cu_{2-x}Se compound resides on the surface and along the grain boundaries of the Cu-rich CIGS film due to the toptactic reaction under excess Cu and Se condition [69]. After the Cu_{2-x}Se is converted to slightly Cu-poor CIGS film at EPD, film (VII) exhibits small columnar grains and deep grain boundaries with smaller grain sizes near the bottom region while film (VIII) shows large grain sizes. Both films (VII) and (VIII) show shallow crevices of random sizes near the top region. This suggests that the observation of the smaller grain size as well as deep grain boundary in the film with NaF precursor are due to Na atoms that do not dissolve to form Na_kCu_{1-k}(In,Ga)Se₂ compounds in the CIGS grains but rather Na(In,Ga)Se₂ or isolated-Na atoms and situate themselves at the grain boundaries or on the CIGS surface as also proposed by Rudmann *et al.* [70].

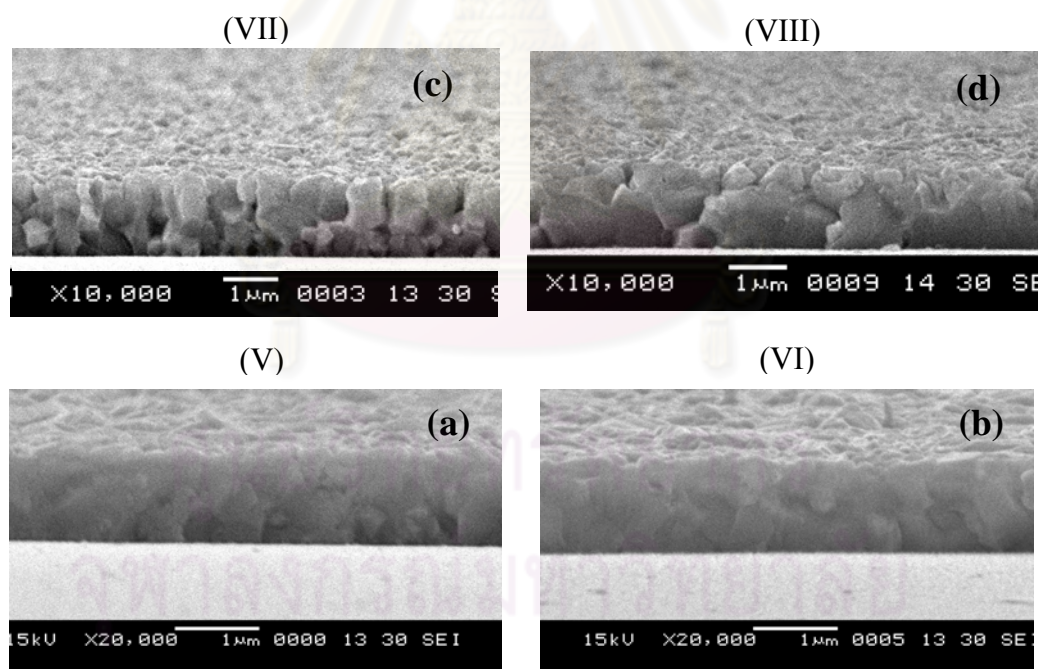


Figure 4.16 SEM cross-section images of the films at the end of the second stage: (a) with NaF, (b) without NaF; and at EPD: (c) with NaF, (d) without NaF.

4.2.4 AES depth profiles

The AES depth profiling for Na contents is performed on selective samples with NaF precursor as shown in Fig. 4.17. Most Na atoms from the precursor are located at the bottom region of the $(\text{In,Ga})_2\text{Se}_3$ film as seen in Fig. 4.17(a). This suggests that Na has poor chemical reaction to form the Na-related compounds, e.g. Na_2Se or $\text{Na}(\text{In,Ga})\text{Se}_2$, at low substrate temperature of 340°C , and/or poor diffusion into the $(\text{In,Ga})_2\text{Se}_3$ film. After a rapid increase of T_{sub} to 550°C , most of the Na atoms are found to concentrate near the film surface as seen in Fig. 4.17(b) suggesting that the Na atoms or Na compounds are driven through the $(\text{In,Ga})_2\text{Se}_3$ layers to the surface due to the increase of thermal energy. However, the Na atoms are uniformly distributed in film (V) at the end of the second stage, which also coincides with the suppression of the growth direction along (220)(204) orientation of the growing Cu-rich CIGS. It could be deduced that most Na atoms and/or the Na-related compounds would then only reside at the grain boundaries of the film in a small amount, which could not be detected by XRD. The formation of $\text{Na}(\text{In,Ga})\text{Se}_2$ is perhaps possible as small clusters in the CIGS host but there is not enough diffraction intensity. Finally, at EPD, uniform Na distribution is observed with significantly high content of Na at the CIGS surface as shown in Fig. 4.17(d). This observation suggests that during the complete conversion of Cu_{2-x}Se to slightly Cu-poor CIGS, the Na atoms or Na-related compounds can move to the CIGS surface along grain boundaries.

In addition, the variations of $[\text{Ga}]/([\text{In}]+[\text{Ga}])$ in film (VII) with the incorporation of Na can be observed as the double-graded Ga composition compared to that of a uniform Ga content in film (VIII) without NaF precursor as shown in Fig. 4.18. The Ga grading is automatically obtained in the films with NaF precursor. In other words, Na affects the inter-diffusion between In and Ga in the CIGS film during the growth of CIGS films. The variation starts in the 2nd stage as shown in Fig. 4.19 at which there has the phase transformation from $(\text{In,Ga})_2\text{Se}_3$ to CIGS. Na may disturb the mobility of Ga that creates Ga grading through the back contact.

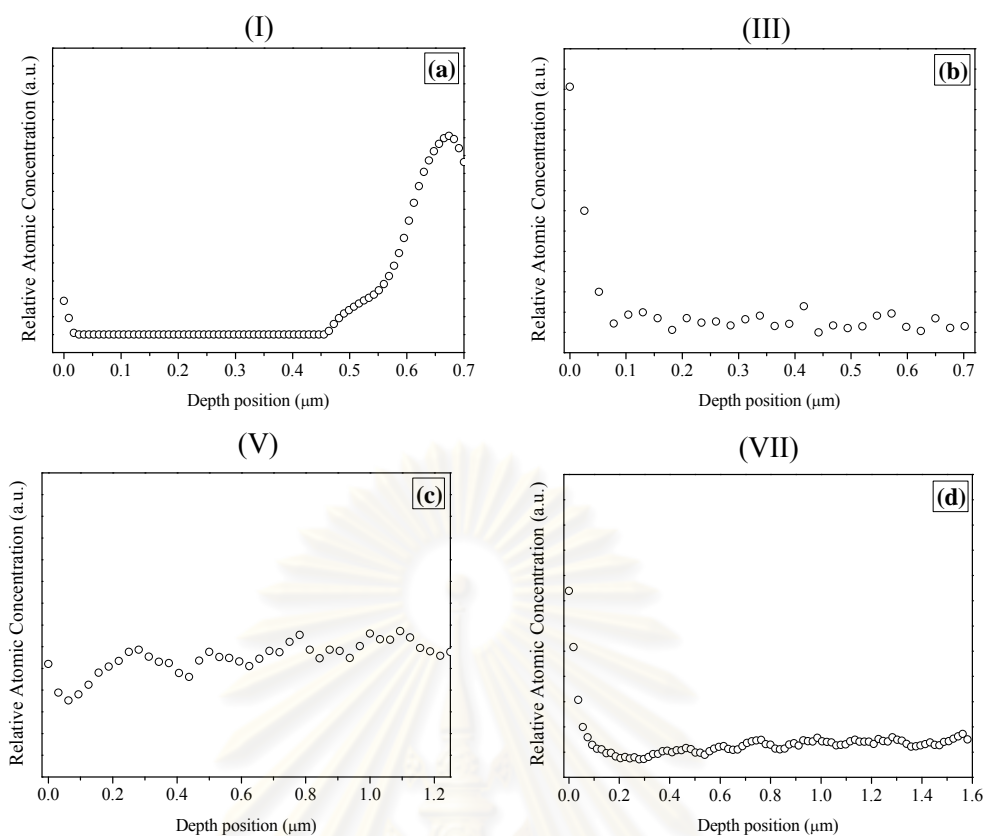


Figure 4.17 AES depth profiles of Na atoms in the films with NaF precursor; (a) end of first stage, (b) at transition temperature, (c) end of second stage, and (d) at EPD.

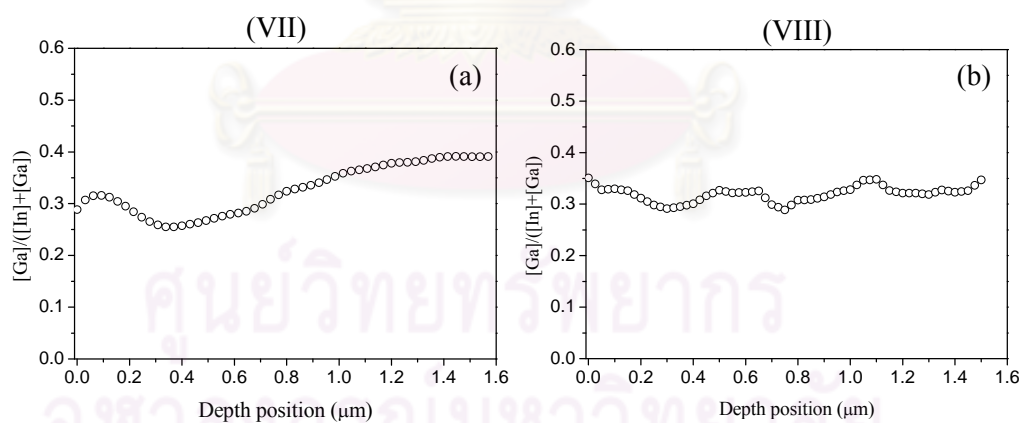


Figure 4.18 $[Ga]/([In]+[Ga])$ ratio in CIGS film with (a) and without (b) NaF precursor.

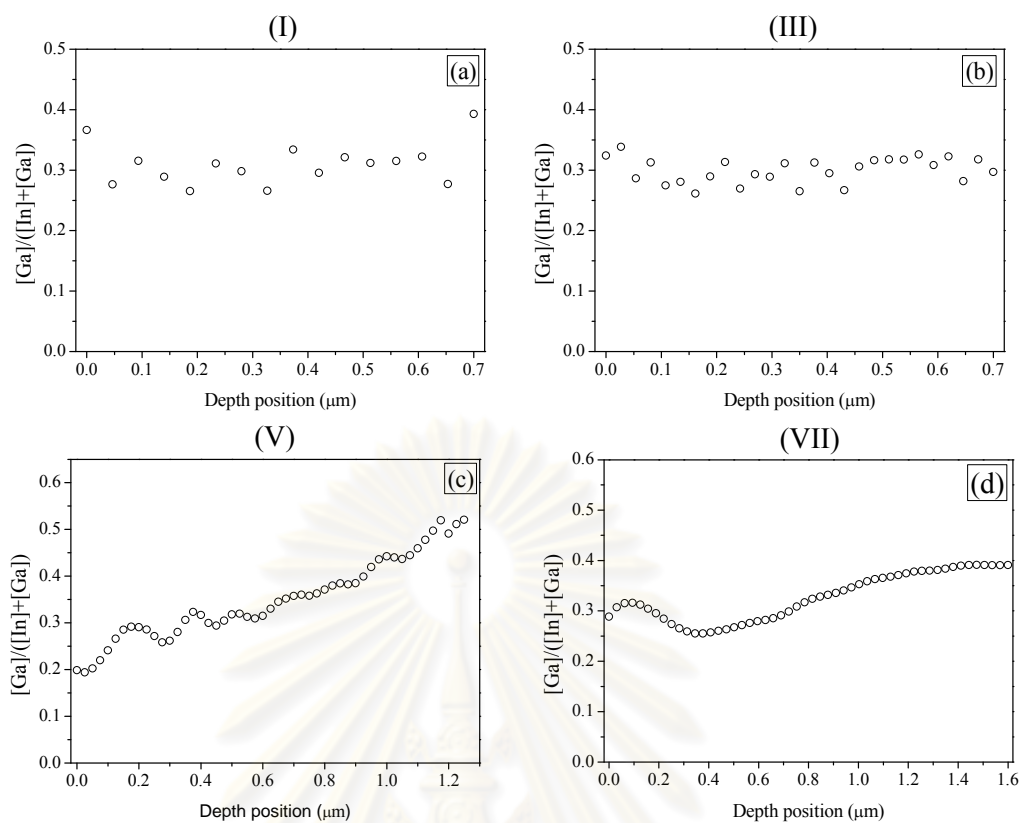


Figure 4.19 Variation of $[Ga]/([In]+[Ga])$ ratio in depth profiles of the films at interrupted points; (a) end of first stage, (b) at transition temperature, (c) end of second stage, and (d) at EPD.

ศูนย์วิทยทรัพยากร
จุฬาลงกรณ์มหาวิทยาลัย

CHAPTER V

GROWTH AND DOPING MECHANISMS

In this section, a simple model of the Na-enhanced CIGS thin film growth based on the experimental results in section 4.2 is proposed to describe the growth and doping mechanisms. The effects of Na through the entire evolution in the three-stage growth deposition starting from the deposition of the NaF precursor to the complete conversion of the CIGS film are explained. First, the growth characteristics corresponding to the grain growth, texture, and microstructure of the CIGS films will be considered. The incorporation of Na affects the growth characteristics of CIGS films by changing the preferred orientation and grain size during the growth of CIGS film due to the constitution of Na-related compounds with the Cu, (In, Ga) and Se. Then, the possible doping mechanism under the influence of Na is introduced. The increase of hole concentration relating to the native defects e.g. vacancies, interstitials, anti-site defects and clusters of defect in the crystal structure of the CIGS films is described.

A simple description on the effect of Na can then be deduced from the experimental results such that the Na from a NaF precursor is simply a mimicking of Na diffused from the SLG substrate to the CIGS film and to ensure the observation of its effect. Growth characteristics of Cu(In,Ga)Se₂ thin films using the three-stage deposition process with a NaF precursor are considered. The schematic description of the growth is illustrated in Fig. 5.1. The process starts with the layered structure of γ -(In,Ga)₂Se₃ at low substrate temperature in the first-stage where most Na atoms from NaF precursor are located at the bottom region as shown in Fig. 5.1 (a) and confirmed by the AES measurement (see AES profile in Fig. 4.24 (a)). The diffusion of Na into the (In,Ga)₂Se₃ film in the 1st stage is similar to what is observed in the Na diffusion from the SLG due to its poor chemical reaction at low temperature. The quantity of Na diffusion into CIGS film mainly corresponds to substrate temperature. In addition, the presence of NaF precursor enhances the (105) preferred orientation and suppresses the (110) crystal orientation of γ -(In,Ga)₂Se₃ which is a typical orientation of Mo film.

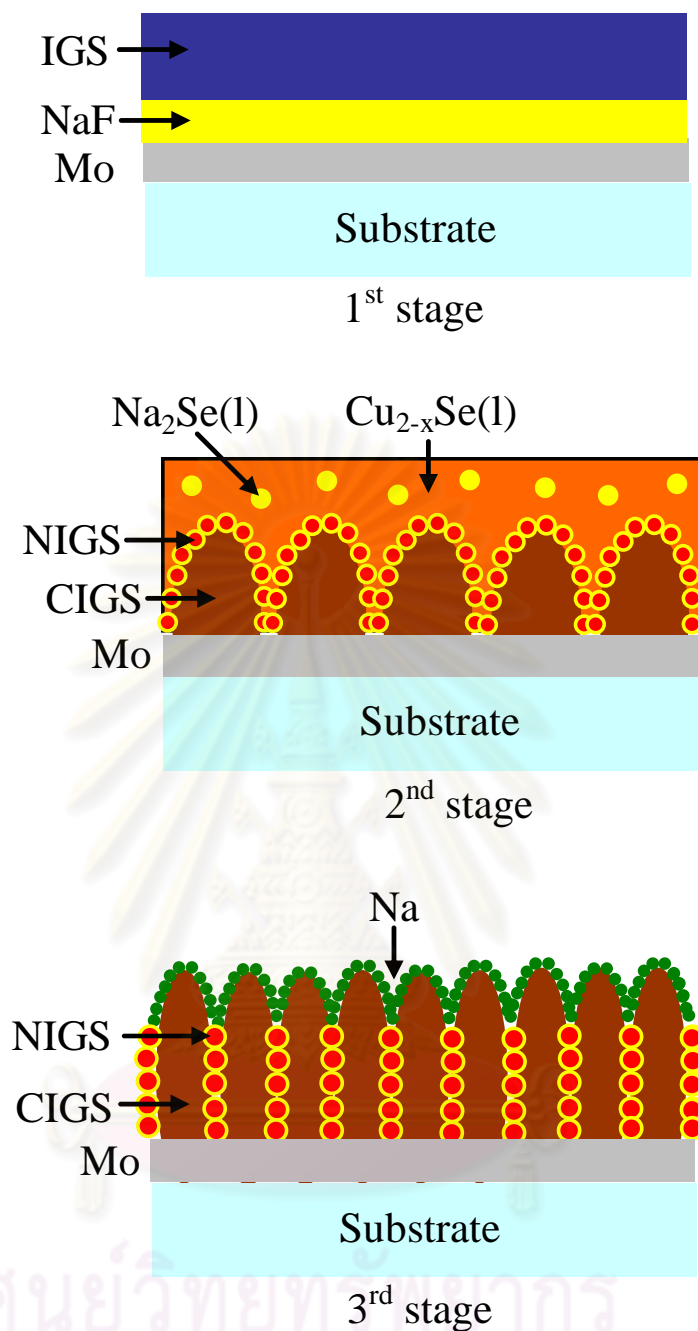


Figure 5.1 Schematic diagram of the CIGS growth model in 3-stage growth process with Na precursor (IGS, CIGS, and NIGS refer to $(\text{In,Ga})_2\text{Se}_3$, $\text{Cu}(\text{In,Ga})\text{Se}_2$, and $\text{Na}(\text{In,Ga})\text{Se}_2$ respectively).

After increasing the substrate temperature from 340 °C to 550 °C and only the Cu and high enough Se fluxes are allowed in the 2nd stage, the increase in thermal energy enhances Na diffusion and/or the formation of the Na-related compounds e.g. Na_{2-x}Se on the surface (see AES profile in Fig. 4.24 (c)) or $\text{Na}(\text{In,Ga})\text{Se}_2$ from the γ - $(\text{In,Ga})_2\text{Se}_3$ together with the formation of CIGS as depicted in Fig. 5.1 (b). With a

large structure of $\text{Na}(\text{In,Ga})\text{Se}_2$, it is believed that $\text{Na}(\text{In,Ga})\text{Se}_2$ is hard to diffuse from inside the film thus it should distribute along the CIGS grain boundaries. The Na_{2-x}Se is formed as a liquid phase according to the phase diagram [71] in addition to the liquid phase of Cu_{2-x}Se covering the surface of the stoichiometric CIGS film. Most Na atom does not dissolve to form $\text{Na}_k\text{Cu}_{1-k}(\text{In,Ga})\text{Se}_2$ compound in the CIGS grain but separate to $\text{Na}(\text{In,Ga})\text{Se}_2$ and occupy at grain boundary or on the CIGS surface as proposed in Ref. [70]. The Na_{2-x}Se can also diffuse down and be converted to $\text{Na}(\text{In,Ga})\text{Se}_2$, thus causing a more uniform distribution of Na as shown in Fig. 4.24 (e). In addition, the presence of Na-related compounds disturb the growth direction of (220)(204) orientation in the 2nd stage of CIGS thin film.

After a complete conversion of Cu_{2-x}Se to CIGS in the 3rd stage, some of $\text{Na}(\text{In,Ga})\text{Se}_2$ decompose to free Na and leave V_{Na} inside $\text{Na}(\text{In,Ga})\text{Se}_2$. Free Na atoms are driven to the surface and the V_{Na} defects take place around grain boundaries as depicted in Fig. 5.1 (c). Note that, the uniform Na distribution with significantly high content of Na at CIGS surface is obtained (see AES profile in Fig. 4.24 (g)). The smaller grain sizes as well as the deep grain boundaries in the CIGS film with Na precursor due to the Na compounds i.e. $\text{Na}(\text{In,Ga})\text{Se}_2$ take place the CIGS grain boundaries and then leave the V_{Na} defects by Na fleeing to surface. It mainly causes the increase of p-type defects similar to what is observed for V_{Cu} . The quantity of Na induced defect corresponds to the Na concentration used in the deposition process. Thus, the variation of p-type doping depends on the formation of point defects in crystal structure i.e. V_{Cu} , Na_{In} and Na_{Cu} leading to the increase of efficiency of the devices. On the other hand, the excess free Na atoms occupying V_{Cu} could reduce the p-type defect.

CHAPTER VI

CONCLUSION

In this dissertation, the influence of Na on the properties of the CIGS films and solar cell efficiency has been studied. Two main Na sources, i.e. Na from the SLG and Na from the NaF precursor are considered. The influence of Na from the SLG substrate is suppressed and then verified by using the Al_2O_3 layer as a Na diffusion barrier. The lack of Na induces flat round grains corresponding to the increase of (220)(204) texture and reduces the uniformity of the CIGS films. Na is an important parameter to enhance p-type doping in the CIGS film which could be determined from the V_{oc} and the FF. The comparative studies of two Na sources show similar characteristics e.g. the enhancement of (112) texture, the increase of film uniformity and the increase of V_{oc} and FF which lead to the possibility of using NaF as the external Na source. The improvement of crystal quality and the increase of p-type defects are the main parameters to gain the solar cell efficiency. However, thicker NaF precursor or too high Na content results in the decrease of the solar cell efficiency due to the Na residual. The optimum Na concentration in the CIGS film is approximately 0.25 at. % to achieve the best cell efficiency.

The evolution of the CIGS thin films using Na precursor during the three-stage growth process is analyzed by interrupting at the end of each stage. Na in the NaF precursor affects the crystal orientation, grain size and morphology of the growing films. The precursor located at the bottom affects the preferred orientation of γ -(In,Ga) $_2$ Se $_3$ film by enhancing the (105) orientation. Then, Na can diffuse into the mixture of the CIGS and the Cu_{2-x}Se compounds at the end of the 2nd stage. Na reduces (220)(204) orientation of the CIGS film and enhance roughness with slightly sharp grain. Finally, the small columnar grains and deep grain boundaries with the increase of (112) orientation as well as variation of $[\text{Ga}]/([\text{In}]+[\text{Ga}])$ in the CIGS film are observed at EPD.

Finally, the growth mechanism of Na incorporation in the CIGS film is introduced. The growth characteristics of the CIGS thin films with the NaF precursor using the three-stage growth process have been proposed based on the experimental

observations. The experiment is designed to have significant amount of Na from the NaF precursor in order to observe its influence with the crystal orientations, grain sizes and morphology of the growing CIGS films. The (112) preferred orientation is dominant in the CIGS film with the NaF precursor instead of (220)(204) preferred orientation typically seen in the CIGS film without NaF precursor using the three-stage process. The smaller grain size as well as deep grain boundary in the film with NaF precursor are distinguishable from the film without NaF precursor corresponding to the Na(In,Ga)Se₂ or isolated-Na atoms that resides at the grain boundaries or on the CIGS surface. At EPD, Na(In,Ga)Se₂ can be decomposed and contributes free Na atoms which are then driven to the surface thus leaving the vacancies around the grain boundaries. This results in the increase of the p-type defects. In addition, the grading of Ga composition is automatically obtained in the CIGS films with the NaF precursor.



ศูนย์วิทยทรัพยากร
จุฬาลงกรณ์มหาวิทยาลัย

References

- [1] Jacobson, M. Z. Review of Solutions to Global Warming, Air Pollution, and Energy Security. *Energy Environ. Sci.* (2009): 4.
- [2] Bube, R. H. Photovoltaic Material, London: *Imperial College Press*, 1998.
- [3] Waldau, A. J. Status of PV Research, Solar Cell Production and Market Implementation in Japan, USA and the European Union. *European Commission* (2002).
- [4] Appleyard, D. Utility-Scale Thin-Film: Three New Plants in Germany Total Almost 50 MW. *Renewable Energy World Magazine* (2009).
- [5] O'Regan, B., and Grätzel, M. A low-cost, high-efficiency solar cell based on dye-sensitized colloidal TiO₂ films. *Nature* 353 (1991): 737–740.
- [6] Ramanathan, K., et al. Properties of 19.2% Efficiency ZnO/CdS/CuInGaSe₂ Thin film Solar Cells. *Prog. Photovolt: Res. Appl.* 11 (2003): 225–230.
- [7] Barnett, A. M. and Rothwarf, A. Thin-film solar cells; a unified analysis of their potential. *IEEE Trans. Elec. Dev. ED-27* (1980): 615.
- [8] Burgess, R. M., et al. Electron and proton radiation effects on GaAs and CuInSe₂ thin film solar cells. *Conference Record of the 20th IEEE Photovoltaic Specialists Conference* (1988): 909.
- [9] Herberholz, R., et al. Phase segregation, Cu migration and junction formation in Cu(In,Ga)Se₂. *Eur. Phys. J. Appl. Phys.* 6 (1999): 131–139.
- [10] Contreras, M. A., et al. On the role of Na and modifications to CIGS absorber materials using thin MF (M=Na, K, Cs) precursor layers. *Conference Record of the 26th IEEE Photovoltaic Specialists Conference* (1997): 359–362.
- [11] Bodegård, M., et al. Growth of Cu(In,Ga)Se₂ thin films by coevaporation using alkaline precursors. *Thin Solid Films* 361-362 (2000): 9–16.
- [12] Granath, K., et al. The effect of NaF on Cu(In,Ga)Se₂ Thin Film Solar Cells. *Solar Energy Materials and Solar Cells* 60 (2000): 279–293.
- [13] Hedström, J., et al. ZnO/CdS/Cu(In,Ga)Se₂ thin film solar cells with improved performance. *Conference Record of the 23th IEEE Photovoltaic Specialists Conference* (1993): 364–371.

- [14] Kessler, F., et al. Approaches to flexible CIGS thin-film solar cells. *Thin Solid Films* 480-481 (2005): 491.
- [15] Rudmann, D., et al. Effects of NaF coevaporation on structural properties of Cu(In,Ga)Se₂ thin films. *Thin Solid Films* 431-432 (2003): 37-40.
- [16] Niles, D. W., et al. Na impurity chemistry in photovoltaic CIGS thin films: Investigation with X-ray photoelectron spectroscopy. *J. Vac. Sci. Technol. A* 15 (1997): 3044-3049.
- [17] Stanbery, B. J., et al. Engineered Phase Inhomogeneity for CIS device optimization. *Proc. of the 11th Int. Conf. on Ternary and Multinary Compounds* (1997): 915-922.
- [18] Stanbery, B. J., et al. Role of sodium in the control of defect structures in CIS. *Conference Record of the 28th IEEE Photovoltaic Specialists Conference* (2000): 440-445.
- [19] Granata, J. E., and Sites, J. R. Impact of sodium in the bulk and in grain boundaries of CIS. *Proceedings of the 2nd World Conference on Photovoltaic Solar Energy Conversion I* (1998): 604-607.
- [20] Rudmann, D. Effect of sodium on growth and properties of Cu(In,Ga)Se₂ thin films and solar cells. *Doctoral thesis, University of Basel, 2004.*
- [21] Rockett, A. The electronic effects of point defects in Cu(In_xGa_{1-x})Se₂. *Thin Solid Films* 361-362 (2000): 330-337.
- [22] Kronik, L., et al. Effects of Na on polycrystalline CIGS and its solar cell performance. *Adv. Mater.* 10 (1998): 31-36.
- [23] Wei, S. H., et al. Effects of Na on the electrical and structural properties of CuInSe₂. *Journal of Applied Physics* 85 (1999): 7214-7218.
- [24] Ohring, M. *Materials Science of Thin Films*. New Jersey: Academic Press, 2002.
- [25] Elshabini, A., and Barlow, F. D. *Thin film technology handbook*. New York: McGraw-Hill, 1998.
- [26] NREL, Available from <http://www.nrel.gov/rredc>.
- [27] Jaffe, J. E. and Zunger, A theory of the band gap anomaly in ABC₂ chalcopyrite semiconductors. *Phys. Rev. B* 29 (1984): 1882-1906.

- [28] Wei, S. H., Zhang, S. B., and Zunger, A. Effects of Ga addition to CuInSe₂ on its electronic, structural, and defect properties. *Appl. Phys. Lett.* 72 (1998): 3199–3201.
- [29] Vegard, L. Die Konstitution der Mischkristalle und die Raumfüllung der Atome. *Zeitschrift für Physik*, 5:17, 1921.
- [30] Stanbery, B. J. Copper Indium Selenides and Related Materials for Photovoltaic Devices. *Crit. Rev. Solid State* 27 (2002):73–117.
- [31] Mikkelsen, J. C. Ternary phase relations of the chalcopyrite compound CuGaSe₂. *J. Elec-tron Mater.* 10 (1981): 541-558.
- [32] Rudmann, D. Effect of sodium on growth and properties of Cu(In,Ga)Se₂ thin films and solar cells. *Doctoral thesis, University of Basel*, 2004.
- [33] Rincon, C. et al. Optical properties and characterizations of CuInSe₂. *Solar Cells* 16 (1986):335-349.
- [34] Mickelsen, R. A., and Chen, W. S. High photocurrent polycrystalline thin-film CdS/CuInSe₂ solar cell. *Appl. Phys. Lett.* 36 (1980): 371–373.
- [35] Mickelsen, R. A., and Chen, W. S. Development of a 9.4% efficient thin-film CuInSe₂/CdS solar cell. *Conference Record of the 15th IEEE Photovoltaic Specialists Conference* (1981): 800– 804.
- [36] Klenk, R., et al. A Model for the Successful Growth of Polycrystalline Films of CuInSe₂ by Multisource Physical Vacuum Evaporation. *Adv. Mater.* 5 (1993) : 114–119.
- [37] Chityuttakan, C. et al. In situ monitoring of the growth of Cu(In,Ga)Se₂ Thin Films. *Solar Energy Materials and Solar Cells* 90 (2006) : 3124.
- [38] Nishiwaki, S. et al. Preparation of Cu(In,Ga)Se₂ thin films from Cu-Se/In-Ga-Se precursors for high-efficiency solar cells. *Solar Energy Materials and Solar Cells* 67 (2001) : 217–223.
- [39] Gabor, A. M. et al. High-efficiency CuIn_xGa_{1-x}Se₂ solar cells made from (In_xGa_{1-x})₂Se₃ precursor films. *Appl. Phys. Lett.* 65 (1994) : 198.
- [40] Gabor, A. et al. Band-gap engineering in Cu(In,Ga)Se₂ thin films grown from (In,Ga)₂Se₃ precursors. *Solar Energy Materials and Solar Cells* 41-42 (1996): 247–260.

- [41] Scheer, R. et al. Cu(In_{1-x}Ga_x)Se₂ growth studies by *in situ* spectroscopic light scattering. *Appl. Phys. Lett.* 82 (2003): 2091–2093.
- [42] Kessler, J. et al. Analysis of CIGS films and devices resulting from different Cu-rich to Cu-poor transitions. *Proceedings of the 17th European Photovoltaic Solar Energy Conference 2* (2001):1019–1022.
- [43] Dullweber, T. et al. A new approach to high-efficiency solar cells by band gap grading in Cu(In,Ga)Se₂ chalcopyrite semiconductors. *Solar Energy Materials and Solar Cells* 67 (2001): 145-150.
- [44] Dullweber, T. et al. Back surface band gap gradings in Cu(In,Ga)Se₂ solar cells. *Thin Solid Films* 387 (2001): 11-13.
- [45] Song, J. L. et al. Device modeling and simulation of the performance of Cu(In_{1-x}Ga_x)Se₂ solar cells. *Solid-State Electronics* 48 (2004): 73–79.
- [46] Gloeckler, M., and Sites J. R. Band-gap grading in Cu(In,Ga)Se₂ solar cells. *Journal of Physics and Chemistry of Solids* 66 (2005): 1891–1894.
- [47] Lundberg, O. et al. The effect of Ga-grading in CIGS thin film solar cells. *Thin Solid Films* 480–481 (2005): 520–525.
- [48] Lundberg, O. et al. Diffusion of indium and gallium in Cu(In,Ga)Se₂ thin film solar cells. *Journal of Physics and Chemistry of Solids* 64 (2003): 1499–1504.
- [49] Kohara, N. et al. Preparation of device-quality Cu(In,Ga)Se₂ thin films deposited by co-evaporation with composition monitor. *Jpn. J. Appl. Phys.* 34 (1995): L1141–L1144.
- [50] Kessler, J. et al. Analysis of CIGS films and devices resulting from different Cu-rich to Cu-poor transitions. *Proceedings of the 17th European Photovoltaic Solar Energy Conference 2* (2001): 1019–1022.
- [51] Nishitani, M. et al. Composition monitoring method in CuInSe₂ thin film preparation. *Thin Solid Films* 258 (1995): 313–316.
- [52] Scofield, J. H. et al. Sputtered molybdenum bilayer back contact for copper indium diselenide-based polycrystalline thin-film solar cells. *Thin Solid Films* 260 (1995): 26-31.

- [53] Gordillo, G. et al. Structural and electrical properties of DC sputtered molybdenum Films. *Solar Energy Materials and Solar Cells* 51 (1998): 327-337.
- [54] Abou-Ras, D. et al. Formation and characterization of MoSe₂ for Cu(In,Ga)Se₂ based solar cells. *Thin Solid Films* 480-481 (2005): 433-438.
- [55] Al-Thani, H. A., and Williamson, D. L. The Effect of Mo Back Contact on Na Out Diffusion and Device Performance of Mo/Cu(In,Ga)Se₂/CdS/ZnO Solar Cells. *29th IEEE PV Specialists Conference* (2002).
- [56] Granath, K. The Influence of Na on the Growth of Cu(In,Ga)Se₂ Layers for Thin Film Solar Cells. *PhD. thesis, Uppsala University*, 1999.
- [57] Rockett, A. et al. Na incorporation in Mo and CuInSe₂ from production processes. *Solar Energy Materials and Solar Cells* 59 (1999): 255–264.
- [58] Hashimoto, Y. et al. Chemical bath deposition of CdS buffer layer for GIGS solar cells. *Solar Energy Materials and Solar Cells* 50 (1998): 71-7.
- [59] Contreras, M. A. et al. Optimization of CBD CdS process in high efficiency Cu(In,Ga)Se₂-based solar cells. *Thin Solid Films* 403–404 (2002): 204–211.
- [60] Nakada, T. et al. Band offset of high efficiency CBD-ZnS/CIGS thin film solar cells. *Thin Solid Films* 431-432 (2003): 242-248.
- [61] Nakada, T. et al. High-efficiency Cu(In,Ga)Se₂ thin-film solar cells with a CBD-ZnS buffer layer. *Solar Energy Materials and Solar Cells* 67 (2001): 255-260.
- [62] Ortega-Borges, R., and Lincot, D. Mechanism of Chemical Bath Deposition of Cadmium Sulfide Thin Films in the Ammonia-Thiourea System. *J. Electrochem. Soc.* 140 (1993): 3464–3473.
- [63] Powalla, M. et al. Large-area CIGS modules: processes and properties. *Thin Solid Films* 431–432 (2003): 523.
- [64] Karg, F. H. et al. Development and manufacturing of CIS thin film solar modules. *Solar Energy Materials and Solar Cells* 66 (2001): 645.
- [65] Ellmer, K. et al. Magnetron sputtering of transparent conductive zinc oxide: relation between the sputtering parameters and the electronic properties. *J. Phys. D: Appl. Phys.* 33 (2000): R17-R32.

- [66] Kessler, J. et al. Optimization of rf-sputtered ZnO/ZnO:Al for CIGS based devices. *Proceedings of the 16th European Photovoltaic Solar Energy Conference*, 1 (2000): 775–778.
- [67] Bhattacharyya, D. et al. Determination of optical constants and band gaps of bi-layered semiconductor films. *Vacuum* 46 (3), (1995): 309-313.
- [68] Neumann, H. Optical properties and electronic band structure of CuInSe₂. *Solar Cells* 16 (1986): 317-333.
- [69] Wada, T. et al. Growth of CuInSe₂ crystals in Cu-rich Cu-In-Se thin films. *J. Mater. Res.* 12 (1997) 1456.
- [70] Rudmann, D., et al. Efficiency enhancement of Cu(In,Ga)Se₂ solar cells due to post-deposition Na incorporation, *Appl. Phys. Lett.*, 84 (2004) 1129-1131.
- [71] Massalski, T. B. Binary Alloy Phase Diagrams, Second edition, Materials Information Society, Materials Park, OH, 1990 vol.3.



APPENDICES

ศูนย์วิทยทรัพยากร
จุฬาลงกรณ์มหาวิทยาลัย

APPENDIX A

LIST OF ABBREVIATIONS

AES	Auger electron spectroscopy
AFM	Atomic force microscopy
AM 1.5, AM 0	Air mass 1.5, air mass 0
at. %	Atomic percent
AZO	Aluminum zinc oxide
BEI	Backscatter electron image
BSF	Back-surface field
CBD	Chemical bath deposition
CGS	Compound of CuGaSe ₂
CIGS	Compound of Cu(In,Ga)Se ₂
CIS	Compound of CuInSe ₂
c-Si	Crystalline Silicon
CUPRO	Cu-poor, rich, off
DC	Direct current
E_C	Conduction band energy
E_F	Fermi energy
E_g	Band gap energy
E_V	Valance band energy
EDX	Energy dispersive X-ray spectroscopy
EPD	End point detection
FF	Fill factor
FSEM	Field emission scanning electron microscope
FTO	Fluorine tin oxide
ITO	Indium tin oxide or tin-doped indium oxide
I-V	Current-Voltage
J_{sc}	Short-circuit current density
K-cells	Knudsen cells
MBE	Molecular beam Epitaxy
MBD	Molecular beam deposition

NDCs	Neutral defect complexes
NREL	National Renewable Energy Laboratory
NIR, VIS, UV	Near infrared, visible, ultra violet
OVC	Ordered vacancy compound
ODC	Ordered defect compound
PV	Photovoltaic
PVD	Physical vapor deposition
QCM	Quartz crystal monitor
RBS	Rutherford backscattering spectroscopy
RF	Radio frequency
RHEED	Reflection high-energy electron diffraction
ΔS	Stoichiometry deviation
SEM	Scanning electron microscope
SIMS	Secondary ion mass spectroscopy
SLG	Soda-lime glass
SPRL	Semiconductor physics research laboratory
TCO	Transparent conducting oxide
T_{sub}	Substrate temperature
T_{pyro}	Pyrometer temperature
% T , % R	Optical transmission, Optical refraction
VLS	Vapour-liquid-solid
V_{oc}	Open-circuit voltage
x	[Ga]/([In]+[Ga]) ratio
XRD	X-ray diffraction
XPS	X-ray photoelectron spectroscopy
y	[Cu]/([In]+[Ga]) ratio

APPENDIX B

LIST OF CONFERENCES

1. Sakdanuphab, R., Chinvetkitvanich, P., Chatraphorn, S., Yoodee, K., and Chityuttakarn, C. "Ga-Graded CIGS Thin Film Absorber Grown By Co-evaporation Method" *The 32nd Congress on Science and Technology Thailand (STT32)*, Bangkok, Thailand, 10-12 October 2006.
2. Sakdanuphab, R., Arthibenyakul, B., Chityuttakarn, C., Chatraphorn, S., and Yoodee, K. "Effect of Ga-graded region to the performance of $\text{CuIn}_{1-x}\text{Ga}_x\text{Se}_2$ thin film solar cells" *Siam Physics Congress 2007 (SPC 2007)*, Nakorn Pathom, Thailand, 22-24 March 2007.
3. Sakdanuphab, R., Chatraphorn, S., Yoodee, K., and Chityuttakarn, C. "Sodium-enhanced 3-stage growth of CIGS thin film solar cells" *Siam Physics Congress 2008 (SPC 2008)*, Nakorn Ratchasima, Thailand, 20-22 March 2008.
4. Sakdanuphab, R., Chinvetkitvanich, P., Chatraphorn, S., and Chityuttakarn, C. "Effects of Sodium Fluoride precursor in $\text{Cu}(\text{In,Ga})\text{Se}_2$ Thin Film Solar Cells" *5th Thailand Materials Science and Technology Conference (MSAT5)*, Bangkok, Thailand, 16-19 September 2008.
5. Sakdanuphab, R., Chatraphorn, S., Yoodee, K., and Chityuttakarn, C. "Enriching Sodium Fluoride in 3-Stage Growth $\text{Cu}(\text{In,Ga})\text{Se}_2$ Thin Film Grown by Molecular Beam Deposition Method" *The 34th Congress on Science and Technology Thailand (STT34)*, Bangkok, Thailand, 31 October – 2 November 2008.
6. Chityuttakarn, C., Chatraphorn, S., and Sakdanuphab, R. "Influence of Ga-Graded to the Performance of CIGS Thin Film Solar Cells" *4th Mathematics and Physical Sciences Graduate Congress 2008 (MPSGC 08)*, National University of Singapore, Singapore, 17-19 December, 2008.
7. Sakdanuphab, R., Chatraphorn, S., and Chityuttakarn, C. "Effects of Se Flux on 2-Stage Growth of $\text{Cu}(\text{In,Ga})\text{Se}_2$ Thin Film Solar Cells" *Siam Physics Congress 2009 (SPC 2009)*, Petchburi, Thailand, 20-22 March 2009.
8. Sakdanuphab, R., Chatraphorn, S., Yoodee, K., and Chityuttakarn, C. "Efficiency Enhancement of $\text{Cu}(\text{In,Ga})\text{Se}_2$ Thin Film Solar Cells by NaF

Precursor” *Siam Physics Congress 2010 (SPC 2010)*, Kanchanaburi, Thailand, 25-27 March 2010.

9. Sakdanuphab, R., Chinvetkitvanich, P., Chatraphorn, S., Yoodee, K., and Chityuttakarn, C. “Evolution of Cu(In,Ga)Se₂ Thin Films using Na Precursor in the 3-stage Growth Process” *7th Asian Meeting on Ferroelectricity (AMF-7) and the 7th Asian Meeting on Electroceramics (AMEC-7)*, Jeju island, Korea, 28 June – 1 July 2010.
10. Sakdanuphab, R., Chatraphorn, S., and Chityuttakarn, C. “Development of Cu(In,Ga)Se₂ Thin Film Solar Cells: A Study of NaF Effects on CIGS using Alkaline Diffusion Barrier” *6th Thailand Materials Science and Technology Conference (MSAT6)*, Bangkok, Thailand, 26-27 August 2010.



ศูนย์วิทยทรัพยากร
จุฬาลงกรณ์มหาวิทยาลัย

APPENDIX C

LIST OF PUBLICATIONS

1. Sakdanuphab, R., Chityuttakan, C., Pankiew, A., Somwang, N., Yoodee, K., Chatraphorn, S. "Growth characteristics of Cu(In,Ga)Se₂ thin films using 3-stage deposition process with a NaF precursor" *Journal of Crystal Growth* **319** (2011) 44-48.
2. Sakdanuphab, R., Chityuttakan, C., Yoodee, K., Chatraphorn, S. "Evolution of Cu(In,Ga)Se₂ thin films using Na precursor in the 3-stage growth process" submitted in *Current Applied Physics* (Special Issue: AMF/AMEC-7).
3. Sakdanuphab, R., Chityuttakan, C., Arthibenyakul, B., Chatraphorn, S., Yoodee, K., "Effect of Ga-graded region to the performance of CuIn_{1-x}Ga_xSe₂ thin film solar cells" *THAI JOURNAL OF PHYSICS Series 3* (2008).
4. Sakdanuphab, R., Chityuttakan, C., Chatraphorn, S., Yoodee, K., "Sodium-enhanced 3-stage growth of CIGS thin film solar cells" *THAI JOURNAL OF PHYSICS Series 4* (2009).
5. Sakdanuphab, R., Chityuttakan, C., Chatraphorn, S., Yoodee, K., "Effects of Se flux on 2-stage growth of Cu(In,Ga)Se₂ thin films solar" *THAI JOURNAL OF PHYSICS Series 5* (2010).

VITAE

Rachsak Sakdanuphab was born on 2nd November 1981 in Prachuabkirikhan province, Thailand. He was a student in Development and Promotion for Science and Technology Talent Project (DPST) since 1999-2010. He received his Bachelor of Science degree (First Class Honors) in Physics from Kasetsart University in 2002, and received his Master of Science degree in Physics from Chulalongkorn University in 2006. He worked at semiconductor physics research laboratory (SPRL), Chulalongkorn University during his PhD. course.



ศูนย์วิทยทรัพยากร
จุฬาลงกรณ์มหาวิทยาลัย